THE UNIVERSITY *of* EDINBURGH

Axion dark matter and two-neutrino double electron capture searches in the Large Underground Xenon experiment

Maria Francesca Marzioni

Doctor of Philosophy
The University of Edinburgh
January 2018

Abstract

The hunt for Dark Matter plays a truly critical role in contemporary physics. At both the largest and smallest scales, deep questions are being raised about the fundamental nature of the universe – questions that confirmation and then characterisation of particle dark matter will provide many answers to. This thesis presents some of the world's most sensitive searches to date for certain types of axion dark matter, axion-like particles, and two-neutrino double electron capture. These have been conducted using the Large Underground Xenon (LUX) experiment.

Evidence for dark matter and physics beyond the Standard Model of particle physics is described in Chapter 1, while Chapter 2 gives an overview of proposed candidates for particle dark matter. The various experimental approaches being used to detect particle dark matter are presented in Chapter 3. Direct detection with time projection chambers plays a major role in this thesis, with particular interest in the LUX detector, that is described in its components and operations. Chapter 4 presents LUX direct searches for weakly interacting massive particles. Although I have contributed to these analyses, they are included for completeness only, as they are not part of my central work.

The LUX collaboration's searches for axion dark matter and axion-like particle have delivered world-leading results on the axion-electron coupling constant. These results, that I personally led and which have been published in Physics Review Letters, are presented in Chapter 5, along with sensitivity studies, also led by me, made for the future LUX-ZEPLIN experiment.

Finally, a search for two-neutrino double electron capture of ^{124}Xe, that I performed using LUX data to extract a limit on the half life of the process, is presented in Chapter 6. Although being allowed by the Standard Model, two-

neutrino double electron capture shares the matrix element calculation framework with the neutrinoless channel of the same process, becoming of great interest in the scope of neutrino physics.

Conclusions follow and close the thesis.

Declaration

This thesis was composed by myself and not submitted for any other degree or professional qualification. The work presented in this thesis was carried out within the Nuclear Physics and the Particle Physics Experiment groups at the University of Edinburgh, as part of the LUX and LUX-ZEPLIN collaborations. I personally led the analysis of LUX data for axion and axion-like particle searches, as described in Chapter 5. The two-neutrino double electron capture analysis discussed in Chapter 6 is also part of my original work, while I only contributed to the work discussed in Chapter 3 and 4.

Maria Francesca Marzioni, January 2018

Acknowledgements

A page in my thesis will never be enough to thank all the people who made it possible. This thesis and I would not be here without the support of many. Someone said that *happiness is only real when shared*. My happiness today is true only because I am surrounded by many incredible people.

First of all, I would like to thank Prof. Alexander Murphy, my supervisor, the guide who led me through this hard and, at the same time, incredible path. He has always been there for me, providing his support in the most professional but friendly, demanding but flexible way.

A special thank you goes to Dr. Paolo Beltrame, who I had the pleasure and honour to work with. He has been of great support to my work, as well as being crucial for my professional development.

I am glad and honoured to had the chance to work within the EdiDM group, a place were co-workers become friends, where there is always time for very good science and for very good fun. I thank all the EdiDM crew, past and present, especially Jim, Nicolas, Chiara, and Hassan.

I want to thank all the LUXers and LZers I had the honour to work with, too many to mention. It has been a real pleasure to be part of the University of Edinburgh community, in particular the Nuclear Physics and the Particle Physics Experiment groups, and to share the work place with all my officemates. I would like to thank Prof. Franz Muheim and Dr. Greig Cowan, for supervising my progresses throughout my PhD. A special thought goes to Prof. Marialuisa Aliotta, who has been a reliable mentor and a true friend.

The time spent in Edinburgh would not have been so enjoyable without the people I shared my life with. Thank you Mara, Marco, Francesco, Salvatore, Micaela, Maria, Rosa, William, Piergiorgio, Kevin, Elengo, Stefano, Christos, and all the others. You have been more than friends to me, you have been my family away from home. And I want to thank Barbara and Ciarán, who warmly welcomed me when I first arrived in town.

Thank you Valeria, Federico, Silvia, Daniela, Olivia, Micaela, Gianmarco, Francesco, Federica, Marta, Silvia, Damiano, Lorenzo, Lorenzo, Alessandro, Antonio, Andrea, Simone...for having been by my side, even if miles away.

Silvia, Carlotta...you two are sisters to me. Wherever I am, I know you are there for me, and you will always be.

I would like to thank my family-in-law, Giada, Antonietta, Roberto, Giulia, Federico, and all the others, who have always made me feel home, treating me as a cousin, a daughter, a sister.

My uncles, Alessandro and Antonio, are two special people. Thank you both for loving me as a daughter and always making time for me. And thanks to my aunt, Marilina, for the never ending support and love.

As soon as I started my PhD, my grandpa Alberico and my grandma Marisa passed away. I know you both have been on my shoulder every single day since then, protecting me throughout this adventure. A special thank you goes to my grandma Maria Luisa and my grandpa Vito, for the love and affection, now and ever.

Thank you Alessandra...my sister, my soul sister, my first and best friend. I have loved you since you were in mum's belly, and I will always do...*sempre e per sempre*.

Nothing in my life, not just this thesis, would have been possible without my parents, Antonia and Carlo. They often sacrificed themselves to make me grow up in my dreams and aspirations, and to let me live the life I have always wanted to. They have been a precious example to me, and they have loved me unconditionally. Mum, dad, you are my heroes...I hope to be a parent as you two, when the time will come. I love you.

A deep thank you goes to Gianluca, my best friend, my partner, my place, my future.

Contents

List of Figures

List of Tables

Chapter 1

Introduction

The application of the Scientific Method to provide deep understanding of Nature is one of the great human achievements. Despite the many successes, the puzzle has yet to be completed. Identification of particle dark matter is one of the major missing pieces today. Astrophysical and cosmological hints suggest that ordinary matter only constitutes a small fraction of the overall matter content of the universe. The latest results from the Planck satellite constrain only $\sim 5\%$ of the total energy density to be attributed to baryonic matter, while $\sim 26\%$ of it is due to dark matter and $\sim 69\%$ to dark energy [1].

In addition to astronomical and cosmological motivation, dark matter can also solve several yet open issues in the Standard Model of particle physics and its incompleteness. In fact, the Standard Model cannot incorporate gravity, cannot survive any attempt at unification of all forces, cannot explain why the Higgs boson mass is so fine-tuned, neither what happens up to the Planck scale. This suggests that this model is an incomplete theory of the universe.

Moreover, other open questions still stand. For example, we do not know yet the mass scale and hierarchy of neutrinos, neither whether neutrinos are Dirac or Majorana particles. Being a massive object, the neutrino can either be its own antiparticle (Majorana nature), or not (Dirac nature). If a Majorana mass contribution exists, then neutrinos may participate in lepton number-violating processes. This can possibly explain a matter-antimatter asymmetry in the early universe [2], and give further indication about the incompleteness of the Standard Model.

This chapter presents the history of dark matter, in order to describe how it became a well established explanation for a wide variety of astrophysical observations. We start with the early studies made by Lord Kelvin, and then move onto Zwicky's observations, before describing evidence for dark matter obtained through rotation curves of galaxies, gravitational lensing and cosmological studies. It is worth noticing that dark matter history is composed of two eras: the first, when scientists such as Kelvin and Zwicky thought that there was just more normal matter than visible, and the second, when the need for non-baryonic dark matter arose. While this chapter mainly treats the former, Chapter 2 will cover the latter, by introducing supersymmetric models for dark matter.

The second section of this chapter is dedicated to the evidence for physics beyond the Standard Model. Processes such as double beta decay and double electron capture are discussed as potential indication for a Majorana nature of neutrinos.

An outline of some of the problems rising in the strong sector of the Standard Model completes the chapter. The strong CP violation problem is discussed, as a preamble to axion physics, that will be one of the main topics of this thesis.

1.1 Dark Matter historical overview

Dark matter history has been originally driven by astronomers and cosmologists. The one who made a fundamental step from an ancient to a modern approach to cosmology was Galileo, whose experimental search via telescope showed how the introduction of new technology can reveal new forms of matter in the universe – forms that were previously invisible as not accessable [3]. This take-home message is still relevant to the yet open problem of dark matter.

1.1.1 Prehistory

The hypothesis of invisible objects populating the observed horizon goes back to the early times of astronomy and cosmology, but it was around the end of the nineteenth century that the astronomical community started noticing that the stars were not uniformly distributed on the sky. The question rising at the time was whether some regions were dark because of some stellar opacity, or because

of the presence of absorbing matter.

Lord Kelvin contributed to such a debate, by applying the theory of gases to the Milky Way. His idea was to establish a relationship between galaxy size and stellar velocity dispersion, based on the assumption that stars can be described as a gas of particles, that are subject to gravity. In attempting a dynamical estimate of the amount of dark matter in the Milky Way, Kelvin wrote: "*[...] Many of our stars, perhaps a great majority of them, may be dark bodies.*" [3].

Among the other scientists involved in the study of our galaxy, it is worth mentioning the name of the Dutch astronomer Jacobus Kapteyn. He offered one of the first quantitative models describing the shape and size of the Milky Way. Moving a step forward with respect to Lord Kelvin's approach, Kapteyn worked out a relationship between the motion of the stars and their velocity dispersion, and argued the possible existence of dark matter by estimating the local density of the galaxy.

After studies and observations made by pioneers such as Kelvin, Kapteyn, and many others, the modern era of dark matter began.

1.1.2 Zwicky and the Coma Cluster

In the early 1930's, Fritz Zwicky, an astronomer at the California Institute of Technology, stumbled across an unexpected gravitational effect while studying galaxies motion within the Coma Cluster (Fig. 1.1). From his observation, he found out that the motion of the cluster could be explained by including in his calculations an additional not-directly-observed form of matter. As it caused gravitation, this component of the universe must have been massive, whilst being invisible for telescopes. Zwicky named it "dark matter" [4].

Zwicky's analysis is based on the virial theorem, a classical mechanics theorem stating that the time average of the total kinetic energy of a N-body system is proportional to the time average of the total potential energy:

$$\frac{1}{2}\sum_{i=1}^{N}\langle m_i v_i^2\rangle = -\frac{1}{2}\sum_{i=1}^{N}\langle \mathbf{r}_i \cdot \mathbf{F}_i\rangle, \tag{1.1}$$

where m_i, v_i and $\mathbf{r}_i$ are, respectively, the mass, the velocity and the position

of the ith body with respect to the centre of mass of the system. The force acting on the body is the sum of all the forces that other bodies in the system apply to it, and is called $\mathbf{F}_i$.

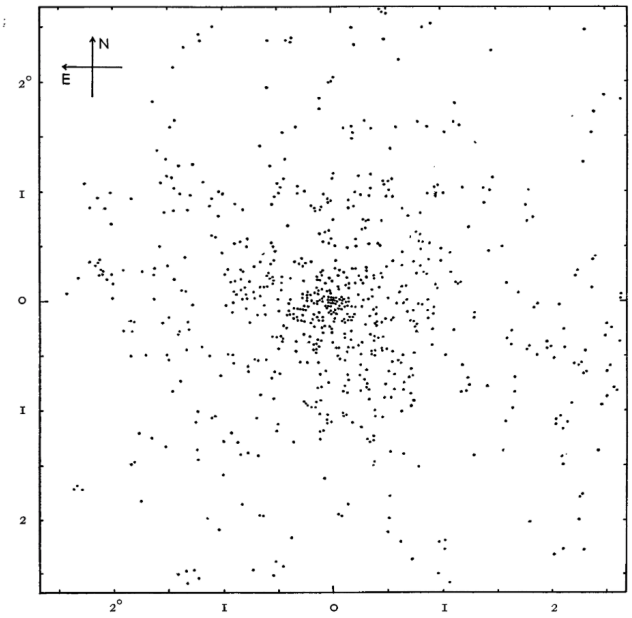

Figure 1.1 *The Coma Cluster of nebulae from the original Zwicky's paper [4].*

Zwicky was the first to use the virial theorem to determine the mass of a galaxy cluster. He firstly estimated the total mass of Coma as the product of the number of observed galaxies in the cluster, 800, and the average mass of a galaxy, 10^9 $M_\odot$ according to Hubble's predictions [1]. Secondly, Zwicky determined the potential energy of the system by estimating its physical size to be approximately 10^6 light years. Applying Eq. 1.1, he eventually calculated the average kinetic energy, and a velocity dispersion of 80 km/s. Such a result though was in contrast with the velocity dispersion of 1000 km/s that was observed looking at the Coma Cluster [3].

A few years later, Zwicky went back to the study of the Coma Cluster, by using the virial theorem in a slightly different way. He assumed that 1000 galaxies were forming Coma, and from the observed velocity dispersion of 700 km/s he estimated the average mass of the galaxy to be larger than 4.5×10^{13} $M_\odot$. This results translates to an average mass of 4.5×10^{10} $M_\odot$ for each of the galaxies forming the cluster. Relying on Hubble's predictions, Zwicky assumed a luminosity for galaxy clusters of 8.5×10^7 $L_\odot$ [2]. The mass-to-light ratio obtained

[1] $M_\odot$ indicates one solar mass.
[2] $L_\odot$ indicates the solar luminosity.

was surprisingly high, $\sim$ 500, providing a first strong evidence for non-luminous matter in the cluster. Scaling Zwicky's result by the current value of the Hubble constant brings the mass-to-light ratio of Coma down to $\sim$ 60, that is still very high.

Further hint about the anomalous mass-to-light ratio of galaxy clusters came from Smith's studies of the Virgo cluster [5]. According to Hubble's prediction, the average mass of the cluster, as obtained from galaxies' luminosities, should have been $\sim 10^9\ M_\odot$. Smith calculated a total mass for Virgo of $10^{14}\ M_\odot$, that divided by 500 observed galaxies, returns an average mass per galaxy of $2 \times 10^{11}\ M_\odot$. The mass-to-light ratio obtained for the Virgo cluster is then $\sim$ 200, of the same order of Zwicky's first result.

1.1.3 Rotation curves

Zwicky's studies of the Coma Cluster also focused on the rotational velocities of the galaxies forming the cluster, and his observations were not in agreement with the expectations based on Kepler's laws of planetary motion. Applying these laws to a case study of a star in circular orbit around the centre of its galaxy, the star experiences an acceleration towards the centre of the galaxy:

$$a = \frac{v^2}{R}, \tag{1.2}$$

where v is its orbital speed, and R is its orbital radius. Given that the acceleration is provided by the gravitational attraction, it can also be expressed as:

$$a = \frac{G\ M(R)}{R^2}, \tag{1.3}$$

where $M(R)$ is the mass contained within a sphere of radius R. Equating Eq. 1.2 to Eq. 1.3, we get an expression for the rotational velocity of the star, as a function of its radial distance from the centre of the galaxy:

$$v = \sqrt{\frac{G\ M(R)}{R}}. \tag{1.4}$$

In the limit of large radii, the luminous mass content of the galaxy, $M(R)$, becomes constant, thus the velocity of an individual component is expected to fall as $v \propto 1/\sqrt{R}$. Observations are in disagreement with this prediction, showing that the orbital velocity of stars tends to stay constant as the radial distance from the centre of the galaxy increases.

Such results were obtained by looking at several galaxies. Taking the Andromeda Galaxy M31 as an example, studies made by H. W. Babcock in the late 1930's [6] are shown in Fig. 1.2. The behaviour of rotational velocities is in disagreement with Kepler's predictions.

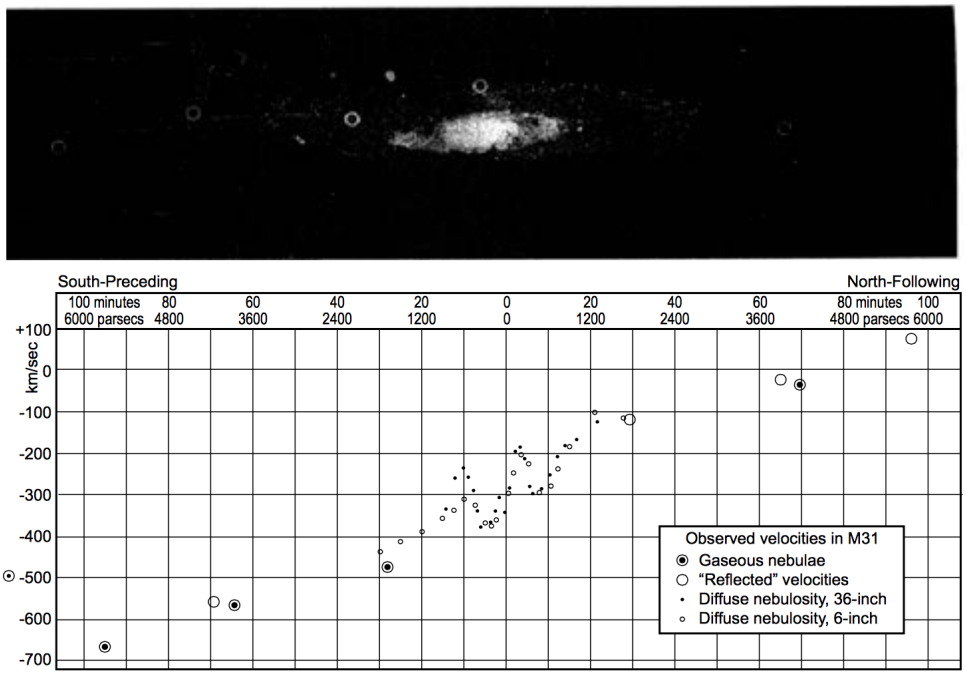

Figure 1.2 *Top panel: a photograph of the Andromeda Galaxy M31. Bottom panel: observed velocities in M31 [6].*

In the 1970's, Rubin and Ford provided more measurements of the Andromeda Galaxy, finding the best value for the mass-to-light ratio to be 12 ± 1 [8]. They also extended their searches to other galaxies, whose rotational velocities presented a constant behaviour at large distance from the centre, as shown in Fig. 1.3.

These results imply that the mass content of galaxies does not become constant at large radial distances, while the ratio $M(R)/R$ in Eq. 1.4 does. This suggests the presence of an additional form of matter beside the luminous one, providing indirect evidence for the existence of a dark matter halo.

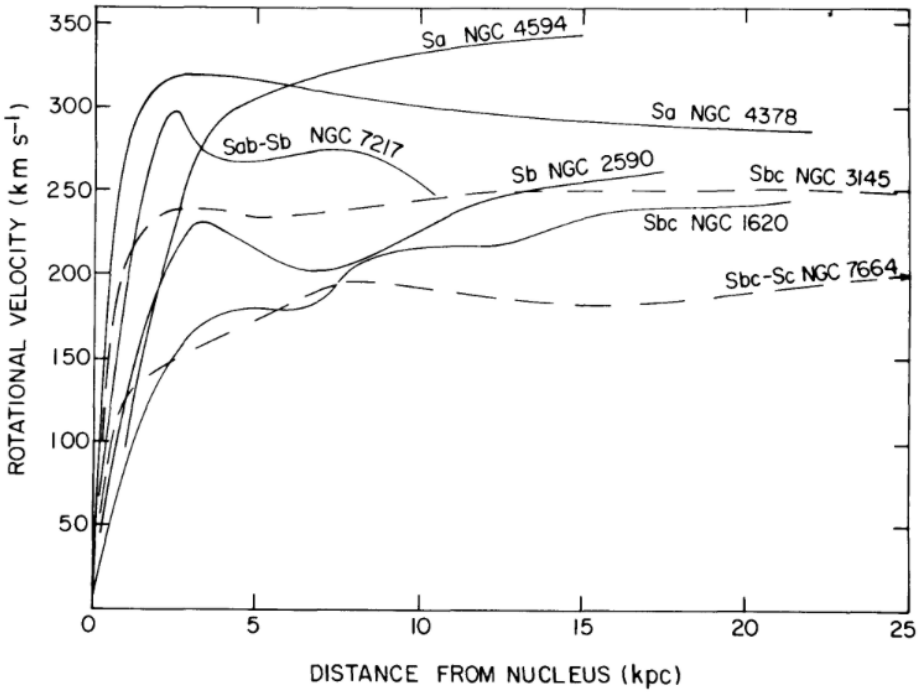

Figure 1.3 *Rotational velocities of seven galaxies, all presenting a constant trend at large distance from the centre [7].*

1.1.4 Gravitational lensing

Einstein's General Relativity provides a unified description of gravity, that is interpreted as a geometric property of space-time. According to Einstein's theory, objects travelling with constant speed move along straight world lines, called "geodesics", while the presence of massive objects creates curvatures in the space-time. The straight path of light then follows the curvature of the space-time, inducing interesting astronomical effects, such as gravitational lensing. This phenomenon occurs when a massive object stands between the observer and the source he is looking at. The image of the source will appear distorted because of the bending of space-time by gravity.

Zwicky was the first one to introduce the idea of nebulae acting as lenses. In order to estimate the mass of a nebula, he proposed to use the deflecting angles that the nebula attributes to radiation [4]. Since then, studies on gravitational lensing have been pursued, giving one more indication of the presence of non-luminous matter in galaxy clusters. Moreover, such gravitational evidence is arguably more robust, given that dark matter is known to interact gravitationally rather than electromagnetically.

Gravitational searches aim at studying images of moving stars or galaxies, to indirectly prove that non-luminous matter has bended the space-time according to Einstein's predictions. If this happens, images will present anomalies due to lensing effects. Depending on their severity, such effects can be categorised in a "strong lensing" to "microlensing" scale.

Strong lensing is quite a rare effect, happening when large distortions of individual background objects lead to arcs and Einstein rings. Weak lensing happens when individual objects have minor distortions, that are only observable when considered as an ensemble. Fluctuations of brightness of a point object due to changes in alignment are known as microlensing. An estimate of any of these lensing effects can be used to determine the mass density of the dark matter halo that produces the observed result.

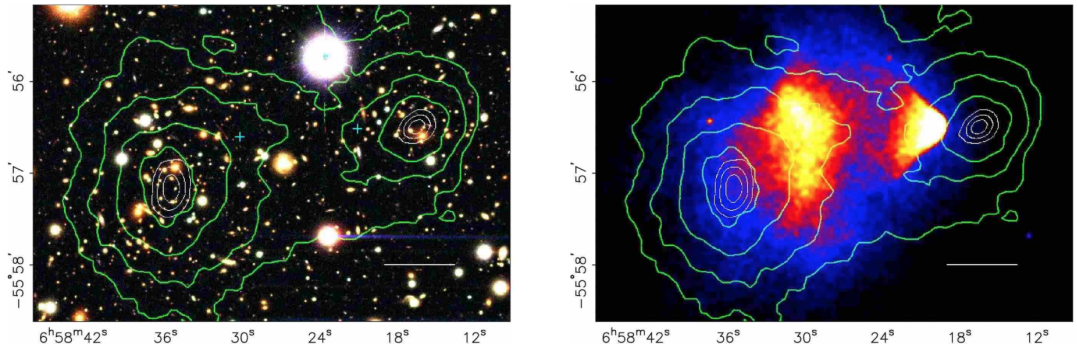

Figure 1.4 *A telescope (left panel) and an x-ray (right panel) image of the bullet cluster 1E0657–558. The former shows the galaxies forming the clusters, the latter shows the bullets with a thermal scale. In both images, mass contours obtained through weak lensing measurements (white and green curves) are shown. Concentric white contours correspond to 68.3%, 95.5%, and 99.7% confidence intervals. The horizontal white bar is drawn at 200 Mpc to indicate the length scale [9].*

A system of two galaxy clusters that have collided, usually known as "bullet cluster", provides an interesting example of weak lensing [9]. In the hypothesis of no dark matter, a cluster is expected to be made of galaxies and intracluster plasma, both having a centrally symmetric distribution. Such a distribution traces the gravitational potential of the cluster. When two clusters interact or merge, x rays are expected to be emitted as the intracluster plasma experiences ram pressure and is thus slowed down, while the galaxies behave as collisionless particles. Plasma and galaxies are therefore expected to decouple with the plasma concentrated in the centre of collision. In the absence of dark matter,

the plasma represents the dominant mass of the cluster, and is responsible for the gravitational potential.

Taking the bullet cluster 1E0657–558 as an example, Fig. 1.4 shows that this is not the case. Indeed, weak lensing measurements indicate that the gravitational potential is not driven by the x ray-emitting plasma, but by collissionless matter that is not interacting electromagnetically.

1.1.5 Cosmic Microwave Background and ΛCDM Model

Beside the astronomical evidence, dark matter is also favoured by cosmological observations. In 1965, Arno Penzias and Robert Wilson, astronomers at the Bell Labs, discovered the Cosmic Microwave Background (CMB), while using a microwave antenna to map the Milky Way. Such a discovery, worth the Nobel Prize in Physics to both of them, is a milestone in experimental cosmology. What Penzias and Wilson happened to be looking at is an isotropic background of microwave radiation, from which extensive information about the universe can be extracted. The discovery of the CMB supports the Big Bang theory of the origin of the universe, and the observation of anisotropies in its temperature provides details about the energy density of the components of the universe.

According to the Big Bang theory, the universe has originated from a very hot and dense state, and then started to expand. When the temperature of the universe was higher than 10^4 K, the universe was a system made of ionised baryonic matter and free electrons, and producing black-body radiation. Many photons were then scattering off free electrons. As the universe expanded, its temperature became lower, cooling down to $\sim$ 3000 K. At this stage ions and electrons started combining to form neutral atoms. Such a process, known as "recombination", reduced the number of free electrons, and consequently the probability of interaction with photons, thus making the universe transparent to photon radiation.

Since its discovery, maps of the CMB have been acquired by the Cosmic Background Explorer (COBE) satellite [10], and by other later experiments, such as the NASA Wilkinson Microwave Anisotropy Probe (WMAP) spacecraft [11], and the ESA Planck observatory [1]. Taken data show that the CMB is accurately fitted by a black-body spectrum, with a temperature $T_0 = 2.72548 \pm 0.00057$ K [12]. The CMB that is visible today can be interpreted as a relic of the black-body

radiation that was filling the early universe. The drop in temperature from $\sim$ 3000 K to $\sim$ 2.7 K can be explained by the expansion of the universe.

Data collected from CMB observations can also be used to constrain theoretical models that describe the content of the universe. Cosmologists analyse temperature anisotropies of the CMB (Fig. 1.5) to determine the abundance of baryons, dark matter, and dark energy.

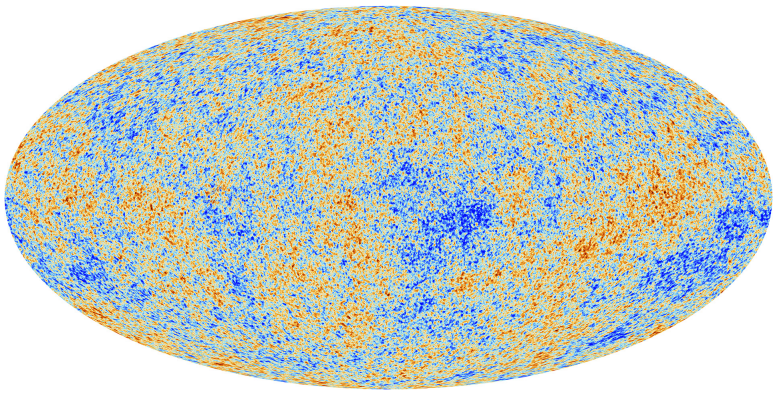

Figure 1.5 *Temperature anisotropies of the Cosmic Microwave Background (CMB) as observed by Planck. Temperature fluctuations correspond to variations in density [1].*

Two variables describe the Big Bang-generated universe: the scale factor, $a = a(t)$, and the curvature constant, κ. The former gives the universe dimension by tracking the increase (or decrease) of cosmic distances over time; the latter indicates the nature of the curvature of the universe, that can be positive ($\kappa = +1$), negative ($\kappa = -1$), or flat ($\kappa = 0$). When Albert Einstein published his theory of General Relativity in 1915, the connection between space-time curvature and energy content was established, as already discussed in this chapter. When applied to cosmology, Einstein's idea opens the way to the so called "ΛCDM model", where Λ is the cosmological constant and CDM stands for cold (*i.e.* non-relativistic at the time of decoupling) dark matter.

The expansion rate of the universe is described by the Hubble parameter, and is the ratio of the time-derivative of the scale factor and the scale factor itself:

$$H(t) \equiv \frac{\dot{a}}{a}. \tag{1.5}$$

CMB observations established that the cosmological constant, Λ, representing the dark energy content, could not be equal to zero, as postulated in past models of universe evolution. The equation linking $a(t)$ and κ to the energy density of the

universe, $\rho(t)$, and to the cosmological constant, Λ, is known as the Friedmann equation:

$$H^2 = \left(\frac{\dot{a}}{a}\right)^2 = \frac{8\pi G}{3}\rho - \frac{\kappa c^2}{a^2} + \frac{\Lambda c^2}{3}, \tag{1.6}$$

where G is the gravitational constant. The critical energy density, ρ_{crit}, for a flat universe can be calculated from Eq. 1.6, setting both κ and Λ to zero:

$$\rho_{crit} = \frac{3H_0^2}{8\pi G}, \tag{1.7}$$

and then it is used to define the density parameters of the ΛCDM model, Ω_i, for each ith component of the universe:

$$\Omega_i \equiv \frac{\rho_i}{\rho_{crit}}. \tag{1.8}$$

Density parameters can be constrained by studying the CMB. Most of the cosmological information comes from the CMB temperature power spectrum, that is presented in Fig. 1.6. Fluctuations in the CMB temperature spectrum are plotted against the multipole moment, l, that is a measure of angular scales on the sky. The oscillating shape of the power spectrum reflects the oscillations in the early universe hot gas, and the peaks are determined by the composition of the universe. The first peak is an indication of the curvature of the universe. As it centred at $l \sim 200$, the universe is spatially flat. If it was at a smaller (higher) multipole moment, the curvature would have been positive (negative). The second peak is determined by the ordinary matter content. In particular, the ratio of heights of the first and the second peak indicates the amount of baryons in the universe. The third peak gives an indication of the dark matter content in the universe, as it is a measure of the mass-to-light ratio. Finally, a flat universe, containing ordinary and dark matter, requires that the remaining mass energy is in the form of dark energy. In fact, without it, the curvature of the universe would have been positive.

The ΛCDM model has been fitted to Planck 2015 CMB data (red curve in Fig. 1.6), delivering limits on the energy density parameters for the overall matter content (Ω_m), for baryons (Ω_b) and dark matter (Ω_{DM}) separately, and for the dark energy content (Ω_Λ). Results are listed in Table 1.1.

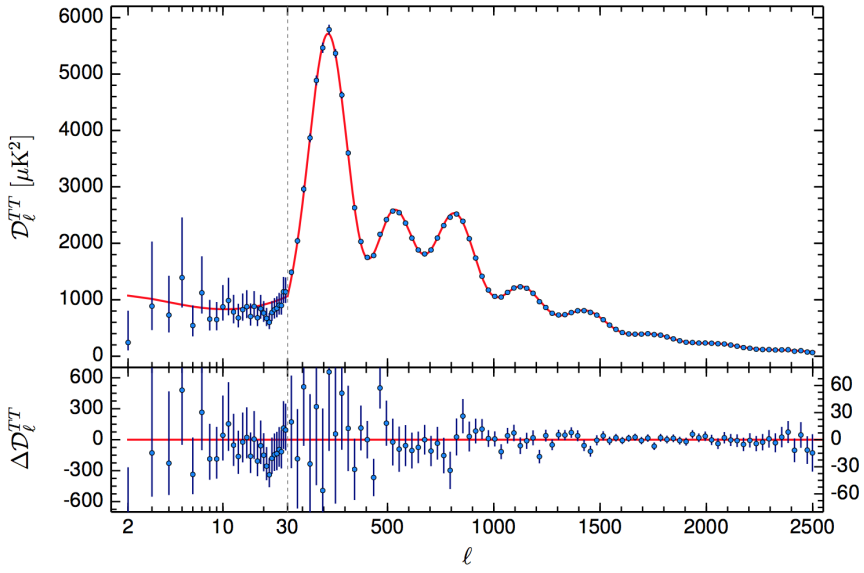

Figure 1.6 *Planck 2015 temperature power spectrum. The first peak is an indication of the curvature of the universe, the second peak reflects the ordinary matter content, while the third peak is determined by the amount of dark matter. The ΛCDM model is fitted to the data (red curve), and the residuals with respect to this model are shown in the lower panel. Error bars are $\pm 1\sigma$ uncertainties [1].*

Parameter	Value	Description
Ω_m	0.308 ± 0.012	Matter density
$\Omega_b h^2$	0.02226 ± 0.00023	Baryonic matter density
$\Omega_{DM} h^2$	0.1186 ± 0.0020	Dark matter density
Ω_Λ	0.692 ± 0.012	Dark energy density

Table 1.1 *Energy density parameters (68% confidence limit) of the ΛCMD model, as measured by using the Planck 2015 CMB temperature power spectrum, combined with lensing reconstruction [1].*

CMB temperature anisotropies have also been used to estimate the Hubble constant, H_0, to be (67.8 ± 0.9) km s^{-1} Mpc^{-1}. H_0 is usually referred to in terms of the parameter $h \equiv H_0/(100$ km s^{-1} Mpc$^{-1})$, known as the reduced Hubble constant. Using this value, Planck's measurements indicate that 69.2% of the overall density is due to dark energy, while 30.8% of it is given by matter, of which only 4.8% is in the form of baryons and 25.8% is dark.

Cosmological parameters have also been estimated using supernovae measurements, as described in Ref. [13].

1.2 Evidence for Physics beyond the Standard Model

Given that 25.8% of the overall energy density of the universe is in the form of non-electromagnetically interacting matter, an obvious hypothesis would be neutrinos to account for it. Neutrinos are electrically neutral and only interact weakly – characteristics that make them promising dark matter candidates. Also, neutrinos are currently the only candidates whose existence has been proven. An overview of other candidates for dark matter will be given in Chapter 2.

Before investigating the possible contribution of neutrinos to the missing dark matter in the universe, it is important to make a distinction between cold and hot dark matter. In the previous section, the Λ model for cold dark matter has been introduced, pointing out that "cold" refers to matter that was non-relativistic at the time of decoupling. On the other hand, neutrinos would accomplish for the "hot" component of dark matter, as they were travelling at relativistic speed being nearly massless.

Since initially postulated by Pauli in 1930, neutrinos have been deeply studied. Today we know that three neutrino (and antineutrino) flavours exist [3], each associated with one of the leptons: ν_e ($\overline{\nu_e}$), ν_μ ($\overline{\nu_\mu}$), and ν_τ ($\overline{\nu_\tau}$). Results from neutrino oscillation experiments prove that neutrinos oscillate between these flavours, and that each flavour state is a superposition of three mass eigenstates (ν_1, ν_2, and ν_3). Such a mixing is obtained through the Pontecorvo-Maki-Nakagawa-Sakata matrix, $U_{\alpha i}$ [14]:

$$\nu_\alpha = \sum_{i=1}^{3} U_{\alpha i} \nu_i, \tag{1.9}$$

where $\alpha = e, \mu, \tau$, and $i = 1, 2, 3$.

In the same way the cosmic microwave background is made of relic photons, relic neutrinos are expected to be everywhere within the universe, providing an

[3] The possibility of a fourth (or further) sterile neutrino is under investigation.

energy density according to Eq. 1.8 [15]:

$$\Omega_\nu = \frac{\rho_\nu}{\rho_{crit}} = \frac{\sum_i m_i}{93.14\ h^2\ eV}, \tag{1.10}$$

where the sum $\sum_i m_i$ is over all neutrino masses.

The squared mass differences between the mass eigenstates have been measured by experiments testing either solar or atmospheric neutrinos. Results are, respectively, $\Delta m^2_{21} \cong 7.4 \times 10^{-5}$ eV^2 and $|\Delta m^2_{31}| \cong 2.5 \times 10^{-3}$ eV^2 [14]. The unknown sign of the latter value is due to the fact that there has been no evidence yet about ν_3 being heavier or lighter than ν_1 and ν_2. This is usually known as the "hierarchy problem", pictured in Fig. 1.7.

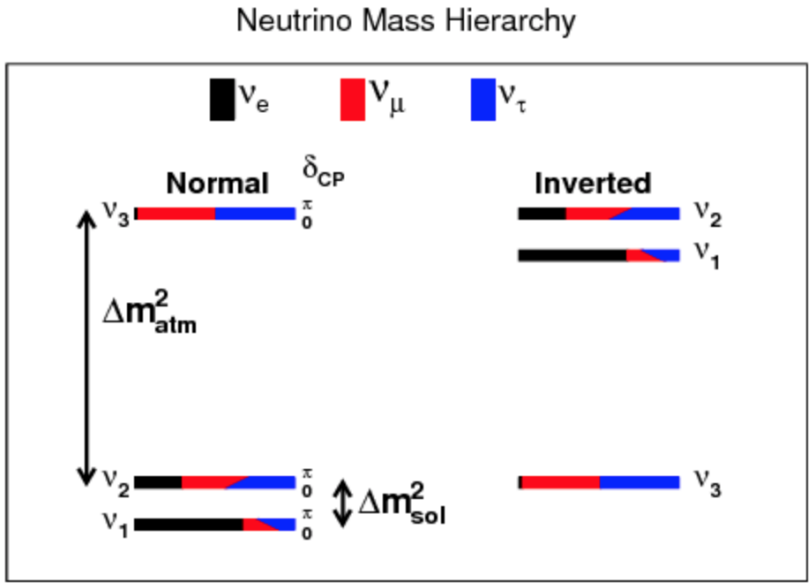

Figure 1.7 *Diagram describing the two alternative hierarchies for neutrino mass eigenstates. The normal hierarchy, on the left, is defined by ν_3 being heavier than ν_1 and ν_2. The inverted hierarchy, on the right, is defined by ν_3 being lighter than ν_1 and ν_2. The colour scale indicates the superposition of flavour states forming each of the mass states [16].*

In order to establish whether neutrinos can address the problem of dark matter, an estimate of Ω_ν is needed. Oscillation experiments provide bounds on the sum of neutrino masses [15], depending on the hierarchy assumed. For the

normal (inverted) hierarchy, the approximate bound reads:

$$0.06\ (0.1)\ eV \lesssim \sum_i m_i \lesssim 6\ eV. \tag{1.11}$$

The upper bound shown in Eq. 1.11 is consistent with the limit of 2 eV that has been set on the mass of the electron neutrino by tritium beta decay experiments [17].

Using Eq. 1.10, the bound on the sum of neutrino masses can be translated to a limit on the energy density of neutrinos:

$$0.0013\ (0.0022) \lesssim \Omega_\nu \lesssim 0.13. \tag{1.12}$$

As we have seen in the previous section, cosmological observations can constrain energy densities. The WMAP collaboration combined their data with some astronomical data, and constrained the energy density in stable neutrinos to be $\Omega_\nu < 0.0147$ (95% C.L.) [18]. Such a result proves that hot dark matter neutrinos cannot contribute for more than 1.47% to the whole dark matter energy density.

Another hint of neutrinos being too light to be dark matter came from the explosion of the Supernova 1987A, when neutrinos arrived almost at the same time as light. Their velocity has been used to put a limit on their mass, that seems to be much smaller than required for neutrinos to account for dark matter [19].

Even if neutrinos cannot address the problem of missing dark matter, they are still particles of great interest, as questions on their nature are yet to be answered. This section presents an overview of some of the processes that are currently studied in order to answer these questions.

1.2.1 Nature of neutrinos: Dirac or Majorana?

One of the main open questions about neutrinos is pictured in Fig. 1.7: how their mass eigenstates are ordered still has to be determined. Such information would also give indications about their nature. Being proven to be massive, the neutrino could either have a Majorana nature (*i.e.* being the same as its antiparticle, $\nu = \overline{\nu}$), or be a Dirac particle (*i.e.* being distinct from it, $\nu \neq \overline{\nu}$). Almost all extensions

of the Standard Model of particle physics predict a Majorana component for the neutrino mass [20].

The left-handed Majorana mass term can be built out of a left-handed neutrino field, ν_L, and its charge conjugate, ν_L^C [21]:

$$\mathcal{L}_L = m_L \overline{\nu_L} \nu_L^C. \tag{1.13}$$

$\mathcal{L}_L$ mixes a particle with its antiparticle as it absorbs a $\overline{\nu_R}$ and creates a ν_L. A Majorana mass term is then possible only if charge and lepton number are not conserved. While charge conservation is not a problem for neutral particles such as neutrinos, lepton number conservation only allows for Dirac neutrinos. On the other hand, unlike electric charge conservation, there is not a strong reason why lepton number should be conserved. If neutrinos are Majorana particles, they may take part to lepton number-violating processes – processes that, if observed, would give evidence for physics beyond the Standard Model.

1.2.2 Neutrinoless double beta decay

The most widely chosen approach to probe the Majorana nature of neutrinos is the search for neutrinoless double beta decay ($0\nu\beta\beta$). This process, if observed, would confirm that neutrinos have a Majorana mass component. Moreover, it would also provide useful information on the neutrino mass scale and hierarchy.

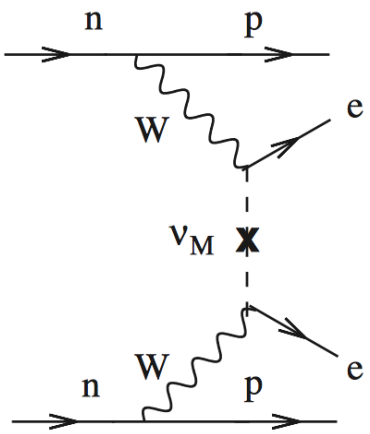

Figure 1.8 *Feynman diagram for $0\nu\beta\beta$ decay. The process can happen through the exchange of a Majorana neutrino, ν_M [22].*

Neutrinoless double beta decay is a nuclear transition that is not allowed

within the Standard Model. Figure 1.8 shows the Feynman diagram of the process, where a nucleus (A, Z) decays to $(A, Z+2)$ emitting two electrons:

$$(A, Z) \rightarrow (A, Z+2) + 2e^{-}. \tag{1.14}$$

This process violates lepton number conservation by two units, and happens if a Majorana neutrino, ν_M, is exchanged [4]. The reaction can be interpreted as if a right-handed antineutrino is emitted in the first vertex and a left-handed neutrino is absorbed in the second. The other requirement for such a decay to happen is that the antineutrino has a left-handed component. Since this component is proportional to the neutrino mass, such a condition is satisfied, as demonstrated by neutrino oscillation experiments.

The rate of $0\nu\beta\beta$ decay is approximately [22]:

$$\left(T^{0\nu}_{1/2}\right)^{-1} \;=\; G_{0\nu}(Q_{\beta\beta}, Z)\; |M_{0\nu}|^2\; \langle m_{\beta\beta}\rangle^2. \tag{1.15}$$

$G_{0\nu}(Q_{\beta\beta}, Z)$ is the phase space factor for the emission of the two electrons, depending on the Q value of the reaction and on the nucleus taking part to the process. $M_{0\nu}$ is the nuclear matrix element of the decay. The third factor in Eq. 1.15 is known as the effective Majorana mass of the electron neutrino, and is defined as:

$$m_{\beta\beta} \equiv |\sum_{i=1}^{3} m_i U^2_{\alpha i}|, \tag{1.16}$$

where m_i are the mass eigenstates, and $U_{\alpha i}$ is the mixing matrix defined in Eq. 1.9. For a given nucleus, $G_{0\nu}(Q_{\beta\beta}, Z)$ is determined by kinematics and is exactly calculable. On the other hand, the estimate of the nuclear matrix element, $M_{0\nu}$, relies on the assumption of a theoretical model. A measurement on the half life, $T^{0\nu}_{1/2}$, would then return a model-dependent interval of allowed values for the effective Majorana mass, $m_{\beta\beta}$. Nevertheless, the observation of a $0\nu\beta\beta$ decay would certainly prove the Majorana nature of neutrinos, as well as the non conservation of the lepton number.

[4] This is the minimal mechanism a $0\nu\beta\beta$ decay can happen through. There are other options available, but they require more than a Majorana neutrino.

The expected energy spectrum for $0\nu\beta\beta$ decay is drawn in Fig. 1.9 as a black solid curve. With no neutrinos in the final state, the process is expected to be detected as a mono-energetic line (only smeared by experimental resolution), as the energies of the two electrons are summing up at the Q value. For comparison, Fig. 1.9 also includes the spectrum for the Standard Model-allowed $2\nu\beta\beta$ decay (dotted curve), that is a continuous distribution between 0 and the Q value of the reaction.

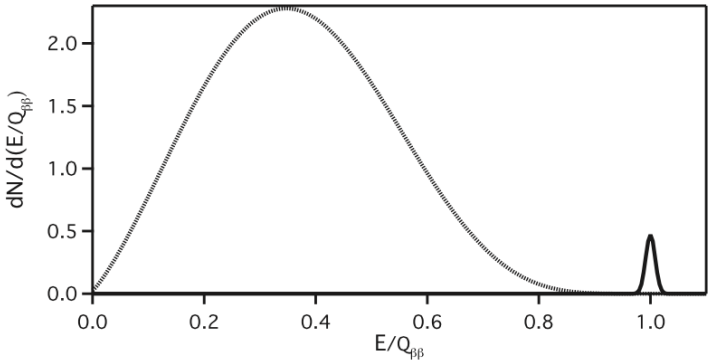

Figure 1.9 *The energy spectrum for $0\nu\beta\beta$ decay (solid curve) as compared with a $2\nu\beta\beta$ decay (dotted curve). If neutrinos are emitted, the shape of the curve indicates a three-body decay, and the energies of the electrons follow a distribution with end-point at the Q value of the reaction. On the other hand, in the neutrinoless case, the electron energies would sum up at $Q_{\beta\beta}$. For this plot, $\Gamma_{0\nu}$ is 1% of $\Gamma_{2\nu}$ and a 2% energy resolution has been assumed [22].*

Neutrinoless double beta decay has yet to be detected, and is currently searched for in several different experiments. Techniques vary, from tellurium bolometers to germanium detectors, as there is more than one candidate isotope. Among them, xenon can also be considered. Xenon is the target material for detectors such as LUX and LZ, but neutrinoless double beta decay searches in these experiments are not the focus of this work, and thus will not be discussed.

1.2.3 Neutrinoless double electron capture

Although the most common channel to investigate the nature of neutrinos is the neutrinoless double beta decay, the inverse process has been proposed as a valid alternative. The observation of neutrinoless double electron capture ($0\nu DEC$) would indicate a Majorana contribution to neutrino mass.

The Feynman diagram for $0\nu DEC$ is shown in Fig. 1.10. A nucleus (A, Z) captures two electrons to become $(A, Z-2)$:

$$(A, Z) + 2e^- \rightarrow (A, Z-2). \tag{1.17}$$

The process can happen without emission of neutrinos, if a Majorana neutrino is exchanged, and lepton number conservation is violated by two units.

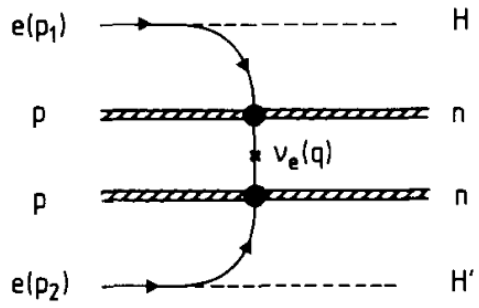

Figure 1.10 *Feynman diagram for resonant $0\nu DEC$: a nucleus (A, Z) captures two electrons, leaving the daughter nucleus in a final excited state, $(A, Z-2)^*$, with two atomic vacancies, H, H'. The process can happen without emission of neutrinos, if a Majorana neutrino is exchanged [23].*

The Q value for the reaction in Eq. 1.17 must satisfy the condition: $Q = M(A, Z) - M(A, Z-2) > 0$. Moreover, in order to have a hope of seeing this process, the Q value for the single electron capture should be negative.

Two processes can lead from the initial to the final state of Eq. 1.17. A *radiative* $0\nu DEC$ happens if one of the two electrons radiates while approaching the nucleus [24]. A *resonant* $0\nu DEC$ takes place when the capture of the two electrons leaves the daughter nucleus in a final excited state, $(A, Z-2)^*$, with two atomic vacancies, H, H'. The final atom radiates and one electron vacancy is filled by outer electrons [23, 25].

The rate of any $0\nu DEC$ process is proportional to four terms [26]:

$$\left(T_{1/2}^{0\nu DEC}\right)^{-1} \propto G_{0\nu DEC} \, |M_{0\nu DEC}|^2 \, \langle m_{\beta\beta} \rangle^2 \, \frac{\Gamma}{\Delta^2 + \Gamma^2/4}. \tag{1.18}$$

$G_{0\nu DEC}$ is the probability that a bound electron is found at the nucleus, $M_{0\nu DEC}$ is the nuclear matrix element, and $m_{\beta\beta}$ is the effective Majorana mass.

The last factor in Eq. 1.18 is built out of $\Delta \equiv |Q - E|$, and Γ. The former is known as the degeneracy parameter, and is the difference between the mass difference between ground state atoms, $Q = M(A, Z) - M(A, Z - 2)$, and the total excitation energy, $E \simeq E^* + E_H + E_{H'}$. The latter is the total width of the reaction, $\Gamma \simeq \Gamma^* + \Gamma_H + \Gamma_{H'}$. The superscripted * and the subscripted $_{H,H'}$ indicate, respectively, the excited daughter nucleus and the electronic vacancies [23].

As the effective Majorana mass appears in both Eq. 1.15 and Eq. 1.18, both processes would prove neutrino Majorana nature, as well as give information on the neutrino mass scale and hierarchy. The reason why $0\nu\beta\beta$ decay is preferred over $0\nu DEC$ is that the lifetime for the latter is generally expected to be several orders of magnitude larger than for the former. This is mainly true for the radiative process. However, a close degeneracy of the initial and final (excited) atomic states, characteristic of the resonant $0\nu DEC$, could enhance the decay rate by up to a 10^6 factor (c.f. Eq. 1.18) [23]. For this reason, experimental searches focus on the resonant $0\nu DEC$, yet to be observed.

1.2.4 Two-neutrino double electron capture

According to the Standard Model of particle physics, the simultaneous capture of two electrons, accompanied by the emission of two neutrinos, is allowed, and is shown diagrammatically in Fig. 1.11. This nuclear process is called two-neutrino double electron capture ($2\nu DEC$):

$$(A, Z) + 2e^- \rightarrow (A, Z - 2) + 2\nu_e, \tag{1.19}$$

and its rate can be expressed as [27]:

$$\left(T_{1/2}^{2\nu DEC}\right)^{-1} = \frac{a_{2\nu DEC}\ F_{0\nu DEC}\ |M_{2\nu DEC}|^2}{ln(2)}. \tag{1.20}$$

The rate is proportional to a dimensional factor, $a_{2\nu DEC} \sim 2 \times 10^{-22}$ y^{-1}, to the phase space factor, $F_{0\nu DEC} \propto Q^5$, and to the nuclear matrix element, $M_{2\nu DEC}$.

The reason why such a standard process is included in this section, dedicated to evidence for physics beyond the Standard Model, relies on the nuclear

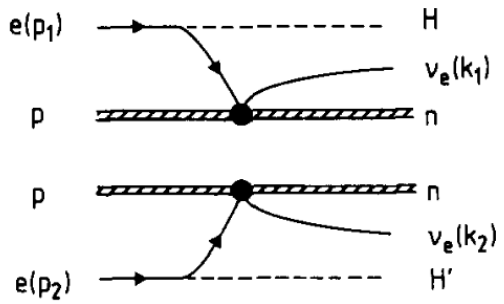

Figure 1.11 *Feynman diagram for $2\nu DEC$: a nucleus (A, Z) captures two electrons to become $(A, Z-2)$. Two atomic vacancies are left, and two neutrinos are emitted [23].*

matrix element. Calculations of nuclear matrix elements cannot be done model-independently, as they rely on the chosen nuclear structure theory. The relationships between nuclear matrix elements of double beta decay and double electron capture have been widely studied [28–31]. Although nuclear matrix elements vary among different processes, the calculation framework may be the same. Thus, within a chosen model framework, matrix elements can be constrained one by another. Moreover, a measurement of any of the nuclear matrix elements, could be used to check the accuracy of theoretical predictions on any other process. For example, measurement of a $2\nu\beta\beta$ decay rate will help constrain the nuclear matrix calculation for $0\nu\beta\beta$.

Searches for $2\nu DEC$ would contribute as an input to the calculation of nuclear matrix elements for the proton-rich side of the mass parabola for even-even isobars [32]. Observations of $2\nu DEC$ have been made only in ^{78}Kr [33] and ^{130}Ba [34, 35], with measured lifetimes in the range of $(6 - 92) \times 10^{20}$ years. Detection of this process is not easy, because only x rays and Auger electrons are emitted, and their energies usually fall in the background-dominated region of the experimental spectrum ($\sim 1 - 100$ keV) [27]. Interest and effort in such searches are currently growing, mainly driven by low-background experiments such as the ones developed for dark matter searches.

1.3 Problems in the strong sector of the Standard Model

This last section of the chapter is dedicated to a couple of problems that arose in the strong sector of the Standard Model of particle physics in the 1970's. We discuss how the solution to the $U(1)_A$ problem, an issue rising from the Lagrangian of strong interactions, opened another fundamental problem. Still to be solved, it is known as strong CP violation problem of quantum chromodynamics (QCD).

1.3.1 The $\mathbf{U(1)_A}$ problem

The QCD Lagrangian for N flavours reads:

$$L_{QCD} = \overline{\psi}(i\gamma^\mu D_\mu - m)\psi - \frac{1}{4}G^{a\mu\nu}G^a_{\mu\nu}, \tag{1.21}$$

where $D_\mu = \partial_\mu - igA^a_\mu t^a$ is the covariant derivative, and $G^a_{\mu\nu} = \partial_\mu A^a_\nu - \partial_\nu A^a_\mu + g f_{abc} A^b_\mu A^c_\nu$ are the field strength tensors of the gluon fields, A^a_μ. The first two terms in Eq. 1.21 describe, respectively, the kinetic energy and the mass of the quarks, while the third tracks the gluon dynamics.

Such a Lagrangian is expected to have an $U(2)_V \times U(2)_A$ symmetry, but, while $U(2)_V$ is observed [5], $U(2)_A = SU(2)_A \times U(1)_A$ is not. The $SU(2)_A$ symmetry is spontaneously broken, with pions being the corresponding Nambu-Goldstone bosons. On the other hand though, there are no Nambu-Goldstone candidates for spontaneous breaking of $U(1)_A$. A potential solution to this problem has been discovered through the introduction of anomalous axial currents.

[5] $U(2)_V = SU(2)_V$ x $U(1)_V$ is a good symmetry of nature, corresponding to isospin and baryon number.

1.3.2 The strong CP problem

The $U(1)_A$ problem might be solved by introducing an extra term in the QCD Lagrangian [36]:

$$L_\theta = \frac{\alpha_S \theta}{8\pi} G^a_{\mu\nu} \widetilde{G}^{a\mu\nu}, \tag{1.22}$$

where $\widetilde{G}^{a\mu\nu} \equiv \frac{1}{2}\epsilon^{\mu\nu\alpha\beta} A^a_{\alpha\beta}$. Such a term, proportional to the divergence of the axial current, violates the PT (*i.e.* parity-time) symmetry, but conserves C (*i.e.* charge conjugation). This makes it a CP violating term. If beside QCD we also include the weak interactions, one more term is added to the Lagrangian:

$$L_m = \frac{\alpha_S Arg(detM)}{8\pi} G^a_{\mu\nu} \widetilde{G}^{a\mu\nu}, \tag{1.23}$$

where M is the quark mass matrix. Diagonalising this matrix leads to a chiral transformation, that changes θ by $Arg(detM)$. Defining a new parameter, $\overline{\theta} \equiv \theta + Arg(detM)$, the Lagrangian in Eq. 1.21 becomes [36]:

$$L_{QCD} = \overline{\psi}(i\gamma^\mu D_\mu - m)\psi - \frac{1}{4} G^{a\mu\nu} G^a_{\mu\nu} + \frac{\alpha_S \overline{\theta}}{8\pi} G^a_{\mu\nu} \widetilde{G}^{a\mu\nu}. \tag{1.24}$$

Although the Lagrangian in Eq. 1.24 includes a CP violating term, strong interactions do not seem to break CP symmetry. For example, CP violation in the strong sector would create an electric dipole moment of the neutron of the order of 10^{-18} e cm [37, 38]. This has been ruled out by experimental observations, given that the most recent upper limit on the magnitude of the neutron electric dipole moment is 3.0×10^{-26} e cm (90% C.L.) [39].

Such an experimental result implies that the parameter $\overline{\theta}$ in Eq. 1.24 must be very small. In principle, this parameter may take a value anywhere in the range 0 to 2π, thus its small value indicates a severe case of fine tuning. This is known as strong CP violation problem. A solution has been proposed by Peccei and Quinn, and will be presented in Chapter 2. They introduced a new symmetry and a new field, called the axion field, that beside ensuring the conservation of CP in the strong sector, also happens to be a well motivated candidate for dark matter.

Chapter 2

Possible theoretical solutions

The previous chapter has focused on the astronomical and cosmological evidence for the presence of dark matter in the universe. According to the observations, only 4.8% of the total energy density is in the form of baryons. The incompleteness of the Standard Model of particle physics has also been discussed, and potential extensions of it have been mentioned.

Chapter 1 leaves a list of yet-to-answer questions. If dark matter does exist, what is it made of? If the Standard Model is an incomplete theory, how can it be extended to fully describe the universe? Are the proposed theoretical solutions compatible with each other?

This chapter is an attempt to address these questions. Baryonic dark matter, weakly interacting massive particles, axions and axion-like particles are introduced. Some of the theoretical models that are proposed to extend the Standard Model will be also presented.

2.1 Dark Matter candidates

As broadly described in Chapter 1, there is strong evidence from a variety of different observations that dark matter exists. On the other hand, it is well established that dark matter cannot be seen as easily as we can observe other particles. Astronomical and cosmological evidence only derives from the gravitational interaction of dark matter with visible particles, thus the available

information to build a model for dark matter is limited.

Even if not enough to establish what dark matter is, such information can give a few useful guidelines in the theoretical modelling of potential candidates. First of all, a suitable dark matter candidate must have at most very weak electromagnetic interactions with Standard Model particles. Dark matter is subject to gravitational interaction and is almost collision-less. The required galactic distribution indicates that dark matter candidates have likely been produced in the early universe, so they must either be stable, or have lifetimes comparable or larger than the age of the universe.

Neutrinos have been proposed as hot dark matter candidates (c.f. Chapter 1). Although their characteristics make them suitable candidates, bounds on neutrino energy density reveal that they can only contribute up to 1.47% to the overall percentage of missing dark matter [18]. Moreover, simulations of cosmological models set very stringent constraints on hot dark matter [40]. Having ruled out the only candidate whose existence has been proven, the hunt for dark matter is open, aiming at balancing observations, predictions and experimental challenges.

2.1.1 Baryonic dark matter

At the early stages of the search for dark matter, the idea of dark matter halos being made of baryons had been considered, but such an option has now been ruled out by several observations, as described below.

Studies on Big Bang nucleosynthesis revealed a good agreement with the standard cosmological model. The synthesis of light elements, such as D, ^{3}He, ^{4}He and ^{7}Li, began about 1 s after the Big Bang. Astrophysical objects are characterised by very high temperatures, so they cannot be sites for production of deuterium, a lightly bound atom that dissociates back to a proton and a neutron in a hot thermal environment. For this reason, deuterium necessarily originated in the Big Bang, and stayed in the interstellar gas. Observations today therefore provide a direct link to Big Bang production, with the highest observed abundances corresponding to the minimum (effectively zero) stellar depletion. The analysis of the deuterium to hydrogen ratio in this gas has been used to establish their original concentration, leading to a constraint on the baryonic matter density in the universe of 1.7×10^{-31} to 4.1×10^{-31} g/cm^3 [41]. This corresponds to about 1% to 15% of the critical density, indicating that most of

the dark matter is non-baryonic.

A massive compact halo object (MACHO) is a baryonic astronomical body that does not emit radiation. Such non-luminous objects could in principle account for missing dark matter in the universe. MACHOs can be detected by exploiting gravitational microlensing, as they are expected to deflect light coming from further sources. Microlensing surveys looked at both the Large [42] and the Small Magellanic Cloud [43], and yielded limits on the amount of dark matter made of MACHOs. Quantitatively, results impose that objects with masses between 2×10^{-7} $M_{\odot}$ and 1 $M_{\odot}$ cannot compose more than 25% of the dark matter halo.

As an example of MACHOs, it is interesting to mention the case of brown dwarfs, star-like objects too small to reach the temperatures needed for nuclear fusion reactions. These "failed stars" have finally been observed, after being searched for for many years. Such a discovery has been a success, as in confirming many predictions about these astronomical objects. On the other hand though, the data indicate that there are not enough brown dwarfs to contribute significantly to the missing dark matter [44].

Also primordial black holes belong to the class of MACHOs. They are hypothetical types of black hole, expected to be formed at the early stages of the Big Bang. Firstly proposed in the 1970's, these objects have all the characteristics to be potential candidates for dark matter. Limits on their abundance have been set. Even though they have been initially ruled out, recent analyses show that primordial black holes can still be valid in a certain mass range [45].

With baryonic dark matter being ruled out as main component of dark matter halos, other candidates have been proposed and searched for. Among several yet-to-be-discovered candidates for non-baryonic cold dark matter, weakly interacting massive particles and axions are the most widely accepted.

2.1.2 Weakly Interacting Massive Particles

The class of weakly interacting massive particles (WIMPs) includes stable (or long-lived) massive particles, expected to have been produced in the early universe and to weakly interact with ordinary matter. WIMPs, conventionally indicated as χ, are the most favourite candidate for cold dark matter.

Within the framework of the Big Bang theory for the formation of the universe, when temperatures were high ($T \gg m_\chi$), the abundance of WIMPs would have been high as well. At that time, WIMPs (χ) and ordinary particles (l) were continuously produced and annihilated, taking part to the $\chi\overline{\chi} \longleftrightarrow l\bar{l}$ process. The annihilation rate of WIMPs can be expressed as $\Gamma = \langle\sigma_A v\rangle n_\chi$, where σ_A is the total annihilation cross section of $\chi\overline{\chi}$ into lighter particles, v is the relative velocity, $\langle ...\rangle$ indicates the thermal average, and n_χ is the number density of WIMPs. The drop in temperature ($T < m_\chi$) caused by the expansion of the universe led to an exponential drop in n_χ. As a consequence, the annihilation rate of χs dropped below the expansion rate (Eq. 1.5), $\Gamma \lesssim H$, bringing WIMP annihilation era to an end. At this time, the number density of χs reached the equilibrium, and since then WIMPs abundance will have remained roughly constant [46].

One of the main reasons why WIMPs are a well established candidate for dark matter is that the current abundance of dark matter can be expressed in terms of the WIMP annihilation cross section [46]:

$$\Omega_\chi h^2 = \frac{m_\chi n_\chi}{\rho_{crit}} \simeq \frac{3 \times 10^{-27}\ cm^3 s^{-1}}{\langle\sigma_A v\rangle}. \tag{2.1}$$

Equation 2.1 holds if the annihilation cross section, σ_A, does not depend on the velocity, v. Referring to Table 1.1, a value of $\langle\sigma_A v\rangle \approx 3 \times 10^{-26}$ cm^3 s^{-1} would be needed to obtain the current density of dark matter. It is a very tempting coincidence that this is roughly what expected for a weakly interacting particle with a mass of ~ 100 GeV. Such a particle is predicted by supersymmetry (SUSY), a symmetry of the space-time that has been proposed to accomplish the unification of the gravitational, electroweak and strong forces.

Supersymmetric theories are extensions of the Standard Model of particle physics that require the existence of a supersymmetric partner for each of the Standard Model particles: leptons (*sleptons*), quarks (*squarks*), gauge bosons (*gauginos*), Higgs bosons (*higgsinos*) [47]. Superpartners are copies of their counterparts, apart from their spin differing by a half integer. The R-parity is a new quantum number, introduced to prevent proton decay in supersymmetric theories: $R = 1$ for Standard Model particles, while $R = -1$ for SUSY counterparts [1]. Supersymmetry is expected not to be an exact symmetry of

[1] The R-parity is defined as $R = (-1)^{3(B-L)+2S}$, where B and L are, respectively, the baryon and lepton number, while S is the spin [46].

nature, as if this was the case we should have observed superparticles by now. SUSY must then be spontaneously broken, resulting in heavier superpartners than their counterparts.

The theoretical assumption of SUSY is that as the expansion of the early universe led to sufficiently low temperatures, the heavier particles decayed into lighter ones, such that just the lightest supersymmetric particle (LSP) was left. At that time, the LSP was subject to pair annihilation only. In models where R-parity is conserved, the LSP is stable, so that it becomes an attractive candidate for WIMP dark matter. Most probably the LSP is a superposition of neutral gauginos and higgsinos [47].

WIMPs are proposed to elastically collide with ordinary matter, inducing recoils of atomic nuclei. This principle is what is exploited in most of the experimental searches for dark matter, as will be described in Chapter 3. Chapter 4 contains further details about the signal that is expected from WIMP interactions.

2.1.3 Other dark matter candidates

There are several hypotheses on the nature of the LSP. Although it is widely thought to be a WIMP, according to other models it may well be a gravitino [48]. In supergravity, gravitinos are the counterparts of gravitons, that are the hypothetical mediators of the gravitational force in quantum field theory. Although the LSP gravitino can be a good candidate for cold dark matter when it acquires a non-zero mass via spontaneous breaking of supersymmetry, it would have such low interaction cross section that a detection seems almost impossible.

While WIMPs are expected to be a thermal relic of the early universe, non-thermal dark matter states, called WIMPzillas, have also been proposed. Being named after their much heavier masses than the weak scale, WIMPzillas are thought to be produced at early stages of the expansion of the universe. If they have masses of about 10^{13} GeV and are stable, then the abundance of WIMPzillas would be enough to give a unitary total density to the universe [49].

Initially introduced to solve a problem of QCD, the axion is another well motivated candidate for dark matter. Axion's supersymmetric counterpart, the axino, could also be a candidate. The next section of this chapter is entirely

dedicated to axions, as well as to other particles predicted by extensions of the Standard Model of particle physics, all of primary interest given the scope of this thesis.

The discussion on dark matter candidates presented in this chapter is far from being exhaustive. Nevertheless, it gives a reasonable insight into the huge variety of proposed solutions to the problem of missing dark matter in the universe.

2.2 Axions and Axion-like particles

Having been proven to give quite a valid description of nature, the Standard Model of particle physics is also known to be incomplete. As mentioned in Chapter 1, many theories have been proposed to extend this model by introducing new symmetries and new particles. A first example is supersymmetry, a well established gateway to dark matter, as discussed in the previous section.

Extensions of the Standard Model are many, and not all of them aim at solving the dark matter problem. Being the description of all the possibilities outside the scope of this work, this section only focuses on axions and axion-like particles, as they will play a fundamental role in the rest of this thesis.

2.2.1 Axions

The physics of axions started in 1977, when Peccei and Quinn proposed a solution to the strong CP violation problem. This issue originates from the CP violating term contained in the Lagrangian for QCD (Eq. 1.24), combined with no violation of CP observed in the strong sector.

Peccei and Quinn introduced a global symmetry, named after them, $U(1)_{PQ}$, that is spontaneously broken at some large energy scale, f_a. The Nambu-Goldstone boson generated by this process is the axion, $a(x)$, a field that transforms under $U(1)_{PQ}$ as:

$$a(x) \rightarrow a(x) + \alpha f_a, \tag{2.2}$$

where α is the phase of the field. In the original Peccei-Quinn model, $f_a = v_F$, where $v_F \simeq 250$ GeV is the electroweak scale.

When we add the axion field to the Lagrangian in Eq. 1.24, three more terms appear [36]:

$$\begin{aligned} L = \overline{\psi}(i\gamma^\mu D_\mu - m)\psi - \frac{1}{4}G^{a\mu\nu}G^a_{\mu\nu} + \frac{\alpha_S\overline{\theta}}{8\pi}G^a_{\mu\nu}\widetilde{G}^{a\mu\nu} \\ - \frac{1}{2}\partial_\mu a\partial^\mu a + L_{int}[\partial^\mu a/f, \psi] + \frac{a}{f_a}\xi\frac{\alpha_S}{8\pi}G^a_{\mu\nu}\widetilde{G}^{a\mu\nu}. \end{aligned} \tag{2.3}$$

They describe, respectively, the axion kinetic energy, the axion interaction, and the chiral anomaly of the $U(1)_{PQ}$ symmetry. The last term also behaves as an effective potential for the axion field. Its minimum, known as Peccei-Quinn solution, falls at $\langle a\rangle = -f_a\overline{\theta}/\xi$ [36]. Defining the physical axion as $a_{phys} \equiv a - \langle a\rangle$, the third term in Eq. 2.3 cancels. As this term is the only one containing the parameter $\overline{\theta}$, therefore responsible for CP violation, the axion field provides a dynamical solution to the strong CP problem.

The Lagrangian for QCD proposed by Peccei and Quinn conserves the CP symmetry, and reads [36]:

$$\begin{aligned} L = \overline{\psi}(i\gamma^\mu D_\mu - m)\psi - \frac{1}{4}G^{a\mu\nu}G^a_{\mu\nu} \\ - \frac{1}{2}\partial_\mu a_{phys}\partial^\mu a_{phys} + L_{int}[\partial^\mu a_{phys}/f, \psi] + \frac{a_{phys}}{f_a}\xi\frac{\alpha_S}{8\pi}G^a_{\mu\nu}\widetilde{G}^{a\mu\nu}. \end{aligned} \tag{2.4}$$

When the Peccei-Quinn symmetry is spontaneously broken, the axion acquires a mass, m_a, that is inversely proportional to the energy scale, f_a, and can be expressed in terms of the pion mass by use of Dashen's theorem [50, 51]:

$$m_a = \frac{z^{1/2}}{1+z}\,\frac{f_\pi m_\pi}{f_a} = \frac{6.0\ eV}{f_a/10^6\ GeV}. \tag{2.5}$$

In this equation, $f_\pi = 93$ MeV is the pion decay constant, m_π is the neutral pion mass, and $z = m_u/m_d = 0.56$ is the mass ratio of up and down quarks.

In 1978, Weinberg [52] and Wilczek [53] identified the physical axion with a neutral pseudoscalar boson, with mass of order 100 keV to 1 MeV. If axions had this mass, then they would have couplings large enough to be experimentally detected, by using several different approaches (searches for axion production at reactors, nuclear deexcitation experiments, beam-dump experiments) [54]. As all the results were null, the originally postulated axion, arising from symmetry

breaking at electroweak scales, was ruled out.

Nevertheless, negative experimental results are not in conflict with axions produced via spontaneous breaking of the Peccei-Quinn symmetry at a much higher energy scale, $f_a \gg v_F$. Usually known as "invisible" axions, the corresponding axions would be very light (c.f. Eq. 2.5) and have very weak couplings to other particles. These couplings are inversely proportional to f_a, and their strength is model dependent. Two main invisible axion models exist: the Dine-Fischler-Srednicki-Zhitnitsky (DFSZ) [55, 56] and the Kim-Shifman-Vainshtein-Zhakharov (KSVZ) [57, 58] models.

The DFSZ model is identical to Peccei and Quinn's original model, except for the inclusion of a new complex scalar field, ϕ. This scalar couples to Standard Model particles via its interaction with the two Higgs doublets predicted by the Peccei-Quinn model. The vacuum expectation value for ϕ is much higher than the electroweak scale: $f_a = \langle\phi\rangle \gg v_F$.

The KSVZ model only considers the Standard Model Higgs doublet, although a new scalar field, σ, and a new heavy quark, Q, are introduced. As only the latter can couple to the known quarks, it mediates the interaction between the new field and the Standard Model (c.f. Fig. 2.1). The mass of the heavy quark is $M_Q \sim f_a$, while the vacuum expectation value of σ is $f_a = \langle\sigma\rangle \gg v_F$. The resulting axion, a, can be interpreted as the phase of σ.

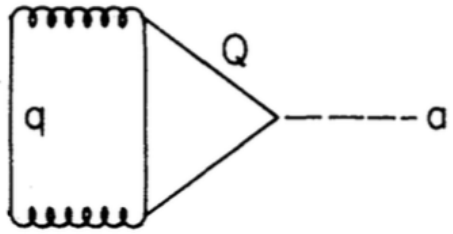

Figure 2.1 *Diagram for axion coupling to a Standard Model quark, q, via the new KSVZ quark, Q, and the gluon loops [57].*

Axions are expected to weakly couple to Standard Model particles, and the strength of the interaction depends on the choice of the theoretical model. Theories predict axion-photon, axion-electron, and axion-nucleon coupling.

The interaction between axions and photons can be written as [59]:

$$L_{a\gamma\gamma} = \frac{1}{4}\, g_{a\gamma\gamma}\, F_{\mu\nu}\widetilde{F}^{\mu\nu}\, a = -g_{a\gamma\gamma}\, \mathbf{E}\cdot\mathbf{B}\, a, \tag{2.6}$$

where a is the axion field, F is the electromagnetic field-strength tensor, $\widetilde{F}$ is its dual, and $\mathbf{E}$ and $\mathbf{B}$ are, respectively, the electric and magnetic fields. The coupling constant, $g_{a\gamma\gamma}$, is inversely proportional to f_a:

$$g_{a\gamma\gamma} = \frac{\alpha}{2\pi f_a}\left(\frac{E}{N} - \frac{2}{3}\frac{4+z}{1+z}\right). \tag{2.7}$$

The other factors entering this equation are the electromagnetic and colour anomaly of the axial current of the axion field, E and N respectively, and the quark mass ratio, z, defined in Eq. 2.5. Although the E/N ratio is unknown, theoretical models make predictions on its value. For example, according to the DFSZ description, $E/N = 8/3$, while in the KSVZ model the equality reads $E/N = 0$ [59]. This model dependence implies that, given an energy scale, a broad range of $g_{a\gamma\gamma}$ values is possible.

As for the interaction between axions and electrons, the role played by the model is even more important. While in the KSVZ model axions couple to electrons only at loop level, the DFSZ model predicts an axion-electron coupling at tree level. This makes quite an important difference in the production of axions in the Sun, as will be discussed later. The axion-electron coupling constant reads [60]:

$$g_{ae} = X_e\frac{m_e}{f_a} \;+\; \frac{3\alpha^2}{4\pi}\frac{m_e}{f_a}\left(\frac{E}{N}\log\frac{f_a}{m_e} - \frac{2}{3}\frac{4+z}{1+z}\log\frac{\Lambda}{m_e}\right). \tag{2.8}$$

The first term is model dependent and proportional to an $O(1)$ coefficient, X_e. The second term is model independent and induced at one loop via the photon coupling. Λ is an energy scale close to the QCD confinement scale, while all the other parameters have the same meaning as in Eq. 2.7.

The third possibility for axion interactions is to couple with nucleons. We

can write the Lagrangian as [61]:

$$\mathcal{L}(x) = i g_{aNN}\ \overline{\psi_N}(x)\ \gamma_5\ \psi_N(x)\ a(x), \tag{2.9}$$

where g_{aNN} is the coupling constant, $\psi_N(x)$ is either a proton or a neutron, and $a(x)$ is the axion field.

The couplings of QCD axions to ordinary matter give rise to a number of effects that can be searched for in astrophysics, cosmology, and laboratory experiments. The results of such searches can then be used to constrain the strength of the coupling constants. Moreover, while still providing a solution to the strong CP violation problem, invisible axions are also proposed as potential candidates for dark matter. All this will be discussed in the last section of this chapter.

2.2.2 Axion-like particles

The Peccei-Quinn model and the invisible axion models are only some examples of theories that extend the Standard Model of particle physics by introducing new symmetries. There are plenty of these theories, and if any of the symmetries is global and gets spontaneously broken, then a Goldstone or pseudo-Goldstone boson is obtained. If this boson is a light scalar (or pseudo-scalar), it can share qualitative properties with the QCD axion. This means that, in addition to invisible QCD axions, there can be many other axion-like particles (ALPs). ALPs are usually predicted by string theory-driven models [62–65].

Axion-like particles couple to ordinary matter in the same way axions do. For a generic ALP, we expect coupling constants to photons and electrons similar to the ones in Eq. 2.7 and 2.8, respectively. To adapt those equations to ALPs, one would remove the terms containing z, as they come from the mixing between axions and mesons, and replace f_a with the ALP decay constant [60].

Another difference is that, while axions had originally been proposed with the aim of solving a problem of QCD, ALPs can be considered as pure predictions of theories beyond the Standard Model. They are not needed for any specific purpose, but can be considered potential candidates for particle dark matter.

2.2.3 Axion cold dark matter

The QCD axion, and more generally the ALPs, have the main characteristics to be dark matter candidates. They are nearly collision-less, neutral, non-baryonic, and weakly interacting with the Standard Model particles. They might well constitute populations of cold dark matter, non-thermally produced through the misalignment mechanism in the early universe [65].

The misalignment mechanism assumes that fields in the early universe have a random initial state which is fixed by the expansion of the universe. The timescale for evolution of a field of mass m is $t \sim 1/m$, thus once this time elapses, the field starts oscillating around the minimum of its potential. Moreover, because of the expansion of the universe, its energy density scales as $\rho \propto 1/a^3$, where a is the universe scale factor defined in Eq. 1.5. Such a behaviour can be attributed to a cold dark matter fluid [66].

Axions and ALPs could have been copiously produced in the early universe via misalignment. We can express the cosmological energy density of the resulting axion population by using Eq. 1.8. The expectation for cold dark matter made of QCD axions is [65, 67]:

$$\frac{\Omega_a \ h^2}{0.112} \approx 6.3 \times \left(\frac{f_a}{10^{12}\ GeV}\right)^{7/6} \left(\frac{\Theta_a}{\pi}\right)^2, \tag{2.10}$$

where Θ_a is the initial misalignment angle, while for the ith ALP dark matter we would expect [65, 66]:

$$\frac{\Omega_{a_i} \ h^2}{0.112} \approx 1.4 \times \left(\frac{m_i}{eV}\right)^{1/2} \left(\frac{f_{a_i}}{10^{11}\ GeV}\right)^2 \left(\frac{\Theta_i}{\pi}\right)^2, \tag{2.11}$$

where the extra factor depends on the ith ALP mass, m_i.

The interest of the international scientific community in axion dark matter is growing fast. There are several experimental approaches to axion searches – searches that will be described both in the rest of this chapter and in Chapter 5.

2.3 Bounds on axion couplings

Axions and ALPs can be searched for in astrophysics, cosmology, and laboratory experiments, based on the theoretical predictions discussed in the previous section. The interaction between axions and ordinary matter can be exploited, and bounds on the axion couplings can be obtained as a result of both observations and simulations.

2.3.1 Astrophysical axion bounds

Looking at astrophysical objects to investigate particle physics might seem quite unusual. Nuclear reactions and thermal processes happening within the stars are well known for producing weakly interacting particles, the most obvious example of which is the production of neutrinos in stars (e.g. leading to the solar neutrino experiments, including those performed at the Davis cavern of the Homestake mine, where the experimental work reported in this thesis was conducted). In principle, particles other than neutrinos could also be being produced. The emission of such particles causes an energy loss in the source, whose properties might change. The study of stellar energy loss then leads to constraints on some of the properties of the particles that are generated and emitted [59]. The Sun, for example, can be considered a powerful source of axions, via both axion-photon and axion-electron coupling.

According to the KSVZ model, the main axion production mechanism happening in the interior of the Sun is driven by the axion-photon coupling. Such a process, known as the Primakoff effect, results in the production of axions from thermal photons within the electromagnetic fields of the stellar environment [68]. The corresponding Feynman diagram is shown in the top left panel of Fig. 2.2. The energy loss rate per unit volume quadratically depends on the coupling constant [59]:

$$Q = \frac{g_{a\gamma\gamma}^2 T^7}{4\pi} F, \tag{2.12}$$

where T is the solar temperature, and F is a numerical factor of $O(1)$. The

resulting axion flux reaching the Earth is:

$$\frac{d\Phi_a}{dE} \approx \left(\frac{g_{a\gamma\gamma}}{10^{-10} GeV^{-1}}\right)^2 \; 6.0 \times 10^{10} cm^{-2} s^{-1} keV^{-1} \; E^{2.481} \; e^{-E/1.205}, \qquad (2.13)$$

where the coupling constant, $g_{a\gamma\gamma}$, is in GeV^{-1}, and the energy, E, is in keV. Equation 2.13 can be used to estimate the axion luminosity in terms of solar luminosity:

$$L_a = \left(\frac{g_{a\gamma\gamma}}{10^{-10} GeV^{-1}}\right)^2 \; 1.85 \times 10^{-3} \; L_\odot. \qquad (2.14)$$

According to the standard solar model, the Sun is approximately halfway through its hydrogen-burning phase so that the solar axion luminosity should not exceed $L_\odot$. This leads to a constraint on the axion flux, and thus on the axion-photon coupling: $g_{a\gamma\gamma} \lesssim 1 \times 10^{-9}$ GeV^{-1} [59].

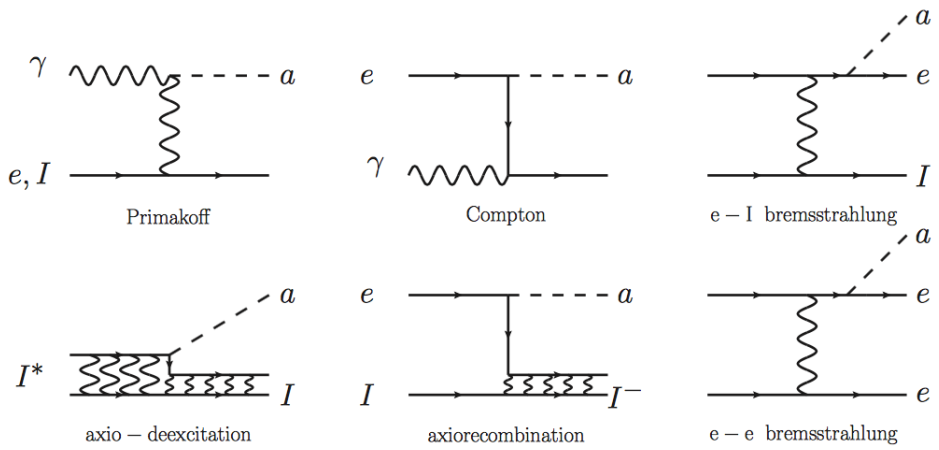

Figure 2.2 *Sample of Feynman diagrams of the reactions responsible for the solar axion flux. Both axion-photon and axion-electron coupling-driven processes are included [60].*

We have already mentioned that the Sun also emits neutrinos. Energy loss due to axion production is expected to increase the solar neutrino flux, as the necessary enhancement of nuclear burning would induce higher temperatures in the Sun. Gondolo and Raffelt used the all-flavour solar neutrino flux measured by the Sudbury Neutrino Observatory (SNO) to constrain the axion-photon coupling to be $g_{a\gamma\gamma} \lesssim 7 \times 10^{-10}$ GeV^{-1} [69].

Stellar evolution can also be tracked through globular-cluster stars, gravitationally bound systems of stars being formed at the same time. The resulting limit on the axion-photon coupling is $g_{a\gamma\gamma} \lesssim 1 \times 10^{-10}$ GeV^{-1} [59].

Astrophysical predictions on the interaction between axions and photons can be investigated experimentally with a suitable setup. Indeed, using a strong magnetic field that mimics the solar electromagnetic field, solar axions approaching the Earth can be converted to photons, and detected. This is the working principle of helioscopes, such as the CERN Axion Solar Telescope (CAST), whose most recent result, discussed in detail in Chapter 5, is reaching the scale of axion bounds set by astrophysical observations [70].

If a DFSZ axion is considered, then Primakoff production is suppressed and the dominant stellar emission process is driven by the axion-electron coupling, g_{ae}. Contributions to the overall flux come from atomic axio-recombination and axio-deexcitation, axio-bremsstrahlung, and Compton scattering (c.f. Fig. 2.2).

Analysis of the impact of axion emission on the cooling of white dwarfs results in best fit values in the range $g_{ae} \sim (3-7) \times 10^{-13}$ [71], while the most stringent bound on the axion-electron coupling is placed by the axion-induced energy loss in red giants: $g_{ae} \lesssim 2.5 \times 10^{-13}$ [72]. Experimental searches undertaken to measure the axion-electron coupling will be described in Chapter 5.

Astrophysical objects can also be employed to set limits on the third possible coupling, the one driving the interaction between axions and nucleons. Supernovae and neutron stars, for example, can emit axions by nucleon bremsstrahlung, $N + N \rightarrow N + N + a$, a reaction that depends on the coupling g_{aNN} [59]. Possible axion emission during the explosion of the Supernova 1987A has been considered. The increase in density during the final collapse of the star would prevent neutrino propagation, while still making possible the escape of axions from the interior, via nucleon bremsstrahlung. The resulting limit on the axion energy scale is $f_a \geqslant (0.7-5) \times 10^{10}$ GeV [73]. In another approach, simulations have been done to explore how the emission of axions by weakly magnetized neutron stars during evolution alters their observable surface temperatures. The resulting bound is $f_a \geqslant (5-10) \times 10^7$ GeV [74].

Anomalous over-cooling effects have been observed in several stellar systems. Such effects have been interpreted as a motivation for axion-like particles, and their consequent hints for ALP-photon and ALP-nucleon coupling could be significant [75].

2.3.2 Cosmological axion bounds

According to the astrophysical axion bounds, the spontaneous breaking of the Peccei-Quinn symmetry is expected to happen at a very high energy scale. As a consequence of this, axions start playing quite a relevant role in cosmology. Axion cosmological effects depend on the value of the Peccei-Quinn symmetry breaking scale, f_a – a value that can also be related to the potential dark matter nature of axions.

In the previous section, we discussed the conditions for axions to be cold dark matter candidates. This happens if axions are non-thermally produced via the misalignment mechanism. The resulting cosmological energy density is expressed, as a function of f_a, in Eq. 2.10. In order to obtain the energy densities observed in the universe, if a cold dark matter axion population exists, then the energy scale has to be $f_a \sim 10^{12}$ GeV.

The other possibility is to have hot dark matter axions, thermally produced in the early universe via axion-pion conversion ($\pi + \pi \longleftrightarrow \pi + a$). Massive thermal axions would have a similar impact on cosmological observables as massive neutrinos (c.f. Chapter 1). The cosmological bound on the breaking energy scale in this case is $f_a \lesssim 10^{12}$ GeV [67], while the most stringent limit on the thermal axion mass has been placed using Planck 2015 data, and is $m_a < 0.529$ eV [76].

The astrophysical and cosmological bounds on axion couplings narrow the parameter space where axions could still exist. Moreover, these bounds drive the experimental searches aiming at axion detection.

2.3.3 Laboratory axion bounds

We have mentioned that bounds on axion mass came from laboratory experiments at the very early stage of axion history. When Weinberg and Wilczek proposed a 100 keV – 1 MeV mass axion as a Peccei-Quinn boson, such a candidate was soon ruled out, as an axion with mass of this order would have had large enough couplings to be observed in several laboratory experiments [54]. This is the start of the invisible axions era.

Since then, there have been other axion searches in laboratory-based experiments. They are mainly magnetometry searches for spin-dependent forces

mediated by axion exchange. The results were generally weaker than the bounds set by both astrophysical and cosmological studies.

Another approach to axion-like particle detection is a microwave light shining through the wall experiment, that exploits the Primakoff effect twice. A photon source is fired against a wall, and some of the photons are converted to axion-like particles by the Primakoff effect. The wall blocks the unconverted photons but not the ALPs, that reach a receiving cavity where the reciprocal conversion takes place via the Primakoff effect. The photons thus obtained can be detected [77].

Very recently, Abel *et al.* published an interesting search for ultra low-mass axion dark matter, based on the proposed interaction between an oscillating axion dark matter field and gluons or fermions. Assuming that such an interaction would induce oscillating electric dipole moments of nucleons and atoms, they set the first laboratory bound on the axion-gluon coupling, and also improved on previous laboratory constraints on the axion-nucleon interaction [78].

In Chapter 3 and 5, we will provide more information about other experimental approaches that can be used to attempt a detection of axions and axion-like particles. The interest of the scientific community in this kind of searches is growing fast, and a discovery would have a strong impact on particle physics, and beyond.

Chapter 3

The Large Underground Xenon experiment

Dark matter candidates and beyond-Standard Model particles have been searched for with great enthusiasm over the past decades. This chapter focuses on how technologies have been adapted to the hunt for new particles, expected to interact only weakly with ordinary matter, making their observation quite challenging.

An overview on potential detection strategies opens the chapter, that then focuses on direct detection, the ultimate approach to dark matter discovery. The working principle of time projection chambers is explained in detail, giving a few examples of their use, and describing the characteristics of xenon in particular, as this is the target used in the present work.

The main character of the chapter, the Large Underground Xenon (LUX) experiment, is described in its components and operations. Details about background sources, data taking and selection, and calibration strategies in LUX close the chapter.

3.1 Dark Matter detectors

To maximise the chance of detection, various strategies have been employed in searching for dark matter. There are three main channels we can look at in the hunt for potential candidates, as highlighted in Fig. 3.1, where P and χ represent,

respectively, a particle of ordinary and dark matter.

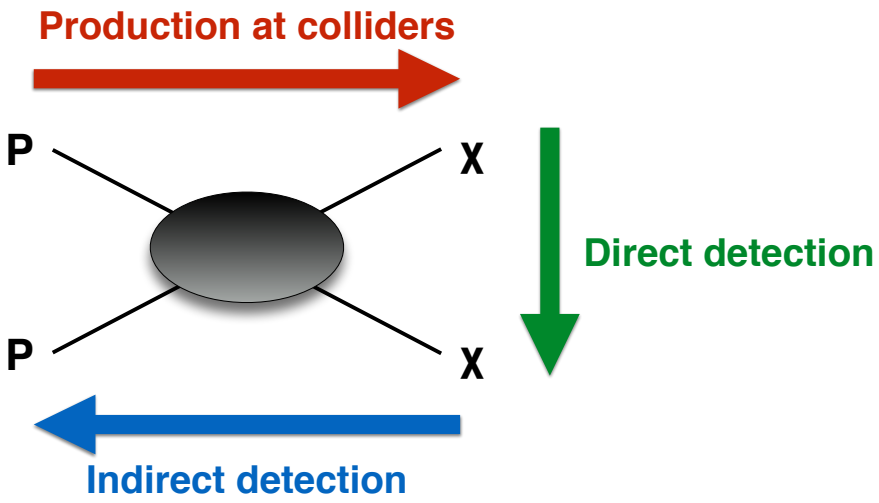

Figure 3.1 *Schematic view of the possible channels for dark matter detection: production at colliders (red arrow, left to right), direct (green arrow, top to bottom) and indirect (blue arrow, right to left) detection.*

3.1.1 Production at colliders

Reading the diagram in Fig. 3.1 from left to right along the red arrow, the collision of electrons or protons at colliders could produce pairs of dark matter particles, if the kinetic energy is sufficient to allow pair production. In detectors such as ATLAS and CMS, both operating at the Large Hadron Collider (LHC), reactions such as $pp \rightarrow \chi\overline{\chi} + jets$ are searched for. The experimental strategy consists in using the jets as a trigger, and the missing transverse momentum as typical dark matter signature.

Considering the high rate of data collected at the LHC, this sort of analysis is not easy, and is affected by quite dominant backgrounds. In particular, processes such as $pp(p\overline{p}) \rightarrow \nu\overline{\nu} + jets$ and $pp(p\overline{p}) \rightarrow l^{-}\overline{\nu}(l^{+}\nu) + jets$ induce a missing energy deposit, that could mimic a signature from WIMPs.

No evidence for dark matter production has been observed at the LHC yet, in any of the several channels both ATLAS [79] and CMS [80] have been looking at.

Analysis strategies are constantly improved and the quantity of collected data is increasing, thus dark matter production could be just around the corner.

3.1.2 Indirect detection

Following the blue arrow on Fig. 3.1, from right to left, dark matter particles are expected to annihilate with each other, with the annihilation producing any particle of ordinary matter, as far as kinematically allowed. The indirect detection relies on the search for the products of such an annihilation (or their own decay products), such as γ rays, positrons, or neutrinos. To maximise the chances of discovery, experiments have been looking at favoured sources, such as the galactic centre, the galactic halo and galaxy clusters, where a high density of dark matter is expected. Depending on the ordinary particle produced, the detection principle must be appropriate, thus both space-based and ground-based detectors have been employed. For example, while charged particles are deflected by galactic magnetic fields, neutral particles travel in a straight line; while γ rays can be absorbed in the interstellar medium, neutrinos are not.

Experiments such as the Fermi Large Area Telescope (Fermi-LAT) [81] search for dark matter annihilating into photons in space, by detecting low-energy γ rays, while atmospheric Cherenkov telescopes such as MAGIC [82] can point to the interesting stellar object to identify mono-energetic lines, or an anomalous flux of photons. No evidence for dark matter annihilation signal has been found to date, and upper limits on the annihilation cross sections have been set. In order to improve the sensitivity reach, the new trend in such searches seems to be the combination of data taken from more than one telescope. The first joint analysis of γ-ray data comes from the Fermi-LAT and MAGIC collaborations, and the resulting limits on the annihilation cross section for dark matter particle masses between 10 GeV and 100 TeV have been published [83].

Recent full-sky maps of the galaxy from the Fermi Gamma-Ray Space Telescope have revealed a diffuse component of γ-ray emission towards the galactic centre. Usually called "Fermi haze", this spectrum of emission has been modelled adding a magnetic field component (resulting in anisotropic diffusion) to dark matter annihilations in a prolate galactic dark halo. The Fermi haze extends up to roughly $\pm$ 50 degrees in latitude, and shows sharp edges at high latitudes. This feature is the most significant outstanding issue, as in contrast with what expected from dark matter annihilation [84].

Satellite experiments such as PAMELA and the Alpha Magnetic Spectrometer (AMS) on the International Space Station can detect positrons, potentially produced by dark matter annihilation. Both PAMELA [85] and AMS [86] data reveal an increase in positron fraction in the energy range 10 – 250 GeV. However, such a rise could be due not only to dark matter annihilation, but also to pulsars (rapidly rotating neutron stars) and microquasars (accretion disk around a black hole), thus this cannot be considered as a clear evidence of dark matter.

Neutrino detectors can behave as indirect detection devices to identify neutrino signatures due to dark matter annihilation. For example, ground-based detectors such as IceCube and ANTARES [87] search for annihilating dark matter in the Sun, expected to produce GeV neutrinos. IceCube delivered the most stringent limit to date on the spin-dependent dark matter-proton scattering cross section for WIMP masses above 50 GeV, annihilating exclusively into $\tau^+\tau^-$ particles (c.f. Figures 4.6, 4.7) [88]. The limit on the spin-independent cross section is not competitive with respect to direct detection results. On the other hand, neutrino observation experiments are able to place strong limits on spin-dependent cross section, as they are measuring the annihilation products, not relying on the expectation values of the proton and neutron spin operators in the target nucleus, as direct detection does. It is important to notice that limits placed by neutrino experiments are more model dependent than direct detection results, as strongly relying on assumptions for the dark matter annihilation process.

Beside annihilation, indirect detection also involves searches for the decay of dark matter. An interesting example of this is given by the x-ray satellites, such as XMM-Newton, able to search for signals between a few keV and $\sim$ 10 keV. In 2014 an unidentified x-ray line at about 3.5 keV was observed in x-ray spectra of the Andromeda galaxy and the Perseus galaxy cluster, by the XMM-Newton telescope. Two independent groups reported the same result [89, 90], declaring that the feature was consistent with a dark matter decay line. Nevertheless, the feature might also be otherwise explained, so further confirmations are still needed to assure its nature. This was the aim of high-resolution x-ray spectroscopy with Hitomi, expected to resolve the origin of the 3.5 keV line. However, Hitomi observation of the Perseus cluster did not even show the expected feature. For a broad dark matter line, there is a 99% inconsistency between Hitomi data and XMM-Newton observation [91]. Considering the focus of this thesis, it is worth mentioning that one of the interpretations of the 3.5 keV line is a 7 keV axion

dark matter particle decaying into photons [92].

3.1.3 Direct detection

Going back to Fig. 3.1, the green arrow towards the bottom of the diagram represents the direct detection. It relies on the interaction between a dark matter particle, χ, and a target nucleus, N, and aims at detecting the recoil energy of the latter, E_n.

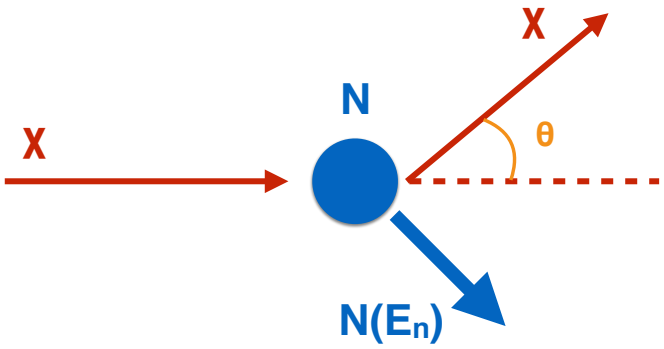

Figure 3.2 *The elastic interaction between a dark matter particle, χ, and a target nucleus, N. Direct detection aims at detecting the recoil energy of the nucleus, E_n.*

The kinematics of the dark matter-nucleus elastic scattering can be easily computed, as dark matter particles move in the halo at non-relativistic speeds. If a dark matter particle of mass M_χ and velocity v scatters off a nucleus of mass M_N, the recoil energy of the nucleus is:

$$E_n = \frac{v^2\mu^2}{M_N}(1 + cos\theta), \tag{3.1}$$

where $\mu \equiv M_\chi M_N/(M_\chi + M_N)$ is the dark matter-nucleus reduced mass, and θ is the scattering angle defined in Fig. 3.2.

The experimental energy threshold is the smallest recoil energy accessible by

a detector. The lower is such a threshold, the larger is the phase space to probe.

Technologies to perform direct detection of dark matter vary. Figure 3.3 reports a non-exhaustive overview, just to give an idea of the great interest and effort deployed in this field – a field that is still believed the ultimate channel for dark matter discovery.

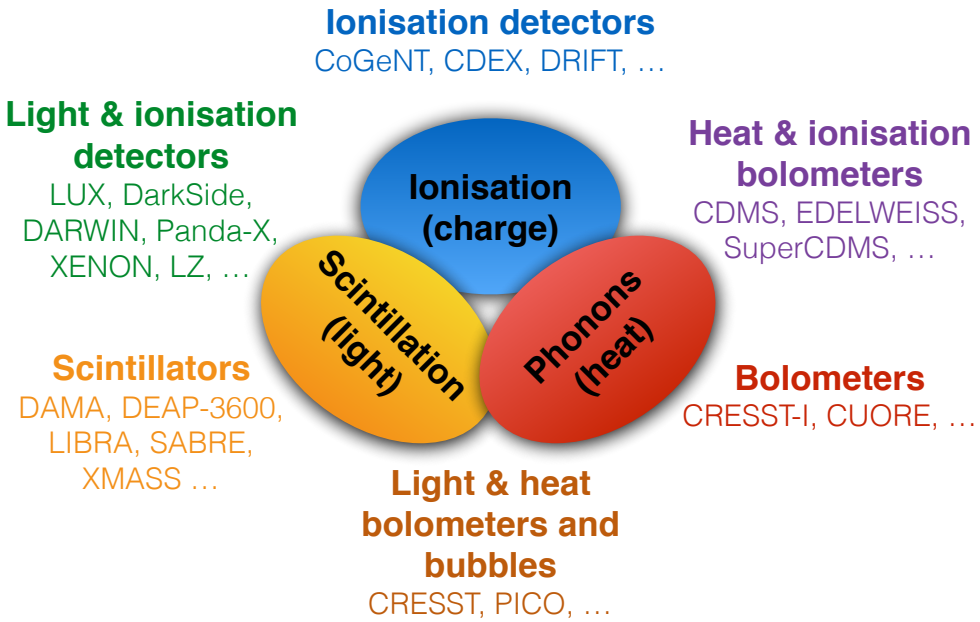

Figure 3.3 *Overview of the technologies employed in direct dark matter detection. Ionisation (charge collection) as the blue blob, scintillation (light collection) as the orange blob, phonons (heat change) as the red blob. A non-exhaustive list of experiments for each model of detection is also given, to show which channel, or which combination of the available channels, has been chosen.*

Looking at Fig. 3.3, there are three possible approaches to direct detection. When a collision between a dark matter particle and a target nucleus occurs, we can measure ionisation via charge collection, scintillation via light collection, and phonons via heat change. Ionisation happens when the recoil energy is enough for an electron of the target nucleus to be released in the collision, leaving the atom as a charged ion. When the energy of the collision is enough that the electrons increase in energy level and release a photon when relaxing down to a lower level, this prompt release of light is called scintillation. If the excitation of the target due to the collision creates a detectable change in temperature or acoustic level in a bubble chamber or a crystal, then phonons can be measured.

The choice of the experimental strategy follows the decision of which of those techniques to employ. The ideal approach would be using all three channels, but this makes the detector design complex. For this reason, experiments have been designed to use only one channel (single phase), or a combination of two of them (double phase). Either germanium detectors or low-pressure gas chambers can measure ionisation signals; scintillation light can be detected in crystals or noble-gas liquids; finally, phonons can be collected in cryogenic bolometers.

Starting with the single phase experiments, an example of ionisation detector is the CoGeNT dark matter experiment [93]. Located at the Soudan Underground Laboratory in Minnesota, it searches for ionisation signals from dark matter interactions in a single high-purity germanium crystal. The main features of such a device are the very low energy threshold ($\sim$ 0.5 keV), that allows for searches for low-mass (> 5 GeV/c^2) WIMPs, a low level of background, and the possibility to discriminate between signal and background [1] by using the signal rise time, that differs between electron recoil and nuclear recoil.

A second purely ionisation detector strategy is embodied in the Directional Recoil Identification From Tracks (DRIFT) detector [94]. Located 1100 m underground in the Boulby Underground Laboratory at the Boulby Mine (UK), DRIFT employs a low-pressure gas as target material to perform directional searches for WIMPs. Although the ionisation density from γ rays and β particles is too low to produce a signal, DRIFT can discriminate against α particles because the tracks are much longer than expected for WIMPs.

Scintillation detectors use scintillating crystals or liquid scintillators as the target medium. The DArk MAtter (DAMA) experiment, for example, employs highly radiopure crystals, made of thallium-doped sodium iodide (NaI(Tl)) and coupled to photomultiplier tubes (PMT). DAMA is located at the Gran Sasso National Laboratory in Italy and aims at detecting WIMP signal through its annual modulation due to the revolution of the Earth around the Sun. If dark matter wind exists and travels in a certain direction, then the signal rate will be modulated over the year, presenting a maximum and a minimum in correspondence with the approximate dates of the alignment or anti-alignment of the Earth's velocity with the WIMP wind. The first and second generation detectors, respectively DAMA/NaI and DAMA/LIBRA, observed an annual

[1] In experimental physics, events generated by known phenomena and expected to be recorded in the detector are called "background", as opposed to "signal" events, usually expected from still-to-discover interactions.

modulation signal, claiming a discovery at 8.9 σ [95, 96]. However, all the experiments coming afterwards could not detect a similar effect, and actually excluded the region of phase space where the DAMA claim stands (c.f. Fig. 4.6).

Liquid scintillators are used by experiments such as XMASS [97] and DEAP-3600 [98], employing, respectively, liquid xenon and liquid argon as target material. Scintillation in liquid noble gases is characterised by a different pulse shape for nuclear recoil and electron recoil events, enabling discrimination between signal and background. We will come back to the differences between xenon and argon as target materials. For now, we only point out that argon detectors are characterised by an intrinsic background, due to ^{39}Ar, that has to be removed by isotopic purification.

Cryogenic bolometers collect the phonon signal produced in the crystals as a consequence of any interaction. As an example, the Cryogenic Underground Observatory for Rare Events (CUORE) [99], located in the Gran Sasso National Laboratory, uses low-heat capacity tellurium dioxide (TeO_2) crystals as target. The detector operates in cryogenic regime, at a temperature of 10 mK, in order to reduce thermal noise. The employment of radiopure materials ensures low radioactive background level. The working principle of such a device relies on the detection of temperature rise in the crystals by the change in resistance in the germanium thermistors glued to the crystals.

Double phase experiments employ two of the three possible channels presented in Fig. 3.3. The Cryogenic Dark Matter Search (CDMS) in the Soudan Underground Laboratory, for example, takes advantage of both ionisation and phonons, using Ge and Si detectors [100]. These operate at low temperature (40 mK) to reduce thermal noise and ensure a heat capacity low enough to gain a large temperature signal. An electric field drifts ionisation electrons to the top of the crystals, while the phonon signal is collected by superconducting transition edge sensors coupled with SQUIDs. Being the ionisation yield of nuclear recoils lower than for electron recoils, the ratio of the ionisation and heat signals works as discrimination parameter. The SuperCDMS experiment is the successor to CDMS (c.f. Fig. 4.6 for results from CDMS). As the event rate from cosmogenics at the depth of Soudan was proving to be a limiting factor, a deeper site was needed. SuperCDMS will thus be located at SNOLAB in Canada [101].

The Cryogenic Rare Event Search with Superconducting Thermometers (CRESST) is located in the Gran Sasso National Laboratory, and targets light

WIMPs with ultra-low threshold detectors [102]. These are calcium tungstate (CaWO4) crystals, cooled down to 10 mK. An interaction mainly produces heat as phonons, but scintillation light is also emitted. Phonons are detected through transition edge sensors, while photons are collected by a silicon light absorber, that converts them to heat, eventually detected by secondary thermometers. As in these crystals a nuclear recoil produces 10 – 40 times less scintillation light than an electron recoil does, the fraction of the phonon and scintillation signal is chosen as discrimination parameter.

The PICO collaboration has worked at the SNOLAB underground facility, in Canada, since 2013, to search for dark matter with superheated liquids (c.f. Figures 4.6, 4.7). The PICO-60 detector is currently the largest bubble chamber in operation. It was initially filled up with CF_3I, substituted by C_3F_8 in 2016 to increase sensitivity to spin-dependent WIMP interactions [103]. The superheated detector technology provides rejection of γ and β background events, and excellent α particles rejection, thanks to the acoustic emission of bubble formation. The new proposal of the PICO project is a much larger bubble chamber, called PICO-500.

Referring to Fig. 3.3, the last class of detectors relies on both charge and light collection. These detectors are called dual-phase time projection chambers and will be fully described in the next section.

3.2 Dual-phase xenon time projection chambers

3.2.1 Working principle of TPCs

A dual-phase time projection chamber (TPC) uses noble scintillators (typically xenon or argon), in both liquid and gaseous phase, as target medium [104]. These chambers are usually cylinders, with a liquid volume and a gaseous region on top, seen by two arrays of photomultiplier tubes (PMTs) at the top and at the bottom, as pictured in Fig. 3.4. The interaction of a particle within the detector produces a prompt scintillation signal, called $S1$. Electrons are also liberated, because of ionisation processes, and those escaping recombination at the event site are drifted towards the gaseous region at the top of the chamber by an applied electric field. A secondary electroluminescence signal, called $S2$ and proportional to the prompt $S1$, is produced. Both signals are read by the PMT arrays and measured in units

of detected photons (phd); the location of the event in the horizontal plane will be given by the map of the fired PMTs in the top array, while the depth of it is obtained from the drift time between $S1$ and $S2$.

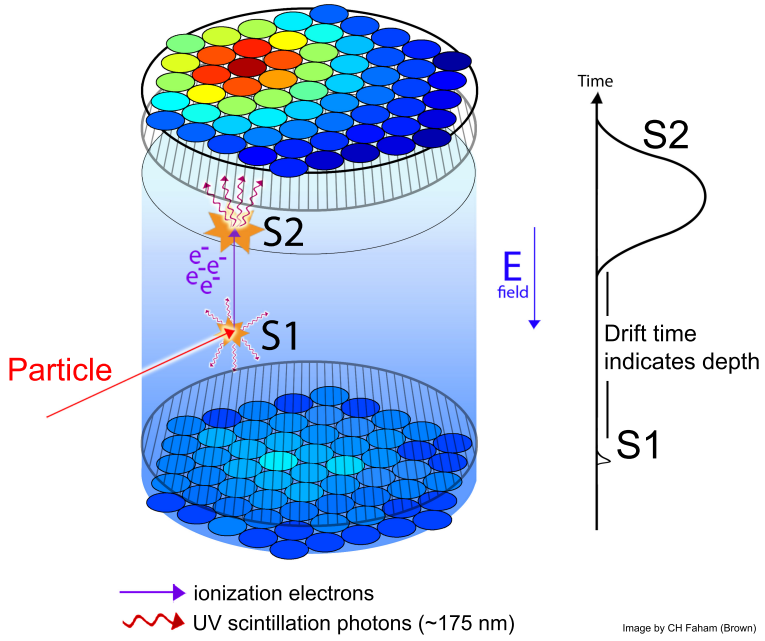

Figure 3.4 *Sketch of a typical TPC event [105]. The particle interaction produces primary scintillation light ($S1$), and ionisation electrons, that are drifted towards the top of the detector by an electric field. Such electrons create an electroluminescence signal ($S2$) when entering the gas region above the liquid phase. Both signals are measured in units of detected photons (phd) and detected by two arrays of PMTs, one at the top and the other at the bottom of the chamber.*

Different particles induce different $S2/S1$ ratios, enabling excellent particle discrimination that separates electron recoils from nuclear recoils, as will be discussed later in this chapter. Additionally, the three-dimensional positioning of the event ensures the removal of background events with spatial distributions coming from the surface or the edges of the chamber. TPCs are large-scale detectors, and this contributes to their high sensitivity for dark matter, and rare event searches more broadly.

3.2.2 Experiments employing dual-phase TPCs

In the past decades, dual-phase TPCs have largely led direct dark matter detection, because they allow for very large active volumes, and high signal-to-background discrimination power. The noble elements usually employed to build such devices are argon and xenon. The former is the most abundant noble element available and the cheapest one, the latter is the most massive stable noble gas and has interesting properties in case of γ rays detection.

An example argon TPC is the DarkSide experiment, located at the Gran Sasso National Laboratory in Italy. The DarkSide collaboration published results on the WIMP search with the DarkSide-50 detector (c.f. Figures 4.4, 4.5) [106], and the data taking will continue, while building a series of larger argon TPCs. In the previous section we have mentioned that the intrinsic background due to ^{39}Ar characterises argon detectors. One of the most innovative techniques implemented by DarkSide is the use of argon from underground gas wells rather than atmospheric sources – an approach that significantly lowers the radioactive ^{39}Ar background.

Beside argon, xenon is the other most used target material for TPCs. Both noble gases are characterised by a property known as "self shielding". It means that the attenuation length is quite short relative to the detector scale, so that external backgrounds cannot reach the sensitive volume. The difference between xenon and argon is that the γ ray attenuation lengths are greater for the latter, making xenon more effective. The reason stands in the xenon's large atomic number ($Z = 54$) and its high density ($\rho \sim 3$ g/cm^3) [107]. The first dual-phase xenon TPC was a 31 kg detector, called ZEPLIN-II and having operated at the Boulby Underground Laboratory (UK) between 2006 and 2011 [108]. Other examples of xenon TPCs are the XENON Dark Matter project, the PandaX detector, the LUX experiment and its successor LZ.

The XENON100 experiment [109], coming after its prototype XENON10 (c.f. Fig. 4.6), operated at the Gran Sasso Underground Laboratory from 2009 to 2016, delivering important results on WIMP and other rare event searches (c.f. Figures 4.4, 4.5, 4.6, 4.7, 5.17, 5.19) [110–112]. The active target of XENON100 contains 62 kg of liquid xenon, while other 99 kg of the same material are used to fill an external veto system. Both the internal volume and the veto are read by photomultiplier tubes. The upgrade of XENON100 is XENON1T,

a $\sim$ 2000 kg target and $\sim$ 1000 kg fiducial mass xenon TPC [113]. XENON1T is the first ton-scale detector of this kind, operating in the same location as its predecessor, from 2016. The first data taking period was interrupted by an earthquake after about 34 live days, and the collaboration reported the first dark matter search result [114]. XENON1T is still taking data.

Another dual-phase xenon TPC is the half-ton scale detector installed at the China Jin-Ping underground Laboratory, PandaX-II, operating since 2014. The first run started in 2015 and was stopped because of the high level of krypton background. A krypton distillation campaign followed, and operations were recovered in 2016, leading to a 80-live days data set. Results on both spin-independent and spin-dependent WIMP cross section have been published (c.f. Figures 4.5, 4.7) [115, 116], while PandaX-II is still taking data. The most recent result has been presented in the summer 2017 at the TeV Particle Astrophysics 2017 Conference at Columbus in the United States, but a publication still has to come.

The LZ detector will be described in Chapter 5, while the next section is dedicated to the LUX experiment. Both of them are dual-phase TPCs filled up with xenon, thus before moving on, we give a few more details about xenon as a target medium.

3.2.3 Xenon as a target medium

Xenon has been proven to be suitable for direct detection of dark matter, being one of the most promising scintillators among other noble elements. Xenon as a high atomic number and a high density (both leading to the already discussed property of "self shielding"); it has a high radioactive purity, it is not chemically dangerous and relatively easily procurable; it has a broad scintillation spectrum (a 14 nm window in the VUV region, showing a single peak at 178 nm) and high scintillation efficiency [117, 118].

A particle interaction in liquid xenon induces excitation and ionisation of the Xe atom [119]. The excited and ionised atoms take part to two distinct processes. The excited Xe^*, called exciton, reacts with the surrounding xenon atoms and produces an excited dimer, Xe_2^*, called excimer. The excimer then decays, emitting a detectable photon, $h\nu$ [118]:

$$\begin{aligned} Xe^* + Xe + Xe &\rightarrow Xe_2^* + Xe, \\ Xe_2^* &\rightarrow 2Xe + h\nu. \end{aligned} \tag{3.2}$$

The reaction of the ion Xe^+ with the surrounding xenon atoms produces a dimer ion, Xe_2^+, that undergoes recombination with ionization electrons. Such a recombination can only produce Xe^{**}, that are atoms in the excited levels placed below the minimum of the potential curve of the Xe_2^+ in its ground state [120]. A non-radiative transition follows, producing an exciton and some heat:

$$\begin{aligned} Xe^+ + Xe &\rightarrow Xe_2^+, \\ Xe_2^+ + e^- &\rightarrow Xe^{**} + Xe, \\ Xe^{**} &\rightarrow Xe^* + heat. \end{aligned} \tag{3.3}$$

The exciton undergoes the same reaction as in Eq. 3.2, with the excimer decaying and emitting a detectable photon, $h\nu$. Such light is what we have called prompt scintillation signal, $S1$. In a time projection chamber, the heat released in Eq. 3.3 cannot be collected and is lost.

If there is no electric field applied, ionisation electrons undergo recombination with the ion Xe^+ to create an exciton Xe^*, that follows the reaction in Eq. 3.2 contributing to the $S1$ signal. However, in the presence of an electric field, some of the electrons can be collected. Taken away from the interaction site, preventing electron-ion recombination, electrons are drifted towards the gaseous region at the top of the chamber. There, they produce a secondary electroluminescence signal, previously named $S2$.

At the beginning of this section we have mentioned that TPCs enable discrimination between nuclear and electron recoil events. Certainly related to the different signal yields of the two classes of events, such a distinction has been shown to be potentially linked to the initial Xe^*/Xe^+ production ratio in liquid xenon. This ratio is ~ 0.9 for nuclear recoils, and ~ 0.06 for electron recoils, causing much less ionisation charge in the case of nuclear recoils [121].

3.2.4 Signal yields and energy reconstruction in dual-phase xenon TPCs

Beside the initial production ratio of excitons and ions, nuclear recoils happening in liquid xenon have denser tracks than electron recoils, resulting in more recombination between ionisation electrons and Xe^+. Thus, the amount of $S2$ signal collected when a collision happen, is smaller for a nuclear recoil than an electron recoil, given the same recoil energy. The quantity of signal collected is indicated by the yield.

Indicating with $S1(\mathbf{E})$ the scintillation signal collected at a given electric field, $\mathbf{E}$, and $S1_0$ that collected at infinite field (when no recombination happens), the scintillation yield is defined as the $S1(\mathbf{E})/S1_0$ ratio. The ionisation yield is also defined as a ratio, $Q(\mathbf{E})/Q_0$, where $Q(\mathbf{E})$ and Q_0 are the charge collected if an $\mathbf{E}$ field is applied and in case of no recombination happening, respectively.

The relationship between the scintillation and ionisation yield in liquid xenon is shown in Fig. 3.5, taking α particles as an example. The dependence reads:

$$S1(\mathbf{E})/S1_0 = \frac{1 - Q(\mathbf{E})/Q_0 + N_{ex}/N_i}{1 + N_{ex}/N_i - \chi}, \tag{3.4}$$

where N_{ex} and N_i are, respectively, the number of excitons and electron-ion pairs produced by an ionising radiation, and $\chi = N_{i0}/N_i$ is the ratio between the number of escaping electrons at zero electric field and the number of electron-ion pairs. Calculations carried in Ref. [118] report values of $N_{ex}/N_i = 0.20$ and $\chi = 0.43$, for electron recoil interactions in liquid xenon.

The charge collected at infinite field, Q_0, is defined differently in the case of electron and nuclear interactions. For electron recoils, it is expressed in terms of recoil energy, E_e (measured in keV_{ee}), and average energy needed to produce an electron-ion pair, W, as in Eq. 3.5; while Eq. 3.6 shows that, for nuclear recoils, a correction factor, $\mathcal{L}$, has to be inserted, and the recoil energy for a nuclear event, E_n (measured in keV_{nr}), has to be considered [122]:

$$Q_0(ER) = \frac{E_e}{W}, \tag{3.5}$$

$$Q_0(NR) = \frac{E_n}{W} \cdot \mathcal{L}. \tag{3.6}$$

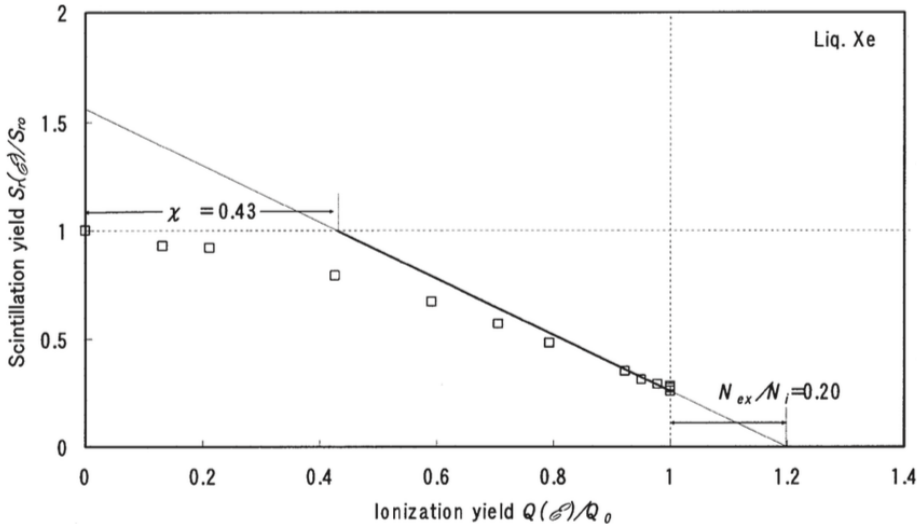

Figure 3.5 *Dependence of scintillation yield on ionisation yield, for α particles in liquid xenon. Note that the y axis label, $S_r(E)/S_{r0}$, has to be read as $S1(\boldsymbol{E})/S1_0$ in the text. According to Eq. 3.4, data points should lie on a straight line. The deviation seen can be attributed to either lack of amplifier linearity, or to drifting electrons attaching to impurities [118].*

The correction term applied to the nuclear recoil case, $\mathcal{L}$, is called the Lindhard factor [123]. It suppresses the charge yield of nuclear recoils, as visible in Fig. 3.6, to account for more energy being lost to atomic motion or heat with respect to electron recoils. The Lindhard factor can be written as a function of the reduced energy $\varepsilon = 11.5\ E_n\ Z^{-7/3}$ keV$_{nr}$ [124]:

$$\mathcal{L} = \frac{k \cdot g(\varepsilon)}{1 + k \cdot g(\varepsilon)}, \tag{3.7}$$

where for a nucleus with atomic and mass number, respectively, Z and A, $k = 0.133\ Z^{2/3}\ A^{-1/2}$, and $g(\varepsilon) = 3.0\ \varepsilon^{0.15} + 0.7\ \varepsilon^{0.6} + \varepsilon$.

The scintillation quenching factors are defined for electron and nuclear recoils as in Eq. 3.4, given the ratios in Eq. 3.5 and 3.6, and are called S_e and S_n, respectively. Figure 3.6 shows a few examples of the behaviour of these factors as a function of drift field, for both electron and nuclear recoils.

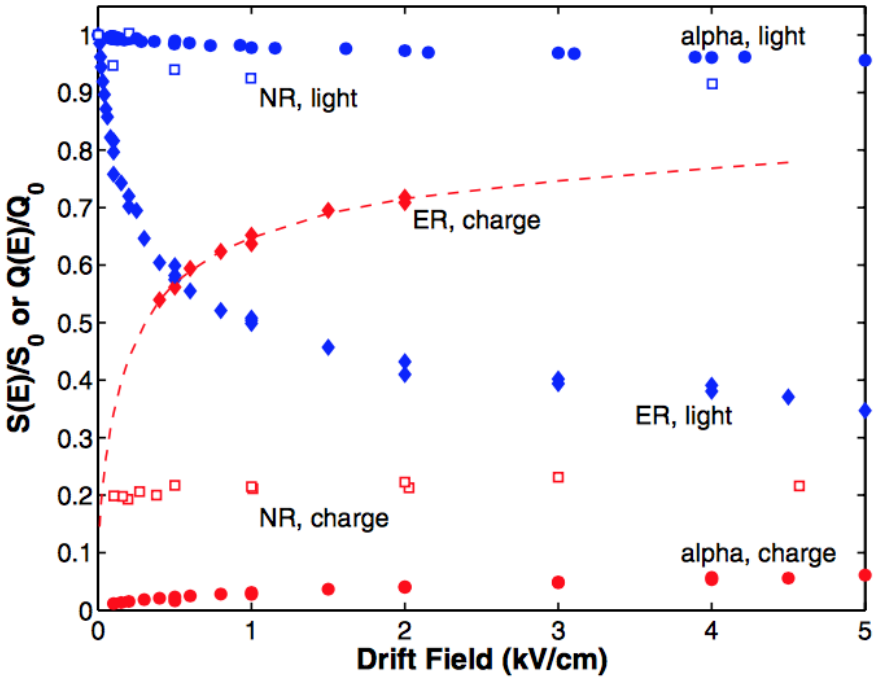

Figure 3.6 *Scintillation (blue) and ionisation (red) yields as a function of drift field in liquid xenon, for 122 keV$_{ee}$ electron recoils (full diamonds), 56.5 keV$_{nr}$ nuclear recoils (open squares), and α particles (full dots) [122].*

The relative scintillation efficiency is the relationship between the scintillation per keV for electron recoil and the one for nuclear recoil, and can be calculated as [124]:

$$\mathcal{L}_{eff} = \frac{E_e}{E_n} \cdot \frac{S_e}{S_n}. \tag{3.8}$$

Some measurements of $\mathcal{L}_{eff}$ as a function of nuclear recoil energy are reported in Fig. 3.7. Results have not always been consistent with each other, leading to an uncertainty in the estimate of the nuclear recoil energy, E_n, when defined via Eq. 3.8. Nevertheless, a common trend in the results suggests that $\mathcal{L}_{eff}$ decreases as the energy decreases. Measurements of the relative scintillation efficiency below 4 keV$_{nr}$ are missing in Fig. 3.7, and would be relevant to constrain light WIMPs.

If we call L_y the light yield, that is the number of photoelectrons detected per unit energy, and Q_y the charge yield, that is the amount of charge detected per unit energy, then the expressions for recoil energies can be rewritten. The electron recoil energy becomes $E_e = S1/L_y$, and the nuclear recoil energy reads

$E_n = S2/Q_y$. Moreover, Eq. 3.8 can be inverted:

$$E_n = \frac{S2}{Q_y} = \frac{1}{\mathcal{L}_{eff}} \cdot \frac{S1}{L_y} \cdot \frac{S_e}{S_n}. \tag{3.9}$$

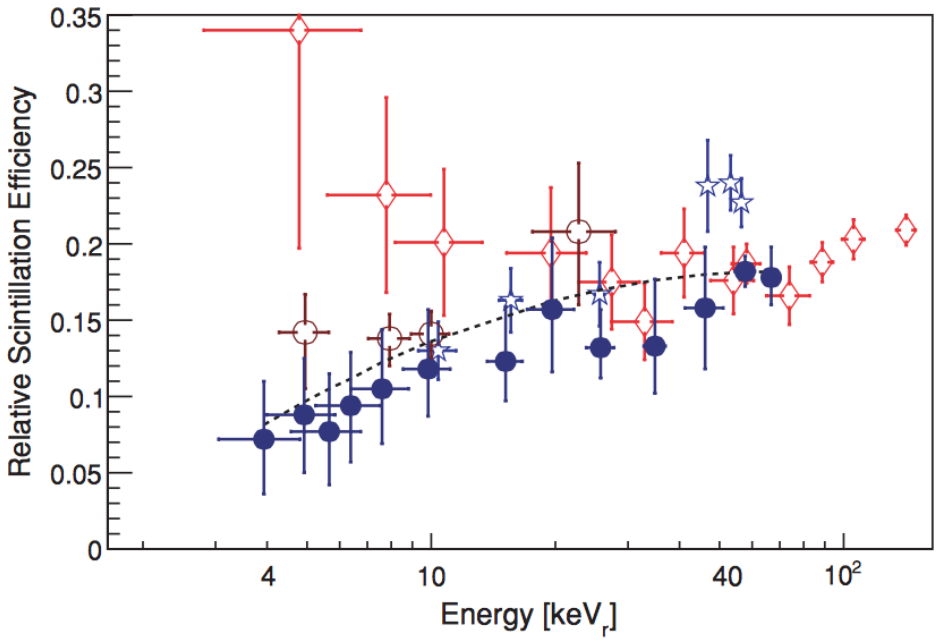

Figure 3.7 *Some measurements of the relative scintillation efficiency in liquid xenon, $\mathcal{L}_{eff}$, as a function of nuclear recoil energy. Measurements have been performed by Manzur (full blue dots), Aprile (blue stars and empty brown dots), and Chepel (red diamonds) [124]. A common trend in the results suggests that $\mathcal{L}_{eff}$ decreases as the energy decreases.*

Eventually, it is possible to express the relative scintillation efficiency in terms of three factors, each accounting for an energy loss:

$$\mathcal{L}_{eff} = \mathcal{L} \cdot q_{esc} \cdot q_{el}. \tag{3.10}$$

As already introduced, the Lindhard factor, $\mathcal{L}$, accounts for some energy being lost to atomic motion or heat. The loss in scintillation light yield due to those electrons that avoid recombination by escaping from the interaction site is expressed by the factor q_{esc}. The fraction of light getting lost because of biexcitonic collisions, that happen when two excitons produce a single photon instead of two, is defined as q_{el}.

The energy deposition in a dual-phase TPC can be described in terms of N_{ex} and N_i, introduced in Eq. 3.4 as the number of excitons and electron-ion pairs produced by an interaction, respectively. The energy deposition will then read [125]:

$$E = fW(N_{ex} + N_i) = fW\left(1 + \frac{N_{ex}}{N_i}\right) N_i, \tag{3.11}$$

where $W = 13.7 \pm 0.2$ eV is the average energy needed to produce a single excited or ionised atom, called the work function. f represents the quenching factor, and its value depends on the nature of the interaction: while it is negligible for electron recoils, it is not for nuclear recoils. The quenching can be expressed as:

$$\begin{aligned} f(ER) &= 1, \\ f(NR) &= \frac{1}{\mathcal{L}}. \end{aligned} \tag{3.12}$$

N_{ex} and N_i are not directly measurable. The quantities we can have access to are the deexcitation photons, n_γ, and the electrons escaping recombination, n_e. They are expressed as:

$$n_\gamma = \left(\frac{N_{ex}}{N_i} + r\right) N_i, \tag{3.13}$$

and

$$n_e = (1 - r)\, N_i, \tag{3.14}$$

where r represents the fraction of the initial electron-ion pairs that recombines, forming more excitons. n_γ and n_e are directly related to the $S1$ and $S2$ signals. The energy can be rewritten in terms of these quantities:

$$E = fW(n_\gamma + n_e) = fW\left(\frac{S1}{g_1} + \frac{S2}{g_2}\right), \tag{3.15}$$

where both $S1$ and $S2$ are in units of detected photons (phd), while g_1 and

g_2 represent the detector gains in units of phd/quantum. In more detail, g_1 takes into account both the light collection efficiency and the PMT quantum efficiency, representing the overall photon detection efficiency for the prompt scintillation. Similarly, g_2 is the overall detection efficiency for the secondary signal, consisting of the product of the electron extraction efficiency (from liquid to gas) and the average single electron pulse size in phd. The quenching factor, f, will depend on the type of recoil (c.f. Eq. 3.12), and the units measuring the energy will change accordingly. Energy of electron recoils is measured in keV_{ee}, while keV_{nr} are used in the case nuclear recoils. Detector calibrations allow for measuring $S1$s and $S2$s from sources with known energy distribution, making it possible to quantify the gain factors and a correspondence between keV_{ee} and keV_{nr}. This will be discussed in the last section of this chapter.

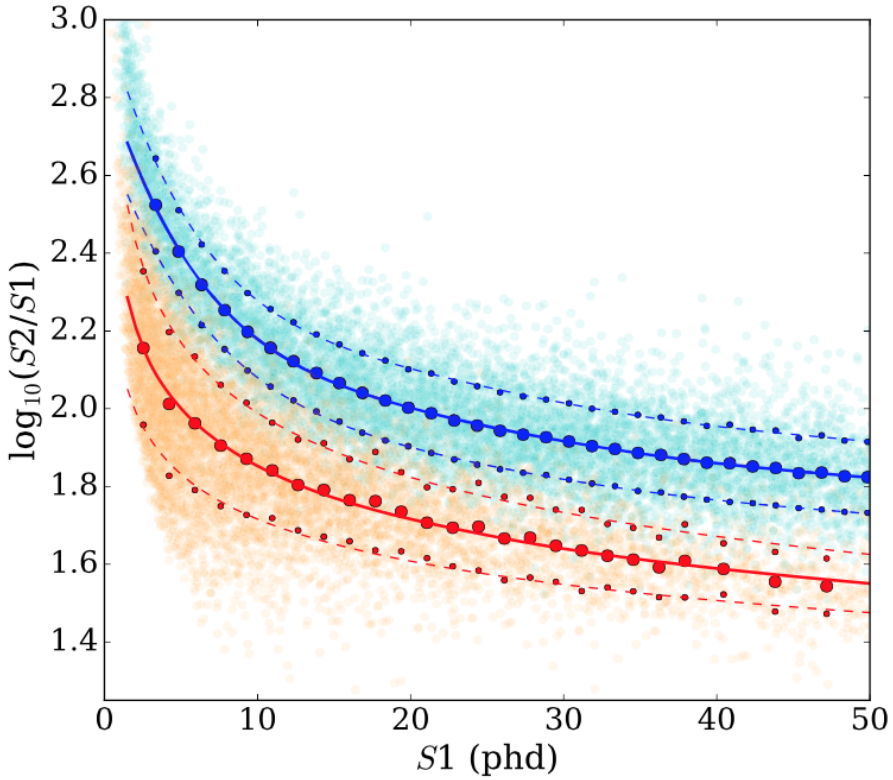

Figure 3.8 *LUX calibration data form two bands. Electron recoil events are cyan, nuclear recoil events are orange. Large and small filled circles identify, respectively, the fitted band Gaussian mean and the fitted Gaussian* $\pm$ 1σ *[125].*

As shown in Eq. 3.5 and 3.6, ionization yields for electron and nuclear recoils differ, inducing different $S2/S1$ ratios. As a consequence, data plotted on a $\log_{10} S2$ versus $S1$ phase space will form two distinct bands, as shown in Fig. 3.8. Because of electron recombination fluctuations in liquid xenon (and other effects

such as described later in this chapter), the two bands have a non-zero width [126]. Calibration data are usually employed to define the bands and their widths.

3.3 The LUX detector

The Large Underground Xenon (LUX) experiment is a dual-phase xenon time projection chamber, that has been designed for direct searches of dark matter. Located 4850 feet underground (4300 m w.e.) at the Sanford Underground Research Facility (SURF) in Lead, South Dakota (U.S.A.), LUX has been taking data since 2013. The LUX Collaboration published several world leading results on WIMP searches, and other rare events analyses (details will be found in Chapter 4, 5, and 6).

The LUX detector is located in the Davis Cavern at SURF. The Davis Cavern is a clean laboratory, built in one of the tunnels of a former gold mine, known as Homestake mine. To reach the laboratory, scientists use a cage that goes down in a shaft. Once reached the 4850-feet level, the access to the Davis Cavern is by a tunnel, as shown in the top panel of Fig. 3.9. The experimental set-up is distributed on two levels (c.f. Fig. 3.9). The top floor hosts both a control and a clean room, while the water tank containing the detector is placed downstairs, as well as part of the electronic readout. The laboratory is 12 m high. To give an idea of proportions, the water tank is sketched next to a human body in Fig. 3.10.

The location deep underground has been chosen to ensure a highly-reduced level of cosmic-rays background. Moreover, all components used for the LUX detector were screened for γ rays, to meet the overall low-background goals. Also, the liquid xenon used to fill the detector underwent a krypton removal campaign. Details about the background requirements and levels will follow.

LUX has finished its operations in the summer 2016 and has been decommissioned starting in September 2016. The LUX project is not finished though, as the Collaboration is currently analysing legacy data and working on LUX's upgrade, the LUX-ZEPLIN (LZ) experiment. LZ will take place in the same laboratory where LUX has operated, starting in 2020.

The working principle of LUX is the same as the other dual-phase TPCs. The choice of xenon as target material has been already discussed. This section is dedicated at the description of the LUX detector in its components and

operations. A detailed overview of the expected sources of background in LUX is also presented.

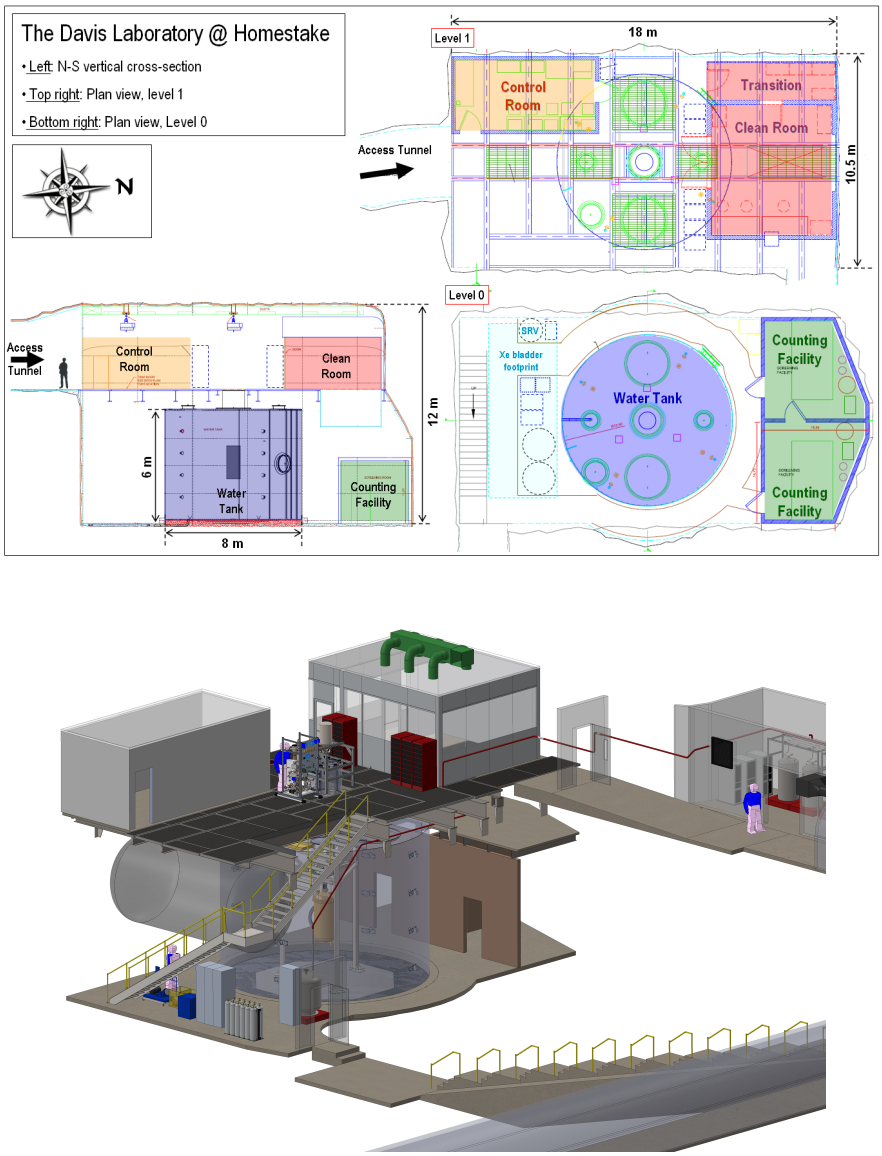

Figure 3.9 *The Davis Cavern. Top: a vertical section (left panel) and two plane views of the two levels (right panel) of the laboratory. Bottom: a three-dimensional view of the laboratory is presented to show the two levels on top of each other.*

3.3.1 Detector internals

The LUX detector is a cylindrical chamber, 60 cm high by 50 cm in diameter, filled with 370 kg of liquid xenon of which 250 kg are in the active region. A schematic cross-sectional view of the apparatus is shown in Fig. 3.11. The detector is placed

within a low-radioactivity titanium cryostat, called the inner vessel, which is housed in a second cryostat, called the outer vessel, and made of titanium as well. Between the two vessels, vacuum is maintained to better insulate the inner vessel, that is maintained at approximately 175 K. Instrumentation cables connect the detector with the outside through conduits placed at the top of the vessels.

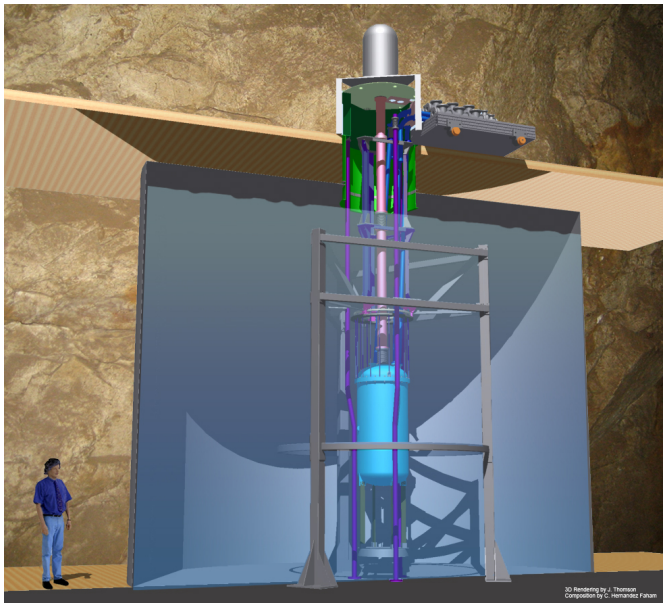

Figure 3.10 *The LUX tank in the lower level of the Davis Cavern. A human scale is given to show proportions. The thermosyphon-based heat-exchange system is also presented: the grey dewar at the top represents the liquid nitrogen bath, and the pink tube shows the connection between the bath and the detector.*

The outer cryostat is contained in the water tank, the light blue cylinder in Fig. 3.10, that is supported by a stainless steel structure. The water tank is 6.1 m high, has a diameter of 7.6 m, and contains 8 tons of water. The detector is thus cheaply and effectively shielded by 2.75 m of water at the top, 3.5 m at the sides, and 1.2 m at the bottom. Backgrounds produced by the cavern rocks, both γ rays and neutrons, are reduced by the water such that they become negligible with respect to the internal radioactivity from the detector components. To achieve this, the water is constantly purified by circulating in a purifying system.

The water tank also acts as a muon veto. Twenty Hamamatsu R7081 photomultiplier tubes (PMTs) are mounted on it, in order to detect muons that enter the tank and emit Cherenkov light. The veto system works such that any nuclear recoil event in the fiducial volume happening in coincidence with a tagged muon is removed from the data.

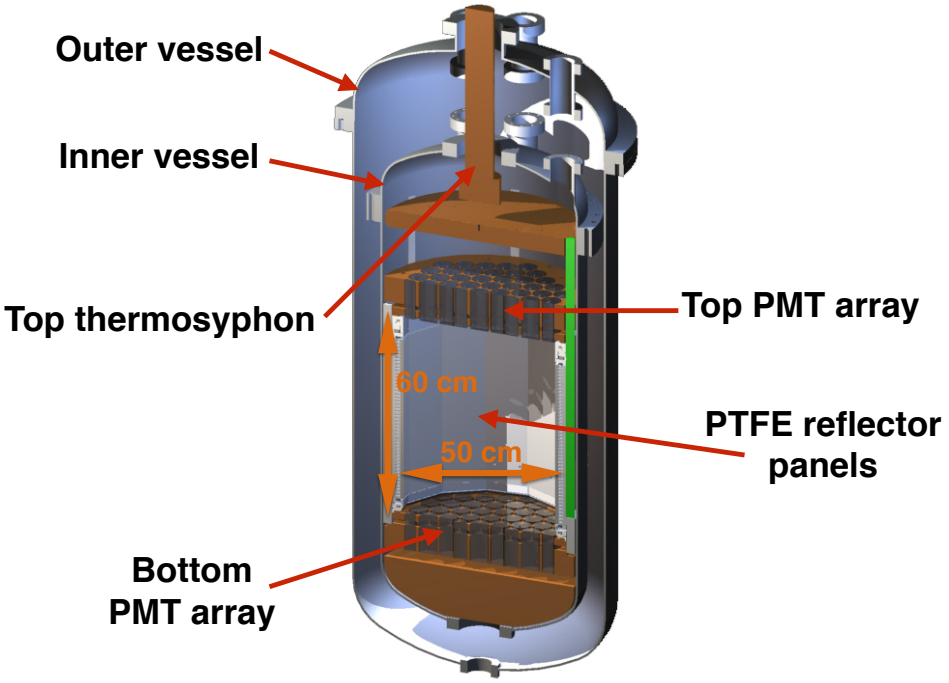

Figure 3.11 *Cross-sectional view of the LUX detector to show its interior and dimensions. Labels and arrows have been inserted to point some of the main features: the two vessels, the two PMT arrays, the thermosyphon, and the reflector panels.*

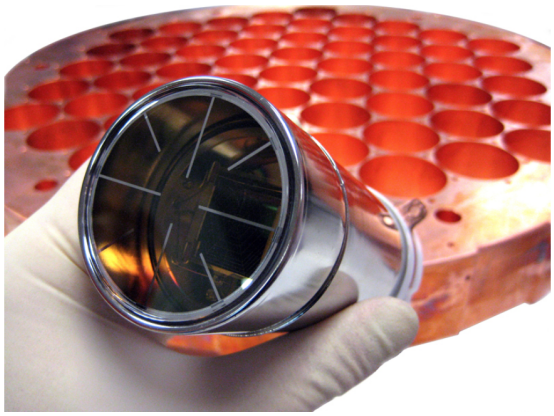

Figure 3.12 *A 5.6 cm diameter Hamamatsu R8778 PMT and one of the supporting copper blocks [105].*

As shown in Fig. 3.11, the detector is seen by two arrays of 61 Hamamatsu R8778 PMTs. Figure 3.12 shows one of these 5.6 cm diameter PMTs, and one of the supporting copper blocks that host the PMTs. These collect the scintillation light produced by interactions in the liquid xenon, with a typical quantum efficiency of 33% at 178 nm wavelength. LUX PMTs have been optimised for liquid xenon operation, and can work at 170 K and up to 5 atm of pressure [105].

The PMT arrays are inserted in a copper structure, internally covered by twelve polytetrafluoroethylene (PTFE) panels, as shown in Fig. 3.13. Other PTFE reflectors also cover the gaps between PMT faces. The reflector panels create the dodecagonal structure typical of LUX, and have the main function of increasing the light collection efficiency.

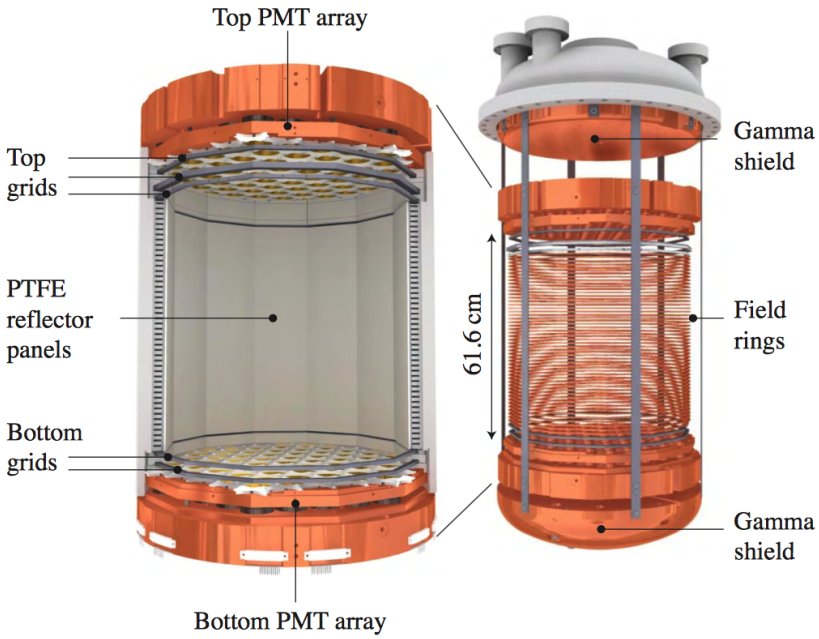

Figure 3.13 *Inner section of the LUX detector. PMT arrays, grids and PTFE panels are highlighted, as well as the electric field rings and the copper γ shields [105].*

Moreover, the PTFE panels support the field cage. The electric field is defined by five wire grids made of stainless steel. The bottom grid is located 2 cm above the bottom PMT array, and has a voltage such that the electric field at the photocathode of the PMTs is zero. The cathode grid is placed 4 cm above the bottom PMT shield, while the liquid xenon surface nominally lays 49.5 cm above the cathode grid. The gate grid sits $\sim$ 5 mm below the liquid surface, whose level is precisely maintained by a weir reservoir into which xenon between gate and anode can flow. The anode, located 1 cm above the gate, and the gate itself, produce a 5 – 6 kV/cm extraction field that pulls the electrons out of the liquid xenon and into the gas phase to generate the $S2$ signal. This electroluminescence process is possible thanks to the electric field that is generated by anode and cathode, and dritfs the electrons towards the liquid xenon surface. The fifth grid is the top one, located 4 cm above the anode and 2 cm below the top PMT array. As for the bottom grid, this is used to ensure that the electric field at the

photocathode of the top PMTs is zero. A resistor chain between the gate and the cathode is used to fix the voltage of the field rings.

As shown in Fig. 3.13, copper structures are placed at the top and at the bottom of the detector. In the former case, a copper disk connects the TPC to the vessel; in the latter, a dome-shape structure is used to displace inactive xenon. Both of them act as additional γ-ray shields. The top copper disks is also connected to the top thermosyphon, as indicated in Fig. 3.11.

Four thermosyphons constitute the unique cryogenic system of LUX, by being connected to a liquid nitrogen bath, placed in a dewar above the detector, as shown in Fig. 3.10. A liquid nitrogen system, consisting of four storage tanks, automatically refills the bath if its level drops below 50% of the full value. Each tank has 450 L capacity and is kept underground, while a fifth tank of 1100 L capacity is filled on the surface and taken underground to refill the storage tanks up to 90% capacity. A photo taken during a typical refill operation conducted by the author can be seen in Fig. 3.14.

Figure 3.14 *Davis Cavern (SURF): a colleague and I operating in one of the tunnels to refill the liquid nitrogen storage tanks.*

Each of the thermosyphons is a tube that consists of a condenser immersed in the liquid nitrogen bath, that is connected through a passive stainless steel guide to a copper cold head, called the evaporator and attached to the inner vessel. The working principle is based on gravity and on thermosyphons being pressurised with gaseous nitrogen: this condenses in the condenser, then flows down the guide reaching the cold head. When in contact with the warmer vessel, the nitrogen evaporates, removing heat from the detector. The gaseous nitrogen then rises up along the tube because of its lower density. When it reaches the cold liquid nitrogen, it condenses again and the process restarts.

The larger thermosyphon in LUX is the top one, represented as the pink tube in Fig. 3.10. This and the bottom one are used to cool the detector from room temperature down to 175 K, as slowly and uniformly as possible. Attached to the copper shield of the inner vessel there are two other cold heads, with the function of controlling the temperature gradient along the vertical axis.

The temperature of the detector, as well as the other parameters that determine whether operations are proceeding normally, are monitored by several sensors that are placed within the experimental apparatus.

The temperature sensors are 100 Ω platinum resistors, that are put in contact with the surface to be monitored through ceramic substrates. Forty of these sensors are placed inside the inner cryostat to check on temperature fluctuations, while 23 of them operate in the vacuum space between the inner and the outer vessel to make sure no leakage is happening. Temperature detectors have been calibrated and tested both prior to installation and in situ, and the accuracy of their measurements has been determined to be of 170 mK.

Several pressure sensors are installed throughout the detector. They are meant to monitor that the pressure is stable within the inner cryostat, as well as in the outer vacuum. They are also placed in the gas circulation system that has been described above, to keep track of leakages.

Two types of level sensors are used in LUX. Parallel-wire sensors measure the liquid level in the inner vessel, the weir, the condenser, and the line xenon returns to the active region through after the circulation cycle. The level of the liquid is obtained by measuring the capacitance of the wire pairs, as it depends on the length of the submerged portion of the wires. Parallel-plate level sensors are inserted between the gate and the anode grids, to ensure a uniform liquid xenon surface, thus a uniform electron extraction field.

All the sensors are configured such that an alarm is triggered if the measured level exceeds either its lower or upper threshold. The alarm is generated by the LUX slow control, a database implemented to collect and store all data coming from the detector instrumentation. Users can easily access the slow control interface through a web browser, and thus constantly monitor the detector status. In case an alarm is triggered, and according to its severity, people on-site and off-site are alerted by a preset combination of lights, sirens, emails, and text messages.

Table 3.1 summaries some of the main parameters that describe the LUX detector.

Liquid xenon	
Total mass	370 kg
Active mass	250 kg
TPC	
Height	60 cm
Diameter	50 cm
Electric field	5 – 6 kV/cm
Drift velocity	1.51 ± 0.01 mm/μs
Water tank	
Height	6.1 m
Diameter	7.6 m
Total mass	8 tons
PMTs	
Total number	122
Diameter	5.6 cm
Efficiency	33%

Table 3.1 *Parameters of the LUX detector.*

3.3.2 External systems

Beside providing the cryogenic system of the LUX detector, thermosyphons also have the function to adjust the temperature of the returning xenon in the circulation system – a system that has been designed to circulate xenon, so that the purification of it is guaranteed throughout the data taking. Xenon is moved from the detector to a hot metal getter in order to remove impurities, and then sent back into the detector. Two pumps power the system, pushing xenon along the path. A typical cycle works in the following way. Xenon from the top of the active region spills into the weir reservoir and then in an evaporator, as the getter requires gaseous xenon. Xenon in gas phase moves along a tube, where it warms up to room temperature, and is eventually pumped in the getter, where it is purified. After cooling down and condensing, the xenon goes in the lower γ-ray shield (indicated in Fig. 3.13). The thermosyphon ensures that the temperature of returning xenon is the same as the rest of the target, before it is reinserted at the bottom of the active region.

Within the circulation system, there are five ports connected to the gas sampling system. The purpose of having such a system is to regularly monitor the level of impurities in the xenon target. Given the different pressures of xenon and impurities, they are separated. The impurities level is analysed to make sure it meets expectations, while xenon can either be discarded or recovered in the storage and recovery vessel (SRV).

The SRV has also been designed as an emergency device, hosting the xenon target in case it has to be extracted by the detector for any reason. The xenon recovery system can be automatically activated by the automated controlled recovery system (ACRS). The ACRS constantly performs checks on the detector parameters by using the sensors, to determine whether a recovery is necessary.

Calibrations of the LUX detector are performed to determine the detector response to recoil events, as will be discussed in detail in the next section. The LUX calibration system was implemented to deal with both internal and external sources.

Six dry source tubes are inserted within the water tank to surround the outer cryostat, as shown in Fig. 3.15. The reason for having the tubes in the water is that the radioactive sources would be otherwise attenuated by the water, making the calibrations less effective. The sealed radioactive sources are inserted in the

tubes and taken out of them through a system of pulleys, that is also used to adjust the position of the source along the vertical dimension of the detector. A system of collimators ensures that γ-rays sources are directionally controlled.

The already discussed self shielding property of xenon implies difficulties in calibrating the very inner fiducial volume by use of external sources only. For this reason, two internal calibration sources are employed: ^{83m}Kr and tritiated methane (CH3T). These sources are injected directly in the circulation system, and uniformly and quickly disperse in the fiducial volume. An important difference between ^{83m}Kr and CH3T is that, while the former decays away within 1.86 hours after the injection, the latter has to be removed from the detector using the getter in the circulation system, as it has a half-life of 12.3 years.

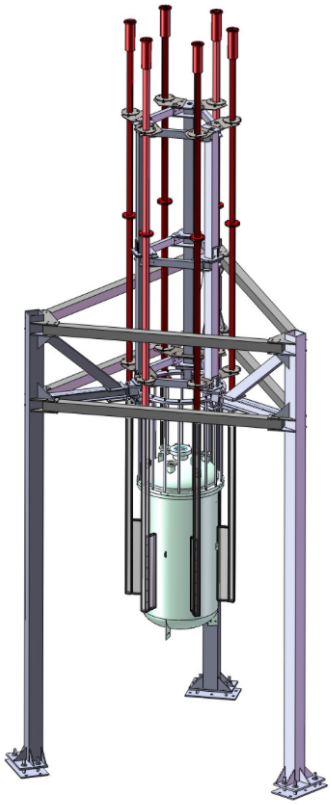

Figure 3.15 *The six external source tubes, used for sealed calibration sources in LUX, are drawn in red [105].*

An additional source of calibration in LUX is a neutron beam, that is produced by a D-D neutron generator operating outside the water tank [127]. To introduce neutrons in the detector, a 377 cm-long air-filled pipe is inserted in the water tank to cover the distance between the tank and the wall of the outer vessel. The pipe creates a collimation path for the neutrons to come in, by

displacing water from the tank.

3.3.3 Detector electronics and DAQ

Interactions happening within the detector, either due to calibration sources or to background (signal) events, are recorded by the two arrays of PMTs that face the liquid xenon from the top and the bottom. Other 20 PMTs observe the water tank. Both analogue and digital electronics form the LUX PMT readout, that is connected with the triggering system, as well as with the LUX data acquisition system (DAQ) [128]. The aim of this chain, shown in Fig. 3.16, is to maximise the signal-to-noise ratio.

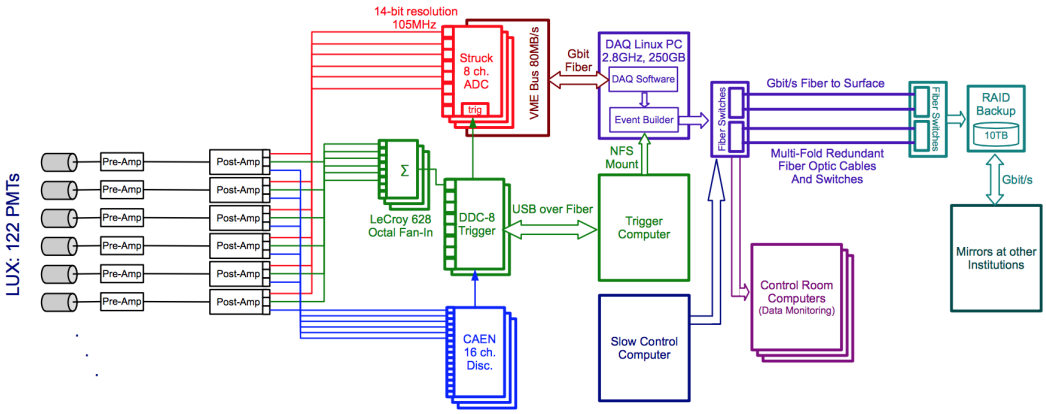

Figure 3.16 *Data flow diagram of the LUX electronics and DAQ [128].*

The first two stages in the analogue electronics chain are the preamplifier and the postamplifier, both dedicated to amplify signals collected by the PMTs. Signals enter the preamplifier immediately after exiting the xenon space, while the postamplifier is located near the digitisers and the triggering system. The gain of LUX PMTs is 3.3×10^6. A single photoelectron produces a pulse with an area of 13.3 mV ns and a FWHM of 7.7 ns at the PMT base.

The analogue to digital converters (ADCs) perform real-time baseline suppression. The requirement is to resolve $\gtrsim 95\%$ of single photoelectron pulses from 5σ fluctuations in the baseline noise. The left panel of Fig. 3.17 shows an example LUX PMT pulse, highlighting fluctuation and detection thresholds. LUX uses the Pulse Only Digitization (POD) acquisition mode, that has been optimised for baseline-dominated signals. The working principle of POD is shown in the right panel of Fig. 3.17. The POD reads pulses from channels pairs, acquiring a signal

only if the detection threshold has been reached in either of the channels. In this way, the DAQ is prevented by storing baseline information.

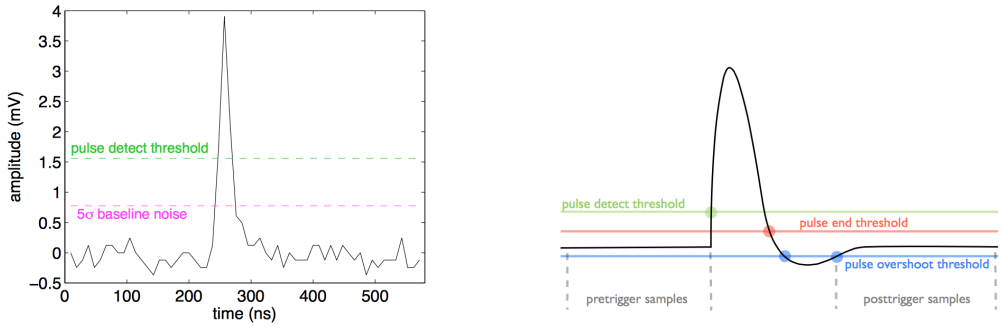

Figure 3.17 *Left panel: single photoelectron pulse from one of the LUX PMTs, as well as pulse detect threshold and 5σ upward fluctuation in the baseline noise. Right panel: illustration of the Pulse Only Digitization (POD) mode and thresholds [128].*

The LUX DAQ has been designed to operate in either calibration or search mode, whose expected event rates are quite different. Calibration campaigns are set such that the total event rate is up to 200 Hz, while the expected background rate in physics runs is only 1.2 Hz.

3.3.4 Background sources

As in any other experiment searching for rare events, backgrounds play a crucial role in LUX. Given previous results, the goal of any such an experiment is to reduce the background level as much as needed to reach the sensitivity for dark matter discovery. The LUX programme aimed at maintaining the background expectation to < 1 WIMP-like background event in 30,000 kg days [105]. Backgrounds are expected to produce either electron recoil or nuclear recoil classes of events.

Contributions to the background in LUX come from different sources. Moving from the outside towards the inner xenon volume, either the external environment, or the cavern rocks, or the detector materials, or the liquid xenon itself contribute to the overall background seen in LUX. The location of the detector 4850 feet underground, the material screening campaigns, the water tank shield, and the purification of the xenon target are some of the strategies used to control the level of background. Also, the self shielding property of xenon makes the centre of the LUX detector a low-background volume, where background coming from

the outside with relatively small energies travel only a few millimeters. γ rays with $\sim$ MeV energies have a mean free path of several centimeters, enough to produce a multi-scatter signature that is easy to recognise.

The water tank surrounding the LUX vessels is designed to ensure that the backgrounds coming from the external environment are sub-dominant to the internal backgrounds generated within the detector. The Davis cavern rocks are the main source of the electron recoil component of the external background, as they contain ^{40}K, ^{238}U and ^{232}Th, that decay emitting γ rays. The content of radioactive isotopes depends on the quality of the rocks, and is unknown. Given the most conservative assumption, as in the cavern completely composed of rhyolite, the expected flux of γ rays reaching the water tank is 9 γ cm^{-2} s^{-1}. Simulations show that the effect of the water shield is to reduce such a flux by a factor of 2×10^{-10}.

External backgrounds also contribute as nuclear recoil events, because of an environmental neutron flux, with neutron energies larger than 1 MeV. These neutrons are mainly produced by ^{238}U spontaneous fission and (α,n) reaction, that happen in the rocks and concrete of the laboratory. Given the rhyolite-based assumption as above, the estimated incident neutron flux is 16.2×10^{-9} cm^{-2} s^{-1}, at the external edge of the water tank. The shield provided by the water works efficiently also in this case, reducing the neutron flux reaching the detector to 10^{-16} yr^{-1}.

Muons coming from the external environment into the Davis cavern interact with both the laboratory rocks and the water tank, producing neutrons of energies $\sim$ GeV that are one of the components of the nuclear recoil background. This muon-induced background is reduced thanks to the choice of an underground experimental site. A $(4.4 \pm 0.1) \times 10^{-9}$ cm^{-2} s^{-1} muon flux is expected at SURF [129]. This induces a $(0.54 \pm 0.01) \times 10^{-9}$ cm^{-2} s^{-1} flux of neutrons from the cavern rocks, that is attenuated by the LUX water shield such that 1×10^{-7} neutrons per second reach the cryostat. Nevertheless, the water also acts as a neutron generation environment. Muons interact within the water tank and produce 6.3×10^{-7} neutrons per second, that will get to the outer cryostat.

LUX construction materials contain ^{238}U, ^{232}Th and ^{226}Ra, as well as contaminations such as ^{40}K and ^{60}Co. All these isotopes generate γ rays that can interact in the fiducial volume, with energies typically between 100 keV and several MeV. The presence of these isotopes is expected in the PMTs, the

PTFE reflector panels, the titanium cryostat, the stainless steel grids, and the thermal insulation. All these components have been assayed for their radioactive content before being used in the detector construction. Titanium and copper also contributed with their cosmogenic activation products: ^{46}Sc and ^{60}Co, respectively. These materials have been activated during the two-years time when the LUX detector was assembled and operated at the Sanford Surface Laboratory. Screening results for each of the components have been used to model the background expectations, and are listed in Fig. 3.18.

Component	Counting Unit	Counting Results [mBq/unit]					
		^{238}U	^{226}Ra	^{232}Th	^{40}K	^{60}Co	Other
PMTs	PMT	<22	9.5±0.6	2.7±0.3	66±6	2.6±0.2	
PMT bases	base	1.0±0.4	1.4±0.2	0.13±0.01	1.2±0.4	<0.03	
Field ring supports (inner panels)	kg		<0.5	<0.35			
Field ring supports (outer panels)	kg		<6.3	<3.1			
Reflector panels (main)	kg		<3	<1			
Reflector panels (grid supports)	kg		<5	<1.3			
Cryostats	kg	4.9±1.2	<0.37	<0.8	<1.6	4.4±0.3 (^{46}Sc)	
Electric field grids	kg		1.4 ± 0.1	0.23 ± 0.07	<0.4	1.4 ± 0.1	
Field shaping rings	kg		<0.5	<0.8		<0.3	
PMT mounts	kg		<2.2	<2.9		<1.7	
Weir	kg		<0.4	<0.2		<0.17	
Superinsulation	kg	<270	73±4	14±3	640±60		
Thermal insulation	kg		130±20	55±10	<100		

Figure 3.18 *Table summarising the radioassay results for the LUX detector components. Results are given in units of mBq/unit, and include estimations of the presence of cosmogenically activated isotopes [130].*

In addition to the electron recoil backgrounds, construction materials are also responsible for the main component of the nuclear recoil background. Neutrons generated through (α,n) reactions in the detector components scatter on xenon nuclei. Dominant sources of this type of background are ^{238}U and ^{232}Th in the PMTs, as well as α particle interactions in the PTFE walls.

The LUX xenon target has been accurately purified, such that the only significant contributions to the background due to the liquid xenon come from its homogeneously distributed radioisotopes, that decay generating β rays or x rays. Thermal neutron capture is the dominant production mechanism. Not being measured, it results in a systematic uncertainty on the predicted activities of the four xenon isotopes to be considered: ^{127}Xe, ^{129m}Xe, ^{131m}Xe, and ^{133}Xe. Each of these isotopes is listed in the left panel of Fig. 3.19, along with its half-life and decay rate, both predicted and observed. All the contributions have been identified in early LUX data, as proven by the right panel of Fig. 3.19, where peaks due to xenon radioisotopes are labelled.

Isotope	Half-life [Days]	Decay Rate [μBq kg^{-1}] Predicted	Observed
^{127}Xe	36	420	490 ± 95
^{129m}Xe	8.9	4.1	3.2 ± 0.6
^{131m}Xe	12	25	22 ± 5
^{133}Xe	5.3	0.014	0.025 ± 0.005

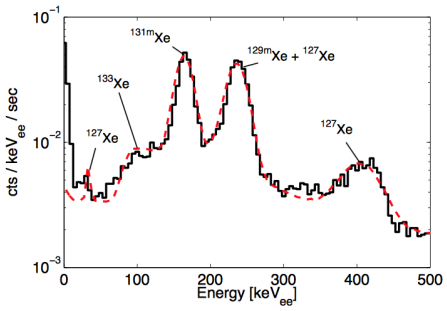

Figure 3.19 *Left panel: Xe radioisotopes are listed with their half-life, predicted and observed decay rate (after 90 days underground). Right panel: peaks due to Xe radioisotopes are identified in the energy spectrum. The solid black spectrum is LUX data taken 12 days after the detector has been taken underground, while the dashed red curve represents the best-fit spectrum [130].*

Considering the half-lives, only ^{127}Xe will constitute a relevant background for the LUX data taking, and only in the 2013 campaign, as it is expected to decay away by the start of the final LUX data taking. The decay process of ^{127}Xe is an electron capture resulting in an orbital vacancy. Electron transitions will fill the vacancy and produce an x-ray or Auger electron cascade. 85% of electron captures come from the K shell, causing a cascade of 33 keV total energy, while a further 12% of captures come from the L shell, producing a cascade of total energy 5.2 keV.

Further significant contributions to the LUX background arise from ^{85}Kr and Rn-daughter contaminants in the liquid xenon. Their decay cascades lead to the emission of β rays that either can or cannot be accompanied by γ rays. In case that no γ ray is emitted or it escapes the active volume, it is not possible to tag these events and they become a source of background.

Radon isotopes, ^{222}Rn and ^{220}Rn, decay through several short-lived daughter stages. ^{222}Rn generates ^{214}Pb and ^{214}Bi, whose activity is expected in the range 3.5 – 14 mBq in the active region [2]. ^{220}Rn generates ^{212}Pb, that then decays in ^{214}Pb, with an expected rate smaller than 2.8 mBq. These constraints are obtained thanks to radon daughters identification, that is done through parent and daughter α decays. Indeed, α particles produce $S1$ pulses much larger than pulses related to γ-ray events.

The LUX liquid xenon initially contained an average of 130 ppb g/g ^{nat}Kr/Xe.

[2]Direct measurements in LUX data provide a stronger constraint for the decay rate of ^{214}Pb, that is expected to be < 8 mBq.

^{85}Kr is an unstable isotope of Kr, present with estimated concentrations of 2×10^{-11} (g/g) in natural krypton. Being a noble element, krypton is not affected by the getter of the purification system, as it acts only on impurities. The 687 keV-endpoint β emission due to the decay of ^{85}Kr (half-life of 10.8 years) thus produces an electron-recoil background. If the concentration of ^{nat}Kr stayed the original 130 ppb g/g, then such a background would be too high to meet the LUX background requirements. Prior data taking, a dedicated removal system was designed to reduce the concentration down to < 5 ppt, lowering the level of ^{85}Kr background to a quarter of the external γ-ray background level. The LUX sampling system inspected liquid xenon on a weekly basis during operations, ensuring that Kr levels were averaging at 3.5 ± 1.0 ppt g/g during the LUX data taking.

Tables 3.2 and 3.3 summarise, respectively, the contributions to the electron-recoil and nuclear-recoil background, in descending order of low-energy event rate. The expectations about all the contributions have been accurately modelled, in order to maximise the discrimination between background and signal in the data, for both electron-recoil band and nuclear-recoil band searches. The construction of the background model will be described in Chapter 4 and 5.

Source	Isotopes	Background
Rocks, construction materials	^{40}K, ^{238}U, ^{232}Th, ^{226}Ra, ^{60}Co	γ rays
Liquid xenon	^{85}Kr, Rn-daughters	β rays
Liquid xenon	^{127}Xe, ^{129m}Xe, ^{131m}Xe, ^{133}Xe	β rays, x rays

Table 3.2 *Contributions to the electron-recoil background in LUX, in descending order of low-energy event rate.*

Source	Isotopes	Background
Rocks, construction materials	^{238}U, ^{232}Th	neutrons
Muons	–	neutrons

Table 3.3 *Contributions to the nuclear-recoil background in LUX, in descending order of low-energy event rate.*

3.4 Data taking and calibrations in LUX

LUX has taken data since 2013. After a first run, a longer one has been carried on between 2014 and 2016. Data taken in LUX belong to two different categories, depending on their employment. Science data are searched for dark matter signals, while calibration runs are essential to determine detector response, efficiency, and resolution.

3.4.1 The LUX data

This part of the chapter is dedicated to a general description of the LUX data. The detector acquires pulses from the PMTs – pulses that undergo specific selection cuts to optimise the efficiency of the acquisition.

The primary scintillation signal, $S1$, is detected in both the top and the bottom PMT arrays, although the largest fraction of the light concentrates on the bottom one because of the total internal reflection at the liquid xenon surface. $S1$ light appears uniformly distributed on the arrays in x and y, and the pulses are short, around 20 samples (200 ns) in length. These features are distinguishable in Fig. 3.20, where the fired PMT arrays are shown on the left, and the $S1$ pulse as a function of samples is shown on the right. As a reference, an $S1$ of about 50 photons is expected for an energy of 2 keV_{ee} deposited in the centre of the detector, if a 1 kV/cm electric field is applied [118]. $S1$ pulses have a rise-time of $\sim$ 6 ns, and then decay exponentially with a time constant of 29 ns [128].

The $S1$ light collection in LUX has been estimated by simulating an energy deposit of 122 keV_{ee}. If no electric field is applied, then the light collection will be 10 photoelectrons/keV_{ee}. On the other hand, if a 1 kV/cm electric field is present, the light collection will be halved, because the electric field prevents some of the released electron from recombining. While recombination would increase the $S1$ signal size, the electrons drifting upwards generate the secondary $S2$ signal.

The $S2$ pulse is about three orders of magnitude larger than the corresponding $S1$ pulse, and appears as a Gaussian when summed over all PMTs. With respect to $S1$s, $S2$s are longer, usually 200 – 300 samples (a few microseconds) in length. Moreover, $S2$ pulses are concentrated on the top PMT array, driven by the proximity of the interaction site where the photons are coming from. Figure 3.21

presents a typical $S2$ pulse in LUX, as well as the map of the fired PMTs. The $S2$ light collection, for a 10 keV_{ee} energy deposition, is 45 electrons per keV_{ee} and 35 photoelectrons per each electron extracted from the liquid surface [118].

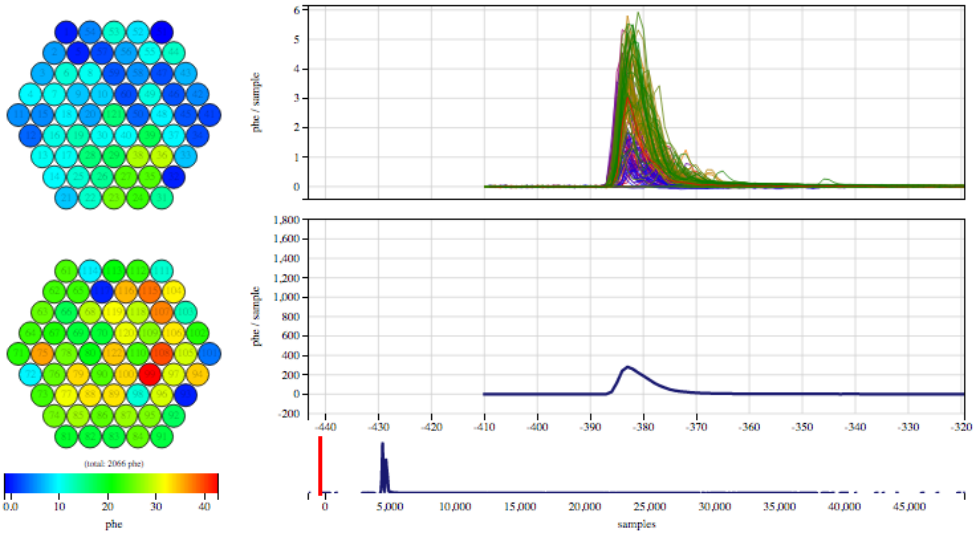

Figure 3.20 *Typical LUX S1 pulse: on the left, the map of the two PMT arrays; on the right, the individual PMTs (top) and the summed (bottom) responses. The light is mainly concentrated on the bottom PMT array, while it is uniform in x and y in both arrays. The pulse is short in length (20 sample, 200 ns).*

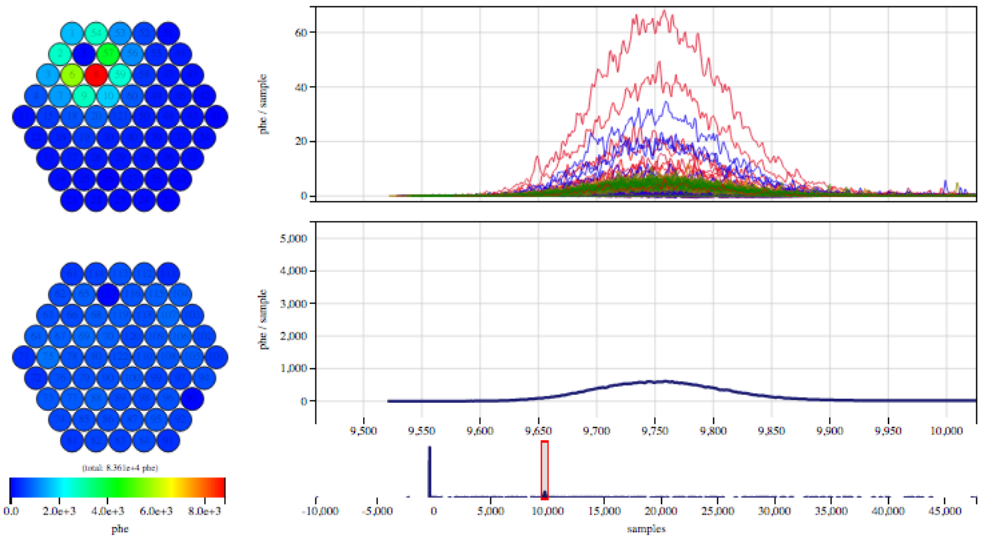

Figure 3.21 *Typical LUX S2 pulse: on the left, the map of the two PMT arrays; on the right, the individual PMTs (top) and the summed (bottom) responses. The light is localised in the top PMT array. The pulse is quite long in length (200 – 300 sample, ∼ 3 µs).*

The localisation of the $S2$ signal allows for the reconstruction of the event position in the horizontal plane, with a precision of 0.3 cm. The vertical

coordinate is obtained to 0.9 mm precision through the electron drift time, that is the time difference between $S1$ and $S2$ pulses, usually between 0 and 230 μs (given a 1 kV/cm electric field).

The selection of the events is based on $S1$ and $S2$ pulses. During science runs, the good events, called "golden events", consist of single scatters with a single $S1$ pulse followed by a single $S2$. The time difference between the two has to be between 0 and $\sim$ 350 μs (35000 samples). The order of the pulses is also important: if the $S1$ is recorded after the $S2$, then a random coincidence occurred, and the event is not selected. Golden events are required to be single scatters, as we do not expect dark matter candidates to produce multiple scatters within the fiducial volume. Multiple scatters are characterised by a single $S1$ followed by more than one distinct $S2$s, and are rejected in the event selection. Figure 3.22 shows a typical triple scatter event in LUX.

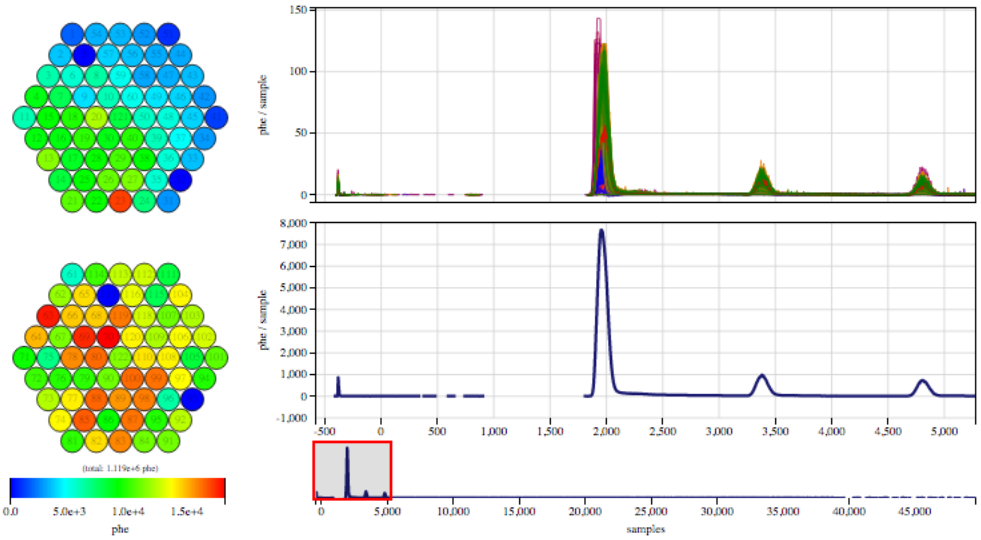

Figure 3.22 *Typical triple scatter event in LUX. A single S1 is followed by three distinct S2s.*

Quality cuts have been optimised to select golden events from science runs and build the LUX data sets. The first selection happens at trigger level, to ensure that the PMT pulse is not a baseline fluctuation. Detector stability cuts are employed to remove time periods of the run in which any of the detector parameters was out of normal ranges. Data collected soon after calibration campaigns are also excluded, as it is likely that traces of the calibration source might still be in the detector. The single scatter selection follows, with the requirement that the $S1$ pulse has at least two PMTs in coincidence.

In order to select the events in the energy region of interest, some area cuts are applied to $S1$ and $S2$ pulses. The reason for placing the cuts on these variables rather than on the reconstructed energy is that LUX observes $S1$s and $S2$s, while the energy is calculated afterwards in the analysis chain and depends on the type of event. The $S2$ signal has an accepted range of 10^2 – 10^4 detected photons, where the minimum threshold is needed to have enough photons to produce a reliable position reconstruction. The $S1$ pulse cut is analysis-dependent, as the energy window of interest depends on the dark matter candidate searched for. $S1$s are required to be in the range 1 – 50 (1 – 80) detected photons in the WIMP (axion and ALP) analysis. These thresholds will be discussed in more detail in Chapter 4 and 5.

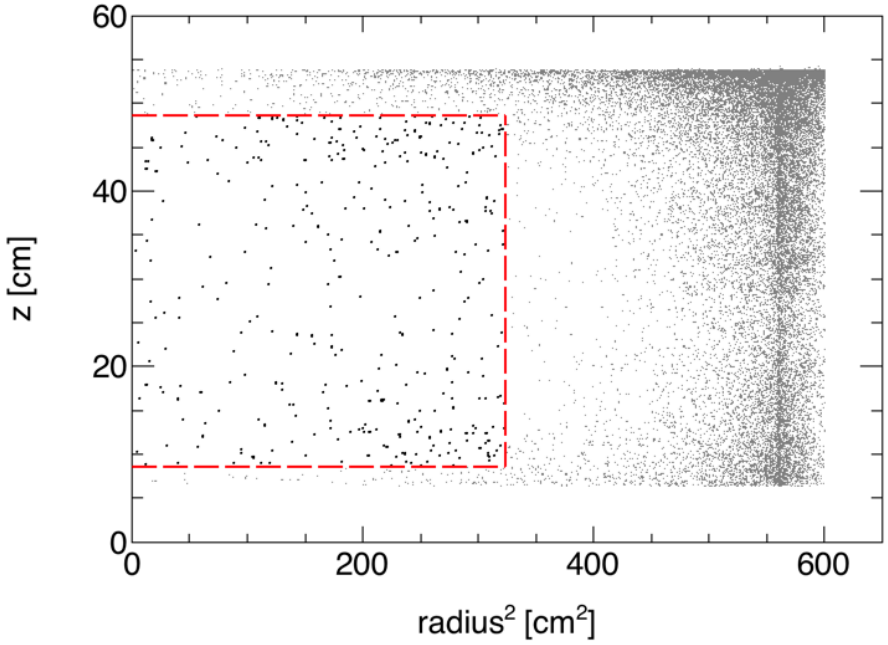

Figure 3.23 *Spatial distribution of LUX 2013 data in the LUX detector. Grey points are events that passed all the selection cuts but the fiducial cut. Black points falling within the dashed red box represent events that are selected by the fiducial volume cut. Note: the S1 cut applied to these events is 1 – 80 detected photons.*

Most of the events selected will fall at the edges of the detector, as shown in Fig. 3.23, where the LUX 2013 electron recoil data are shown after passing all the quality cuts discussed so far. To take advantage of the self shielding property of liquid xenon, fiducial cuts have been optimised. A radial cut is placed at 18 cm from the centre of the detector. Only the events falling within a 48.6 – 8.5 cm range above the faces of the bottom PMTs are selected, by requiring a drift time

of 38 – 305 μs. The dashed red box drawn in Fig. 3.23 defines the fiducial volume identified by these cuts. Such a fiducial selection reduces the number of events by two orders of magnitude.

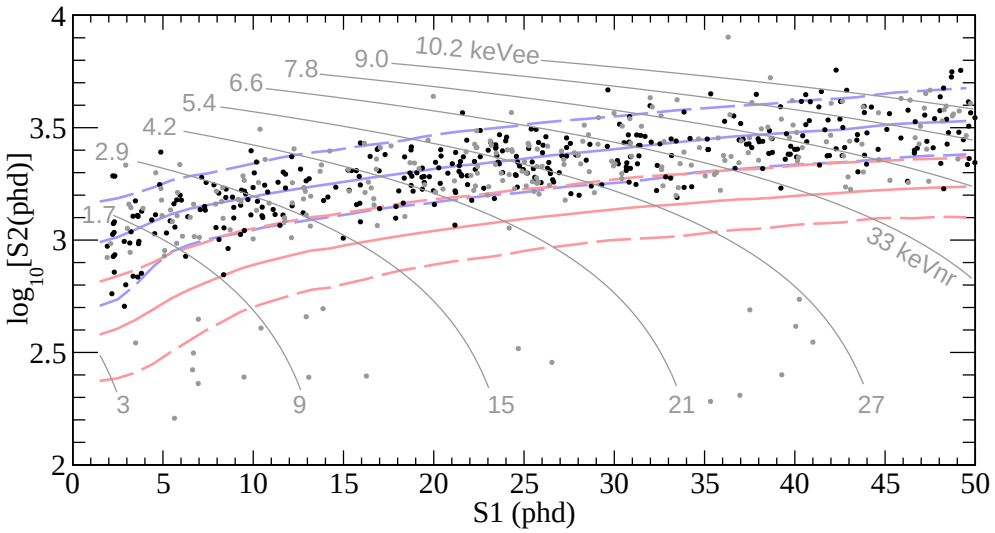

Figure 3.24 *LUX 2013 data:* $\log_{10} S2$ *as a function of S1. Events within 18 cm from the centre of the detector are the black dots, while grey dots are events whose radial position is in 18 – 20 cm. Grey lines trace energy contours, where both the keV$_{ee}$ and the keV$_{nr}$ scale are indicated. Distributions of uniform-in-energy electron recoils (blue) and a 50 GeV/c^2 WIMP signal (red) are indicated as well. Note: the S1 cut applied to these events is 1 – 50 detected photons [131].*

Figure 3.24 shows LUX 2013 data after all the selection cuts have been applied. Data are presented in the $\log_{10} S2$ versus $S1$ phase space. The black dots represent events within the 18 cm radial cut. Grey dots are events with radial coordinate between 18 and 20 cm – events that have been recovered using a data-driven model of background events originating on the detector walls, during the re-analysis of the data set. Energy contours are shown as solid grey lines, indicating the correspondence between keV$_{ee}$ and keV$_{nr}$.

The two bands identified by the blue and red curves represent a uniform electron-recoil distribution and a 50 GeV/c^2 WIMP signal, respectively. The calibrations are used to identify the distribution of electron and nuclear recoils on the $\log_{10} S2$ versus $S1$ phase space, as described below.

3.4.2 Calibrations of the LUX detector

The LUX calibration system has been described in the previous section, as one of the external systems of the LUX detector. It is used to calibrate LUX, in terms of detector response and energy scale, as well as detection efficiency and experimental resolution. Calibrations are also used to determine the boundaries of the bands in the $\log_{10} S2$ versus $S1$ phase space (c.f. Fig. 3.24).

Calibrations have been designed to cover such a wide scope of purposes, by employing both internal and external sources. As for the electron recoil band, β sources are used to calibrate the energy window from a few keV to a few tens of keV, while γ-ray sources are employed to cover the range from $\sim$ 100 keV to a few MeV. Neutron sources, as well as a D-D neutron generator, provide the calibration of the nuclear-recoil band and energy scale.

During LUX operations, a ^{137}Cs calibration is performed every week, on the first day underground. Two sources are inserted in the source tubes and pulled down to reach the designed position, where they sit for approximately 30 minutes. Figure 3.25 shows events collected during one of these calibrations: the photopeak due to the 661.7 keV γ ray rises over the Compton plateau.

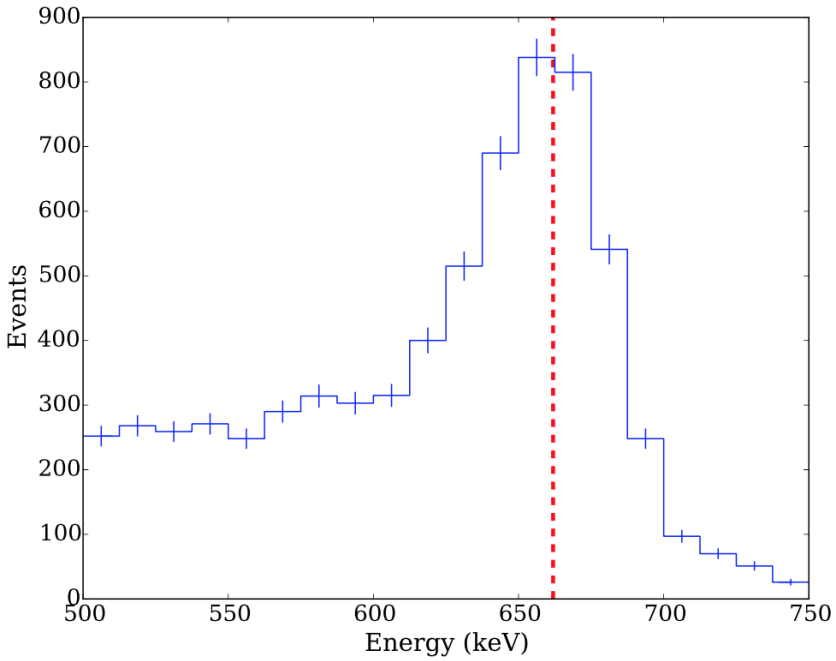

Figure 3.25 *Single-scatter events from an August 2013 ^{137}Cs calibration in the LUX fiducial volume. The true energy of the peak (661.7 keV) is indicated by the dashed red line [125].*

The calibration of the most inner volume of the detector through external sources can be difficult because of the self shielding property of xenon, thus two internal sources are employed in LUX, ^{83m}Kr and tritiated methane (CH3T). Both are dissolved in the liquid xenon.

Periodic ^{83m}Kr calibrations are performed during the LUX science runs [132] to determine the position dependence of the $S1$ and $S2$ signals, to calibrate the energy scale, and to monitor the detector stability. A ^{83}Rb source is used for this purpose, as ^{83}Rb decays to ^{83m}Kr with a half-life of 86.2 days, while not producing any other long-lived radioisotopes. The ^{83}Rb source is contained in charcoal, where ^{83m}Kr is constantly produced. When a calibration is needed, the charcoal is flushed with xenon gas and the flow is diverted in the LUX circulation system. The injected ^{83m}Kr diffuses uniformly in the liquid xenon in a few minutes. ^{83m}Kr, that is a ^{83}Kr's meta-stable excited state, decays emitting a 32.1 keV and a 9.4 keV conversion electron with a half-life of 1.83 hours. Such a short half-life allows for quite frequent calibrations (more than one per week usually), as the activity of the source becomes negligible within hours. The full decay chain is described in the left panel of Fig. 3.26. Because the 9.4 keV decay has a half-life of only 154 ns, while the minimum $S1$ pulse separation in LUX is 10^3 ns, the two decays are merged into a combined 41.55 keV peak in LUX spectrum, as shown in the right panel of Fig. 3.26.

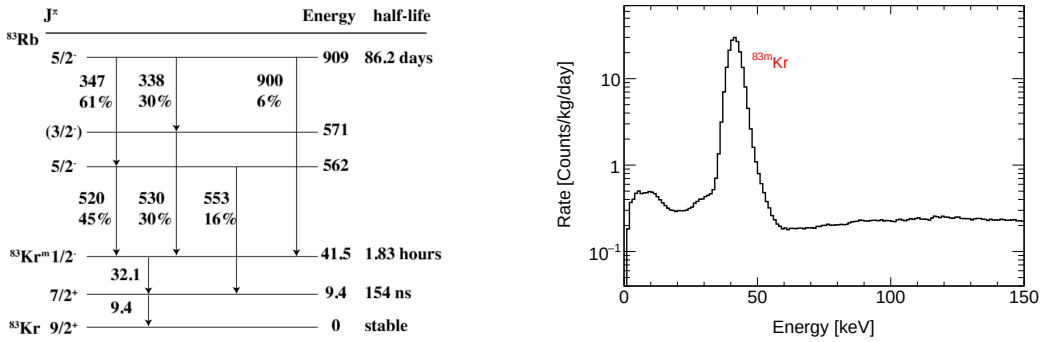

Figure 3.26 *Left panel: decay chain of ^{83}Rb, that 75% of the times decays to ^{83m}Kr. ^{83m}Kr decays further, in two steps, emitting a 32.1 keV and a 9.4 keV conversion electron. Energy is in units of keV, while units of time are indicated in the diagram [132]. Right panel: energy spectrum of LUX 2013 data having passed all the selection cuts (radial cut at 20 cm). The labelled peak due to ^{83m}Kr calibrations is centred at 41.55 keV, as the 154 ns time window between the two decays in cascade is smaller than the minimum S1 pulse separation in LUX.*

The second internal source employed in LUX is tritiated methane (CH3T), that is used as host molecule for tritium (^{3}H) [133]. Being a single-β emitter, tritium is an electron-recoil calibration source. The β spectrum of tritium has a broad peak at 2.5 keV$_{ee}$, a mean energy of 5.6 keV$_{ee}$, and an endpoint of 18.6 keV$_{ee}$. These characteristics make it suitable to explore the detector response in the region of interest of most LUX analyses. CH3T is mixed with purified xenon, that acts as carrier gas when the source is injected in the LUX circulation system to enter the detector. The diffusion time is then matter of minutes and the spatial distribution of the events is uniform, as in the case of ^{83m}Kr. While the activity of ^{83m}Kr becomes negligible quickly, tritium has a half-life of 12.3 years. Therefore, it has to be removed from the detector by using the LUX purification system, making tritium calibrations not as frequent as krypton ones. Two tritium calibrations happened in 2013, in August and December. The latter was the main one, performed when the science data taking was completed. A total activity of 10 Bq of tritium was employed, producing 3×10^5 events in the 250 kg active volume.

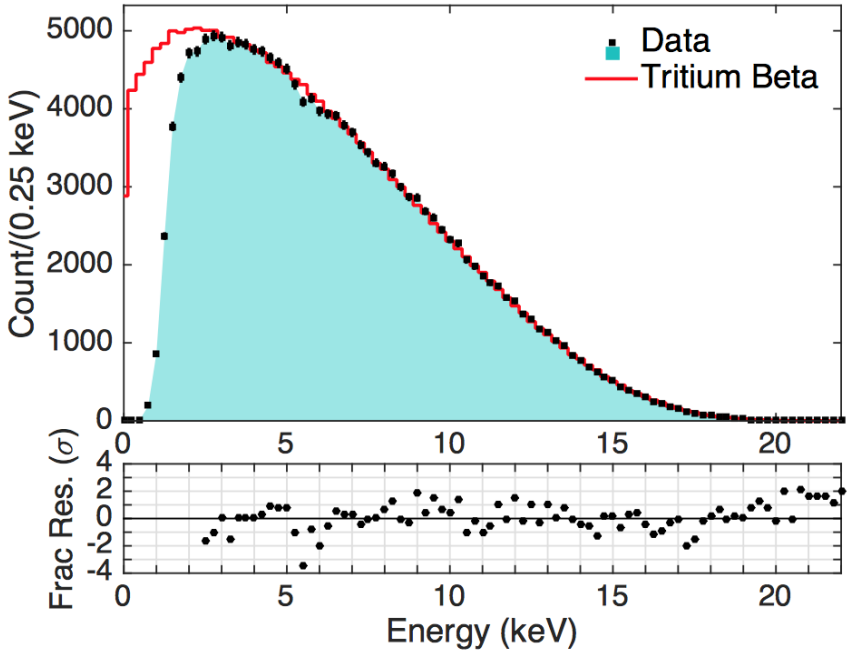

Figure 3.27 *Top: the tritium energy spectrum measured by LUX (black dots) compared to a true tritium spectrum convolved with the experimental resolution (red curve). Bottom: bin-by-bin fit residuals between data and theoretical expectation, in units of σ [133].*

The calibration spectrum has been reconstructed through the electron recoil

energy formula (Eq. 3.15). Figure 3.27 shows the data, fitted to a true tritium spectrum convolved with the experimental resolution. Details about such a resolution will be discussed later. Tritium calibration spectrum is also used to evaluate the efficiency curve for electron recoils, as will be discussed in Chapter 5, and to identify the electron recoil band, as shown in the left panel of Fig. 3.28.

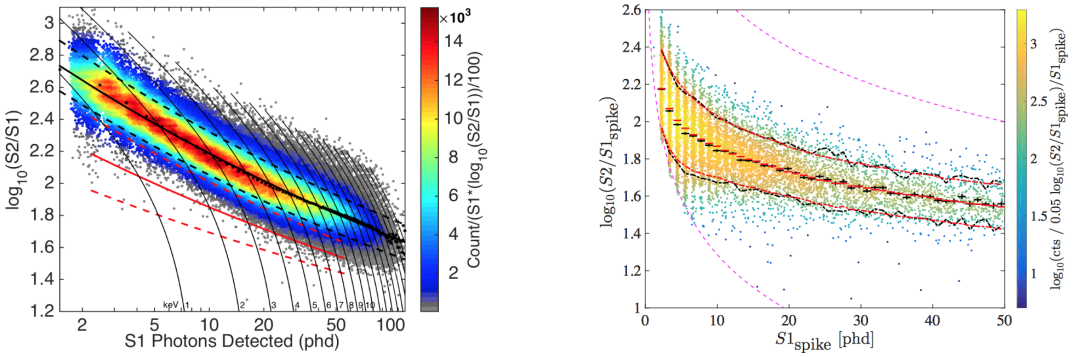

Figure 3.28 *Identification of electron recoil and nuclear recoil band in the* $\log_{10} S2$ *versus* $S1$ *phase space through calibrations. Left panel: tritium calibration data are distributed in the electron-recoil band, whose mean is indicated by the solid black curve. The solid red curve describes the mean of the nuclear-recoil band, as obtained with D-D neutron generator data [133]. Right panel: D-D calibration data are distributed in the nuclear-recoil band [127].*

As for the nuclear recoil band calibration, LUX employs a neutron beam produced by the D-D neutron generator [127] that has been described in the previous section. Such a generator is operated at a 5% duty cycle: 100 μs neutron pulses are used to produce mono-energetic 2.45 MeV neutrons, that scatter multiple times within the fiducial volume. The detector response to nuclear recoils can then be calibrated in the energy range from 0.7 to 24.2 keV_{nr}. D-D generator events are used to define the nuclear-recoil band, as shown in the right panel of Fig. 3.28.

3.4.3 The LUX signal yields and resolution

The experimental response of the LUX detector is determined by the signal yields, the gain factors, and the resolution. An analysis of mono-energetic peaks in the LUX electron-recoil search and calibration data has been performed to estimate such parameters [125]. An energy window from 5.2 keV to 661.7 keV has been covered, considering peaks due to both known background sources (^{127}Xe, ^{131m}Xe, ^{129m}Xe, ^{208}Tl, ^{214}Bi) and calibration sources (^{83m}Kr, ^{137}Cs).

From the reconstruction of the energy of these peaks through Eq. 3.15, the gain factors have been measured to be $g_1 = 0.117 \pm 0.003$ phd/photon and $g_2 = 12.1 \pm 0.8$ phd/electron, with an electron extraction efficiency of $49\% \pm 3\%$.

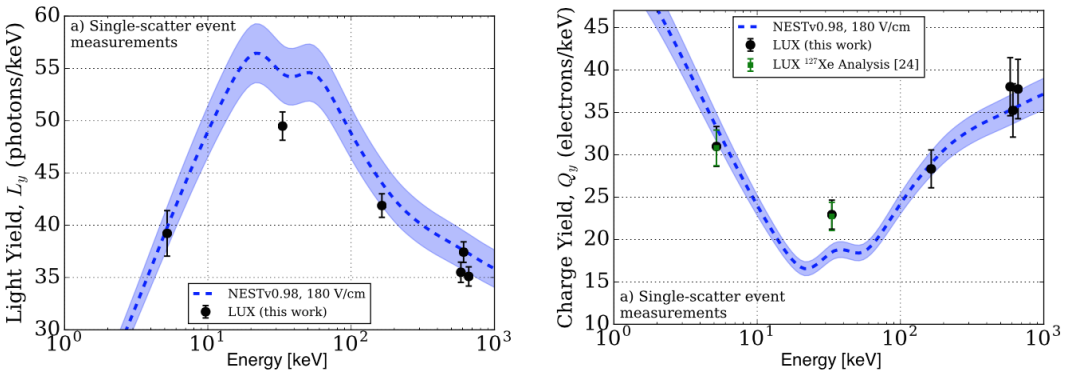

Figure 3.29 *The light (left panel) and charge (right panel) yield, measured at peak energies in the LUX background spectrum (black dots). The NEST prediction for an applied electric field of 180 V/cm (dashed blue curve) ± its 5% uncertainty (shaded blue band) is inserted for comparison [125].*

A fixed mean amount of light and charge is generated by the mono-energetic sources, thus the signal yields can be obtained by fitting the mean $S1$ and $S2$ response at each energy. Measured values of the light and charge yield are plotted as a function of energy in Fig. 3.29, in the left and right panel, respectively. For both yields, data points are superimposed with dashed blue curves representing NEST expectations. The Noble Element Simulation Technique (NEST) is a very accurate simulation tool, that provides models for scintillation and electroluminescence processes in noble elements, given the electric field [134, 135].

The mono-energetic sources can also be used to evaluate the LUX experimental resolution for electron recoils. Figure 3.30 shows the percent energy resolution as a function of energy for several sources. The six lowest energies have been fitted with an $a/\sqrt{E}$ function, returning a value of $a = (0.33 \pm 0.01)\ keV^{1/2}$. The function has been extrapolated at higher energies.

The description of the LUX detector, its operations, and calibrations is a prelude to Chapter 4, 5 and 6, where some of the analyses carried on LUX data will be described.

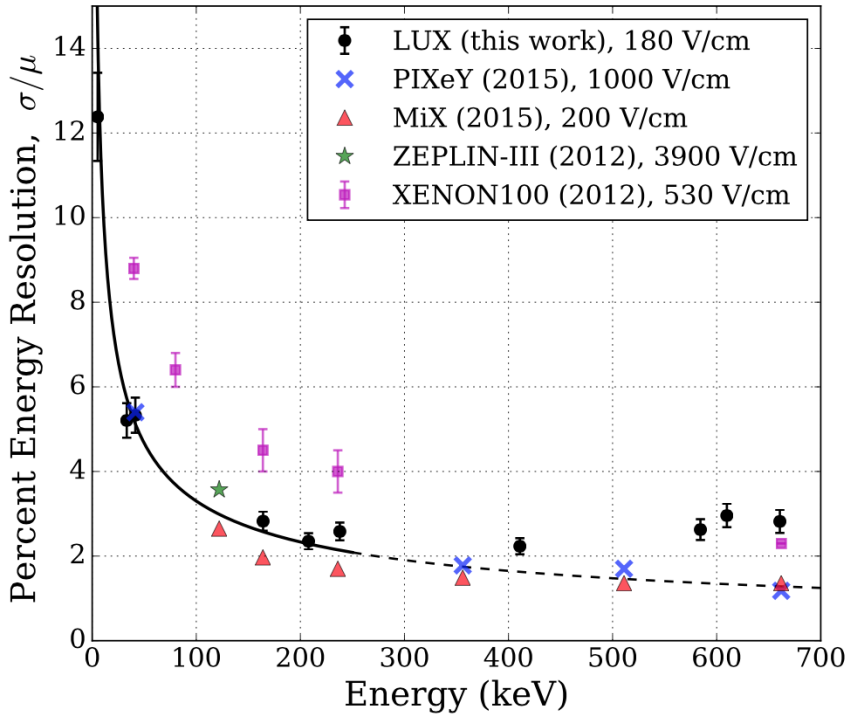

Figure 3.30 *The measured energy resolution at known energy peaks in the LUX electron-recoil spectrum. The fit (extrapolated) function is shown as the solid (dashed) black curve. Results from other experiments are inserted for comparison [125].*

Chapter 4

WIMP searches

Weakly interacting massive particles (WIMPs) stand out the landscape of possible candidates for dark matter given in Chapter 2, being the most widely accepted candidate for cold dark matter. WIMPs can be searched for via several different experimental approaches. WIMPs are expected to have been produced in the early universe, and to weakly interact with ordinary matter via elastic collisions – collisions that induce the recoil of the atomic nucleus. As described in Chapter 3, various experimental strategies try to identify events associated with dark matter-induced recoils, and dual-phase xenon TPCs are certainly some of the more sensitive.

This chapter is dedicated to WIMP searches that have been performed on LUX data. The analyses are included in this thesis for completeness, as they are not part of my original work, even though I have contributed to achieve some of the results.

After introducing the LUX simulation package, LUXSim, details are provided about the WIMP expected event rate, the model of background contributions, and the analysis approach. At the end of the chapter, we give a summary of nuclear-recoil band searches and results delivered by LUX, before moving onto the chapters focusing on electron-recoil band searches.

4.1 LUXSim: a LUX-dedicated simulation package

The simulation of events happening in the detector has always played a central role in nuclear and particle physics, and LUX is not an exception. For this reason the presentation of the LUX simulation package opens the series of chapters dedicated to LUX analyses and results.

Based on the major simulation tool available for physics studies, Geant4, LUXSim is dedicated to low-background physics. The main purpose of this package is to focus on multiple radioactive sources emitting at once, rather than on a single source or beam fired towards the detector [136]. LUXSim allows the user to take a component-centred approach, as in simulating any number of sources within any number of detector components at a time. This procedure is possible thanks to dedicated classes for source generation and a detailed description of detector geometry. The output of LUXSim contains a complete description of physics processes of interest.

The LUXSim package features a reconstruction of the full LUX detector based on CAD designs. Any physical volume is recognised as a class, whose record level can be set by the user according to the necessary amount of detail. Physical volumes can be associated with any radioactive source, whose activity level can be indicated and is used to weight each contribution appropriately. Taking the form of generators, sources are LUXSim classes. Specific values of particle type, energy, direction and activity can be given to the generator. Moreover, each source can be associated to one or multiple detector components, within the same run, allowing for a complete output record.

The liquid xenon is treated as any other LUX component, so that the use of LUXSim is not only restricted to simulations of backgrounds generated in the structure of the detector or coming from the outside, but can be also used to reproduce processes happening inside the target. Examples of this are xenon radioactive isotopes decays, contributing as additional background sources, and potential signal interactions due to any candidate of interest.

Simulations of both background and signal contributions are fundamental to the LUX analysis framework. In the next sections, and in Chapter 5 and 6, examples of the use of LUXSim will be given.

4.2 WIMPs signal model

An interpretation of the theoretical spectrum describing any expected signal is required in order to build the corresponding signal model. The use of LUXSim and NEST (c.f. Chapter 3) allows for this. The modelling of the signal induced by WIMP interactions in LUX is described in this section.

The energy spectrum of WIMP-induced recoils of target nuclei is expected to be smoothly decreasing. The interaction rate varies with the recoil energy as [137]:

$$\frac{dR}{dE_n} = \frac{R_0}{E_0 r} e^{-E_n/E_0 r}, \tag{4.1}$$

where R is the event rate per unit mass, E_n is the recoil energy, R_0 is the total event rate, E_0 is the most likely kinetic energy for an incident WIMP, and r is a kinematic factor. For a WIMP of mass M_χ and a target nucleus of mass M_N, $r = 4M_\chi M_N/(M_\chi + M_N)^2$. Dark matter experiments aim at the highest rate possible. This can be generally achieved via background reduction, and by minimising r with the choice of a high mass target nucleus.

Dark matter experiments measure (or constrain) the differential rate on the left hand side of Eq. 4.1. The signal rate, R_0, can be evaluated (or constrained) based on the result, for each given value of WIMP mass. The common approach is then to convert the limit on the total event rate to a limit on the cross section of the interaction. Indeed, given a velocity distribution for dark matter particles, the differential rate can be expressed in terms of interaction probability. This procedure is what is used to build the signal model for WIMPs in LUX, as well as in many other dark matter search experiments.

4.2.1 Velocity distribution

As introduced in Chapter 2, WIMPs are expected to be a primordial relic. They are thus expected to move with some velocity distribution within the galaxy. The usual assumption is for dark matter to have a Maxwellian velocity distribution:

$$f(\mathbf{v}, \mathbf{v}_E) = e^{-(\mathbf{v}+\mathbf{v}_E)^2/v_0^2}, \tag{4.2}$$

where $\mathbf{v}$ is the dark matter velocity onto the target, $\mathbf{v}_E$ is the velocity of Earth with respect to the dark matter halo, and v_0 is the galactic rotation velocity.

The mean dark matter particle number density can be expressed as $n_0 = \rho_\chi / M_\chi$, where ρ_χ is the dark matter particle density and M_χ is its mass. The integral of the differential dark matter particle density, dn, over velocities from 0 to the local galactic escape velocity, v_{esc}, has to be equal to n_0. Such a condition is ensured by the normalisation factor, k, that enters the expression of the differential dark matter particle density [137]:

$$dn = \frac{n_0}{k}\ f(\mathbf{v}, \mathbf{v}_E)\ d^3v, \tag{4.3}$$

that is the density of dark matter particles with relative velocities within d^3v about $\mathbf{v}$. In the limit $v_{esc} \to \infty$, $k \to k_0 = (\pi v_0^2)^{3/2}$.

Estimates for the parameters defining the velocity distribution come from astrophysics. According to the canonical halo model, dark matter is an isothermal spherical distribution that behaves as a non-interacting ideal gas. The WIMP velocity relative to the galactic centre can be well approximated by the orbital velocity at a given radius: at the Sun location (≈ 8.3 kpc), $v_0 = 220$ km/s [138]. In LUX analyses, we also assume $v_{esc} = 544$ km/s, $\rho_\chi = 0.3$ GeV/cm^3, and an average Earth velocity of 245 km/s [139].

4.2.2 Event rate

Given Eq. 4.3, the event rate per unit mass on a target, dR, can be expressed in terms of cross section per nucleus, σ [137]:

$$dR = \frac{N_A}{A}\ \sigma\ v\ dn, \tag{4.4}$$

where N_A is the Avogadro constant, and A is the atomic mass of the target. The event rate in Eq. 4.4 can be also written as:

$$dR = R_0\ \frac{k_0}{k}\ \frac{1}{2\pi v_0^4}\ v\ f(\mathbf{v}, \mathbf{v}_E)\ d^3v, \tag{4.5}$$

with $R_0 = \frac{2}{\sqrt{\pi}} \frac{N_A}{A} n_0 \sigma_0 v_0$, where σ_0 is the zero-momentum transfer cross section.

The interaction rate varies with the recoil energy, as expressed in Eq. 4.6 in terms of dark matter velocity distribution [137]:

$$\frac{dR}{dE_n} = \frac{R_0}{E_0 r} \frac{k_0}{k} \frac{1}{2\pi v_0^2} \int_{v_{min}}^{v_{max}} \frac{f(\mathbf{v}, \mathbf{v}_E)}{v} d^3v. \tag{4.6}$$

This expression approximates to Eq. 4.1 when $\mathbf{v}_E = 0$ and $v_{esc} \to \infty$.

As introduced at the beginning of this section, the experimental parameter of interest in WIMP searches is the cross section. The zero-momentum transfer cross section, also known as "total cross section", σ_0, accounts for the nature of the WIMP-nucleus interaction, as in whether such an interaction is spin-independent (SI) or spin-dependent (SD). For SI interactions [140]:

$$\sigma_0^{SI} = \frac{4}{\pi} \mu^2 [Z f_p + (A - Z) f_n]^2, \tag{4.7}$$

where $\mu \equiv M_\chi M_N / (M_\chi + M_N)$ is the reduced mass, Z and A are, respectively, the atomic number and mass of the target nucleus, while $f_{p,n}$ are the effective scalar couplings of WIMPs to protons/neutrons. In the approximation $f_p \simeq f_n$, Eq. 4.7 can be rewritten as:

$$\sigma_0^{SI} \simeq \frac{4}{\pi} \mu^2 A^2 |f_p|^2. \tag{4.8}$$

In the SD case, when WIMPs couple to the spin of the target nucleus, the cross section reads [140]:

$$\sigma_0^{SD} = \frac{32}{\pi} G_F^2 \mu^2 \left(\frac{J+1}{J} \right) [\langle S_p \rangle a_p + \langle S_n \rangle a_n]^2, \tag{4.9}$$

where G_F is the Fermi constant, μ is the reduced mass, J is the total spin of the target nucleus, $\langle S_{p,n} \rangle$ are the expectation values of proton and neutron spin, and $a_{p,n}$ are the effective couplings to protons/neutrons.

The use of the total cross section in the calculation of the event rate is an approximation only valid if the wavelength, h/q, is larger than the nuclear

radius, r_n, given a momentum transfer $q = \sqrt{2M_N E_n}$. Such an assumption means that the WIMP is considered as interacting with the entire nucleus. When this condition is no longer valid though, as q increases, the effective cross section, σ, decreases. Given σ_0, the dependence of the cross section on the momentum transfer and on the radius of the target nucleus can be expressed in terms of the so called "form factor", $F(qr_n)$, that accounts for coherence loss [137]:

$$\sigma(qr_n) = \sigma_0 \; F^2(qr_n). \tag{4.10}$$

The form factor is a function of the quantity qr_n, that is dimensionless if q is measured in MeV/c and r_n in fm.

The form factor also accounts for the SI or SD nature of the WIMP-nucleus interaction. For SI interactions, it is believed to behave as proposed by Helm [141]:

$$F_{SI}(qr_n) = 3 \; \frac{j_1(qr_n)}{(qr_n)} \; e^{-(qs)^2/2}, \tag{4.11}$$

where j_1 is the spherical Bessel function, and s measures the nuclear skin thickness. Although for SD interactions the form factor depends on the nucleus and an analytic expression such as Eq. 4.11 does not exist, Lewin and Smith introduced an approximation based on the value of the parameter qr_n [137]:

$$F^2_{SD}(qr_n) = \begin{cases} j_0^2(qr_n) & \text{if } qr_n < 2.55 \text{ or } qr_n > 4.5 \\ \sim 0.047 & \text{if } 2.55 < qr_n < 4.5 \end{cases} \tag{4.12}$$

where $r_n \simeq 1.0A^{1/3}$ fm.

Given the theoretical event rate for WIMP interactions, the expected experimental energy spectrum can be constructed, taking into account detector effects such as resolution and efficiency.

4.2.3 Signal model

A WIMP interaction signal in liquid xenon would result in a nuclear recoil. To simulate the energy deposition due to a WIMP-induced event in LUX, LUXSim has been used. The efficiency for nuclear-recoil event detection in LUX is shown

in Fig. 4.1, and is employed in the production of the signal model.

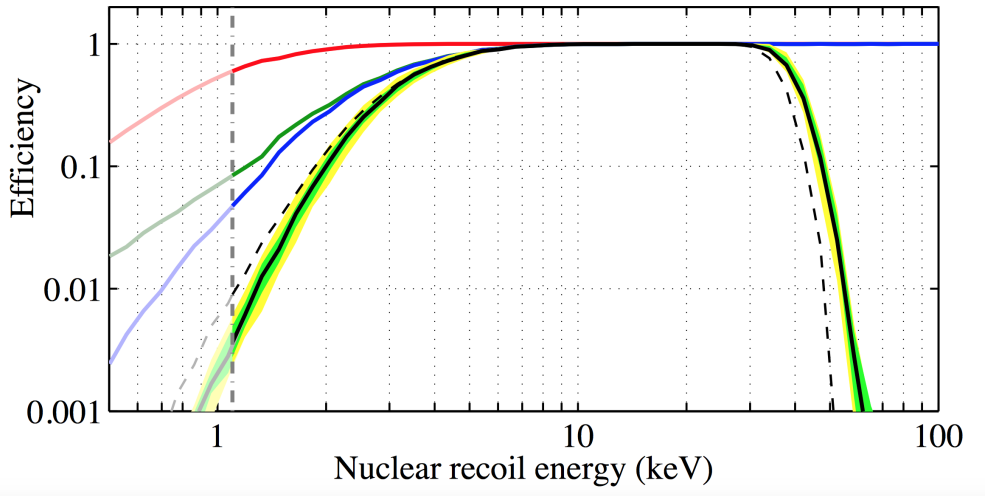

Figure 4.1 *Efficiencies for NR event detection, estimated by using LUXSim and inputs from the DD calibration. In descending order of efficiency: detection of an S2 (red), detection of an S1 (green), detection of both an S1 and an S2 (blue), detection passing thresholds in S1 and raw S2 size. The vertical dashed line indicates that the signal model is cut off at 1.1 keV [131].*

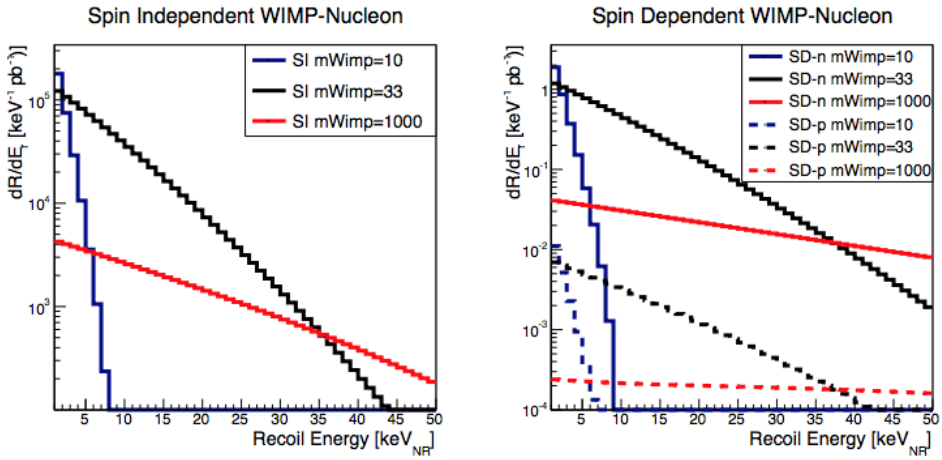

Figure 4.2 *WIMP interaction rates for $M_\chi = 10$ GeV (blue), 33 GeV (black), and 1 TeV (red). Left panel: SI WIMP-nucleon interaction differential rate. Right panel: SD WIMP-neutron (solid) and WIMP-proton (dashed) interaction rate.*

As described in Chapter 3, the NEST tool translates theoretical event rates to LUX-specific experimental quantities, by providing a very accurate simulation of both scintillation and electroluminescence in liquid xenon. In this way, $S1$ and $S2$ values corresponding to the true deposited energy can be extracted, and the nuclear recoil energy scale (keV_{NR}) can be built.

Figure 4.2 shows differential event rates for both SI and SD interactions, taking three WIMP masses as examples. The rate decreases at high recoil energies and is steeper the lighter is the candidate mass (c.f. Eq. 4.1). The event rate can then be translated to a probability density function in a four dimensional phase space, that is identified by the most informative experimental quantities: the prompt scintillation signal ($S1$), the base 10 logarithm of the proportional ($S2$) signal, and the radial (r) and vertical (z) position of the event location within the LUX detector.

4.3 Background model

To make the nuclear recoil spectrum from WIMP interactions detectable, experimental efforts focus on reducing the background rate. As already discussed, approaches to achieve this may vary. The strategy adopted in LUX relies on the selection of clean construction materials, the operation of the detector deep underground, and the choice of an experimental approach to discriminate between nuclear and electron recoils. Following these guidelines, the LUX goal is to maintain background expectation to < 1 WIMP-like background event in 30,000 kg days [105].

In Chapter 3 we have presented the background sources that are expected in LUX. Contributions come from γ rays and neutrons from construction materials, cosmogenically activated xenon isotopes, liquid xenon contaminants such as radon and krypton, and external backgrounds generated by cavern rocks and muons approaching the Earth.

Using the LUXSim simulation tool introduced at the beginning of this chapter, each of the contributions has been simulated to build the background model. LUXSim generators take the activity of the source as an input. Measurements of LUX data, as well as sampling of the liquid xenon target and screening of detector components (c.f. Fig. 3.18), have been used to determine the expected activity [130]. Simulated background events are subject to the WIMP search data quality cuts discussed in Chapter 3, and then used to build probability density functions for both electron and nuclear recoil events. These distributions have the same four dimensions as the signal model. Plots of the background model are not inserted in this section, but will be found in Chapter 5.

4.4 Analyses and results

As this chapter is for completeness only, many details about the analysis technique are not provided. They will be fully discussed in Chapter 5, that is dedicated to the original work this thesis is focused on. Although WIMP searches and axion searches differ with respect to the recoil band where the signal is expected, the statistical approach is the same, for consistency.

WIMP searches in LUX aim at testing the signal model for spin-independent and spin-dependent interactions against LUX data. If no evidence for signal can be found, a statistical limit on the cross section of the interaction is set. LUX has taken data since 2013, delivering two series of publications. The first results have been delivered based on 2013 data only. Final LUX results have been obtained with the analysis of the full exposure, adding up the data collected between 2014 and 2016.

4.4.1 Analysis strategy

The statistical approach chosen in LUX is a Profile Likelihood Ratio (PLR) analysis [142]. Chapter 5 will treat the optimisation of the PLR for electron-recoil band searches, while the results presented in this section rely on the standard PLR for WIMP searches. The four-dimensional probability density functions representing the signal and the background model are scaled by the expected number of counts of each component. The signal acceptance efficiency is also taken into account when constructing the signal model.

Uncertainties on variables such as the scaling factors and the efficiency are incorporated by treating them as "nuisance parameters". Such parameters are constrained to a mean value with a Gaussian standard deviation, and can be varied to find the best fit to the data. In LUX WIMP searches, the rates of the background components, the proportionality constant of the Lindhard factor, k (c.f. Eq. 3.7), and the $S2$ gain ratio, $g_{2,DD}/g_{2,WS}$ [1], are treated as nuisance parameters. Figure 4.3 gives an example of best fit to the 2013 LUX data, taken from the SI WIMP search analysis. A complete description of the background contributions is reported in Chapter 5.

[1]The $S2$ gain ratio is defined as the $S2$ gain during D-D calibration in November 2013 relative to the WIMP search.

Parameter	Constraint	Fit value
Lindhard k	0.174 ± 0.006	$\cdots$
S2 gain ratio: $g_{2,\mathrm{DD}}/g_{2,\mathrm{ws}}$	0.94 ± 0.04	$\cdots$
Low-z-origin γ counts: $\mu_{\gamma,\mathrm{bottom}}$	172 ± 74	165 ± 16
Other γ counts: $\mu_{\gamma,\mathrm{rest}}$	247 ± 106	228 ± 19
β counts: μ_{β}	55 ± 22	84 ± 15
^{127}Xe counts: $\mu_{\mathrm{Xe\text{-}127}}$	91 ± 27	78 ± 12
^{37}Ar counts: $\mu_{\mathrm{Ar\text{-}37}}$	$\cdots$	12 ± 8
Wall counts: μ_{wall}	24 ± 7	22 ± 4

Figure 4.3 *Nuisance parameters in the SI WIMP search global best fit to 2013 LUX data. Constraints are Gaussian with means and standard deviations indicated. Event counts are after analysis cuts [131].*

The PLR allows for testing two alternative hypotheses against a data set. One represents a background-only description of the data, with the interaction cross section set to zero, while the other includes a signal component. For each WIMP mass, fixed non-zero values of the cross section are tested, and the PLR is used to find the best fit to the data set by varying the nuisance parameters within the given uncertainties.

The maximum likelihood value of the cross section has been found to be zero in all the analyses performed on LUX data. Being found no evidence for either SI or SD WIMP interactions, LUX delivered several best limits on WIMP interaction cross sections, that have been published in Physics Review Letters.

4.4.2 Spin-independent results

The first LUX result has been delivered in 2016. Testing WIMP interactions in the data collected in 2013, the most stringent direct limits on the spin-independent WIMP-nucleon cross section have been obtained.

The background-only model gives a good fit to the data, with KS test p values of 0.05, 0.07, 0.34, and 0.64 for the projected distributions in $S1$, $S2$, r, and z respectively [2]. Upper limits on the cross section for WIMP masses within 4 and 1000 GeV/c^2 are shown in Fig. 4.4, and present a minimum of 0.6 zb at 33 GeV/c^2 WIMP mass [131].

[2]Details on the Kolmogorov-Smirnow (KS) test will be given in Chapter 5.

The LUX data taking ended in 2016, and data collected between 2014 and 2016 were summed up to 2013 data to present a complete analysis, leading to a joint publication [143]. The analysis of the 2014-2016 data required several additional actions with respect to the previous data set. Data have been categorised according to a model of the LUX electric field, to take into account a non-uniform and time-varying negative charge density in the PTFE panels that define the radial boundary of the active volume. The LUX detector has been treated as 16 time- and position-dependent detectors. Moreover, starting in December 2014, a protocol for blinding the data to potential nuclear-recoil WIMP signals has been followed. Artificial WIMP-like events are created and inserted within the fiducial volume, and only removed once data selection criteria, efficiencies, and PLR models have been defined.

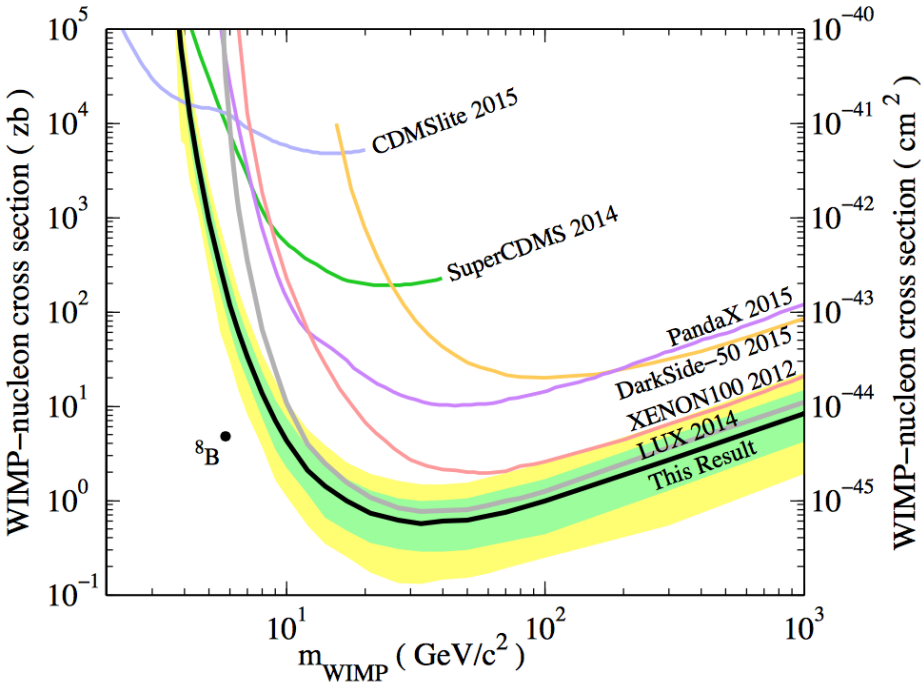

Figure 4.4 *Upper limits on the SI WIMP-nucleon cross section at 90% C.L. from the analysis of LUX 2013 data. Observed limit (black curve), with ± 1 σ (green band), and ± 2 σ (yellow band) regions. Results from other experiments are also included, as published in 2016 in Ref. [131].*

The background-only hypothesis gives the best fit to the data, with KS test values $p > 0.6$ for each of the projected distributions in the observables. At 50 GeV/c^2 WIMP mass, WIMP-nucleon spin-independent cross sections above 1.1×10^{-46} cm^2 are excluded at the 90% C.L., as shown in Fig. 4.5.

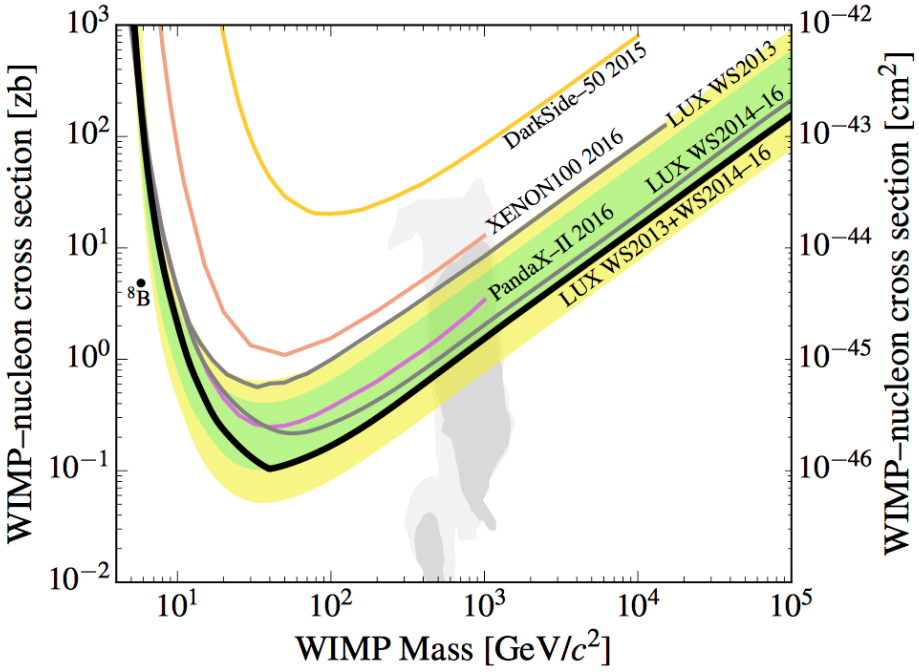

Figure 4.5 *Upper limits on the SI WIMP-nucleon cross section at 90% C.L. from the analysis of the full LUX exposure. Observed limit (black curve), with ± 1 σ (green band), and ± 2 σ (yellow band) regions. Results from other experiments, as well as previous LUX results, are also included, as published in 2017 in Ref. [143].*

4.4.3 Spin-dependent results

First LUX constraints on the spin-dependent WIMP-nucleon elastic cross sections have been obtained from data acquired in 2013. A PLR analysis has been used to set 90% C.L. upper limits on both the WIMP-neutron, σ_n, and WIMP-proton, σ_p, cross section, as shown in Fig. 4.6. At 33 GeV/c^2, values of σ_n above 9.4 × 10^{-41} cm^2, and values of σ_p above 2.9 × 10^{-39} cm^2 are excluded at 90% C.L. The limit on σ_n is the most sensitive constraint to date [144].

The SD analysis has been repeated on the full LUX exposure, delivering the results shown in Fig. 4.7. At 35 GeV/c^2, values of σ_n above 1.6 × 10^{-41} cm^2, and values of σ_p above 5.0 × 10^{-40} cm^2 are excluded at 90% C.L. Also in this case, the spin-dependent WIMP-neutron limit is the most sensitive constraint to date [145].

In both cases, PICO is more sensitive to proton-only coupling, due to the combined impact of unpaired proton of the fluorine nuclei in the C_3F_8 target and the mass of target used.

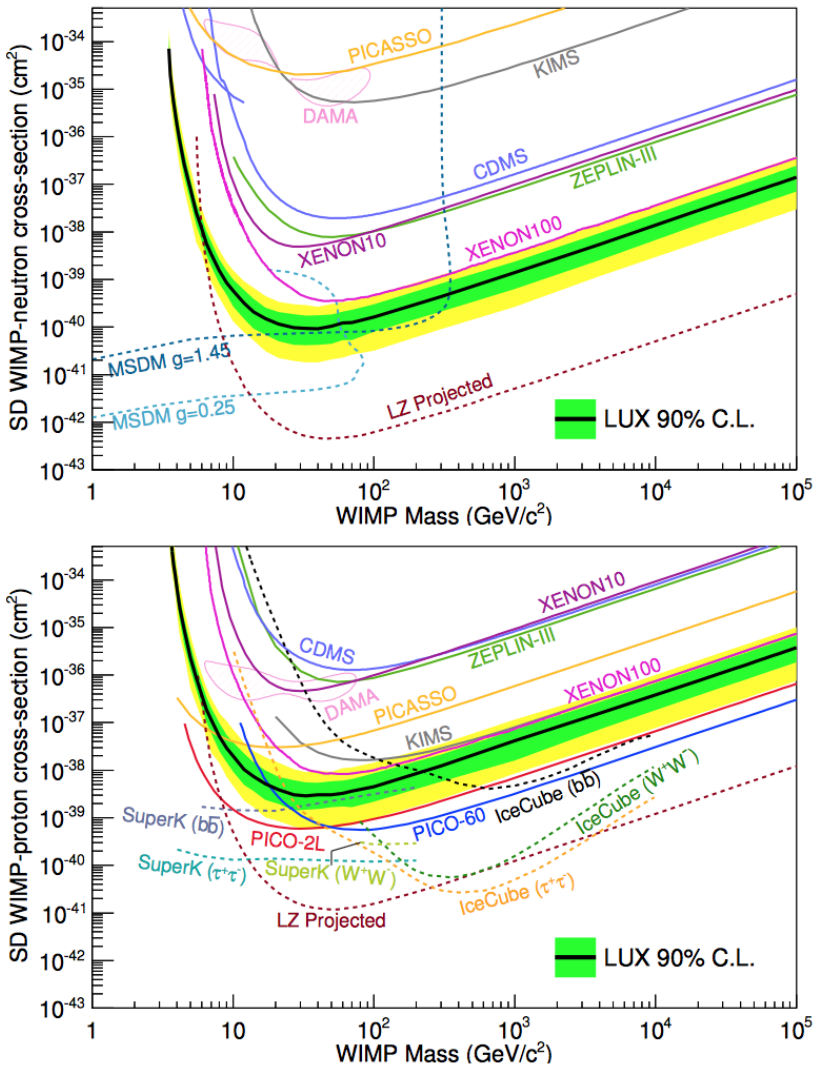

Figure 4.6 *Upper limits on the WIMP-neutron (top) and -proton (bottom) elastic SD cross sections at 90% C.L., as obtained from the analysis of LUX 2013 data. Observed limit (black curve), with ± 1 σ (green band), and ± 2 σ (yellow band) regions. Results from other experiments are also included, as published in 2016 in Ref. [144].*

WIMP searches in LUX take advantage of the discrimination between nuclear and electron recoils that is typical of TPCs. While the WIMP signal is expected as an excess of nuclear-recoil events, most of the background contribute as electron recoils. Nevertheless, electron-recoil band searches can also be performed in such a detector, allowing for the test of other dark matter candidates, as well as phenomena of more general interest in particle physics.

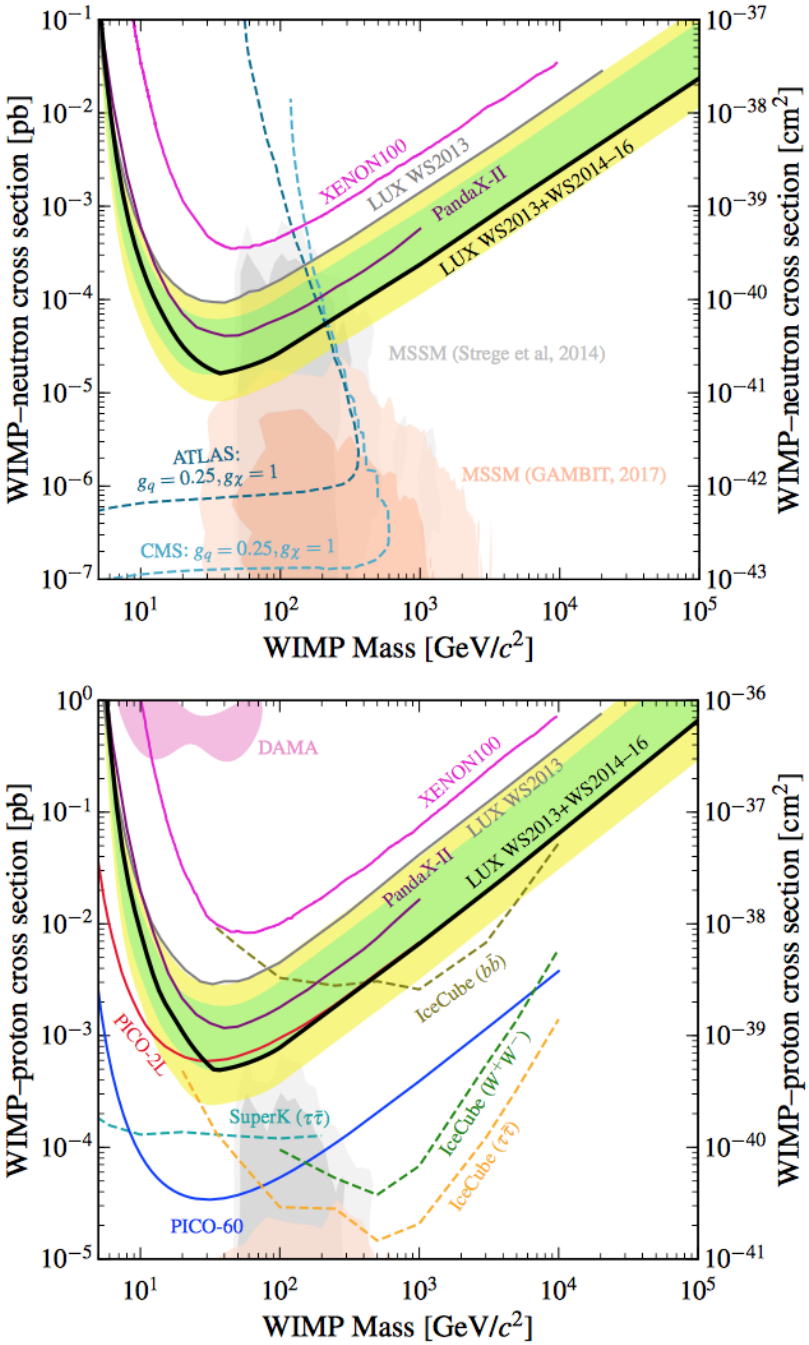

Figure 4.7 *Upper limits on the WIMP-neutron (top) and -proton (bottom) elastic SD cross sections at 90% C.L., as obtained from the analysis of the full LUX exposure. Observed limit (black curve), with ± 1 σ (green band), and ± 2 σ (yellow band) regions. Results from other experiments, as well as previous LUX results, are also included, as published in 2017 in Ref. [145].*

Chapter 5

Axion and axion-like particle searches

Beside the mainstream analyses described in the previous chapter, a device such as LUX can also be employed in other kind of searches. We have previously introduced that the scenario for investigation on dark matter and physics beyond the Standard Model is much wider than WIMPs, with a first example being the axions and the axion-like particles (ALPs).

Data collected in 2013, with an exposure totalling 95 live days $\times$ 118 kg, have been analysed to search for a signal induced by these candidates in the LUX detector. The best limits to date on the coupling constant between axions or ALPs and electrons have been delivered. This chapter presents a detailed description of the analyses underpinning the results published in Physics Review Letters in 2017 [146].

Following the structure of Chapter 4, the production of the signal models to be tested opens the chapter. The background model used to describe the expected background, and the details of the chosen statistical approach are presented, followed by the obtained results.

Looking at the future, we also show sensitivity projections for axion and ALP studies with the next generation experiment that will take LUX's place in the same experimental site, the LUX-ZEPLIN (LZ) detector. As compared with the LUX results, LZ sensitivity projections are such that it would rule out a much wider region of the interesting phase space, or make a detection, thanks to the

larger exposure and the improvements made to reduce the background rate. A look at the big picture closes the chapter by giving an overview on other axion searches and inserting LUX in a wider context.

5.1 Signal models

Interactions happening in LUX can be discriminated against their nature, as in inducing electron or nuclear recoils. For this purpose, data can be organised in a $\log_{10} S2$ versus $S1$ discrimination phase space. It is crucial to underline that axion or ALP interactions would result in additional events within the electron-recoil band of the phase space, rather than in the nuclear-recoil band as for WIMP candidates. This is related to the axion and ALP interactions LUX is able to probe.

In the analyses described in this chapter, two signal sources are considered, axions produced and emitted from the Sun, and primordial ALPs slowly moving within the Galaxy. Both are expected to give a signal in the electron-recoil band and, for both of them, the detection principle relies on the so-called "axio-electric effect". As the axions are produced and emitted from the Sun, in the case of the axion signal model, the solar axion flux plays an important role as well.

To produce a signal model, we take the expected energy spectrum, and we turn it to an expected LUX experimental energy spectrum, by introducing effects such as the detection resolution and efficiency. Even if the spectrum on the energy scale is already informative, we translate it to a probability density function (PDF), that is a probability distribution of the signal events, living in a multi-dimensional phase space. Such a phase space is chosen to optimise the signal discovery potential, as having multiple physical variables to discriminate against makes it easier to distinguish between signal and background.

5.1.1 The axio-electric effect

Axions and ALPs were introduced in Chapter 2, and were described as potentially coupling with photons, electrons, or nucleons. When using a xenon active target such as LUX, only the coupling with the electrons can be tested, relying on the axio-electric effect [147–149].

A sketch and a very schematic Feynman diagram of the axio-electric effect are presented in Fig. 5.1, showing that the features of such an interaction make it similar to the photoelectric effect. An axion of mass m_a is absorbed by a bound electron which is then ejected from the atom, with a kinetic energy equal to the axion mass minus the atomic binding energy.

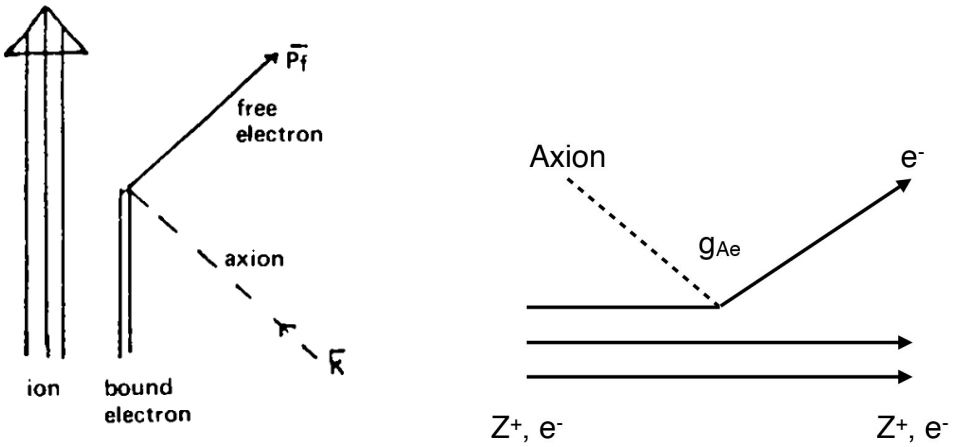

Figure 5.1 *The axio-electric effect: a sketch (left) [147] and a schematic Feynman diagram (right).*

The cross section for the axio-electric effect is given by [147, 148]:

$$\sigma_{Ae} = \sigma_{pe}(E_A)\frac{g_{Ae}^2}{\beta_A}\frac{3E_A^2}{16\pi\alpha_{em}m_e^2}\left(1-\frac{\beta_A^{2/3}}{3}\right), \tag{5.1}$$

where $\sigma_{pe}(E_A)$ is the photoelectric cross section on the target material, g_{Ae} is the coupling constant between axion or ALP and electron, α_{em} is the fine-structure constant, m_e is the mass of the electron, and β_A and E_A are the velocity and the energy of the axion. For a chosen target material, the axio-electric cross section is proportional to the photoelectric cross section, via a factor describing the axion kinematics and the coupling constant squared (c.f. Eq. 5.1). As g_{Ae} is the only unknown parameter in the formula, the purpose of axion searches is to measure its value. This would be possible only in the case of a discovery. Otherwise, if no evidence for signal is found, g_{Ae} can be constrained, and the phase space of allowed values can be reduced.

Assuming an arbitrary value for the coupling constant, in this case $g_{Ae} = 10^{-12}$, the axio-electric cross section can be plotted as a function of the energy of the axion, as shown in Fig. 5.2. The discontinuous trend reflects the atomic energy levels and the internal structure of the target material, and drives the shape of

the expected event rate for both solar axions and galactic axion-like particles.

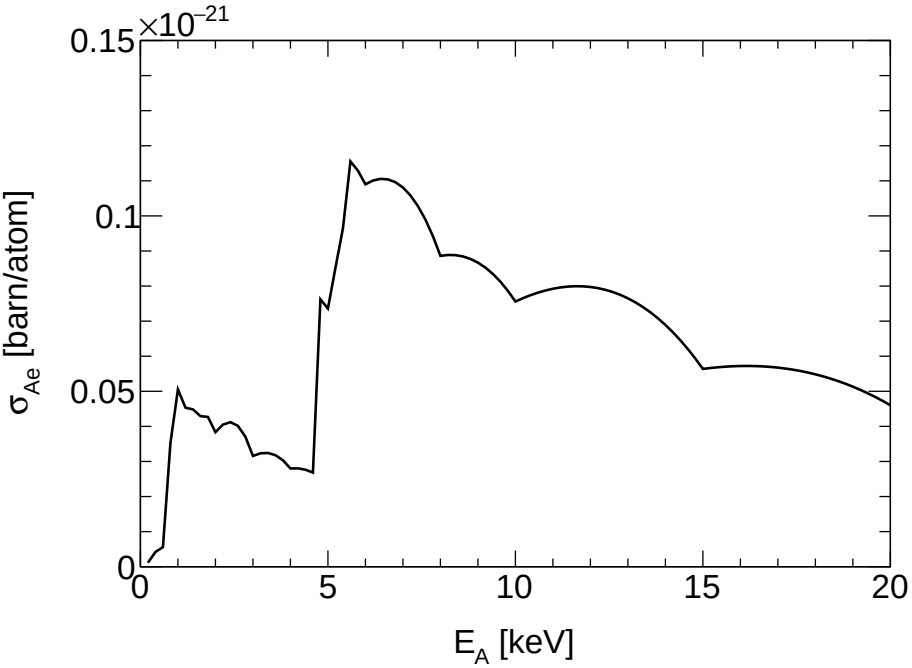

Figure 5.2 *The cross section for the axio-electric effect on xenon, as a function of the energy of the axion (c.f. Eq. 5.1). The discontinuous trend reflects the atomic energy levels and the internal structure of the target material. A value of $g_{Ae} = 10^{-12}$ has been assumed to obtain this plot.*

5.1.2 Axions

Given the axio-electric cross section, the signal model for axions produced and emitted by the Sun can be obtained by taking into account the flux of axions coming from the Sun through the Earth – flux that has been estimated by Javier Redondo [60].

Calculations have been made to describe the axion production reactions, that might be driven by both the axion-electron and the axion-photon coupling, as discussed in Chapter 2. The coupling with electrons is leading to different processes: the dominant contributions to the overall flux are from atomic axio-recombination and axio-deexcitation, axio-bremsstrahlung, and Compton scattering. According to the KSVZ axion model, the leading coupling is the one between axion and photon. This interaction drives the so-called Primakoff production mechanism, responsible of the Primakoff flux [68]. Examples of

Feynman diagrams for all these reactions were shown in Fig. 2.2.

Redondo estimated the flux assuming the solar axion to be massless, however, the flux, as estimated for zero axion mass, is still valid without heavy corrections for masses smaller than 1 keV/c^2 since the total energy is dominated by the kinetic energy. In the following analysis, the solar axion is approximated to be massless because of this theoretical limitation. Nevertheless, under this assumption, the search still covers theoretically interesting phase space, including the region for which axions provide a solution to the strong CP violation problem (c.f. Chapter 2).

The flux of solar axions due to the axion-electron coupling driven processes is shown in Fig 5.3 as a solid black curve. The atomic recombination and deexcitation introduce features associated with atomic shell structure, while the bremsstrahlung and Compton scattering contribute smoothly to the overall shape.

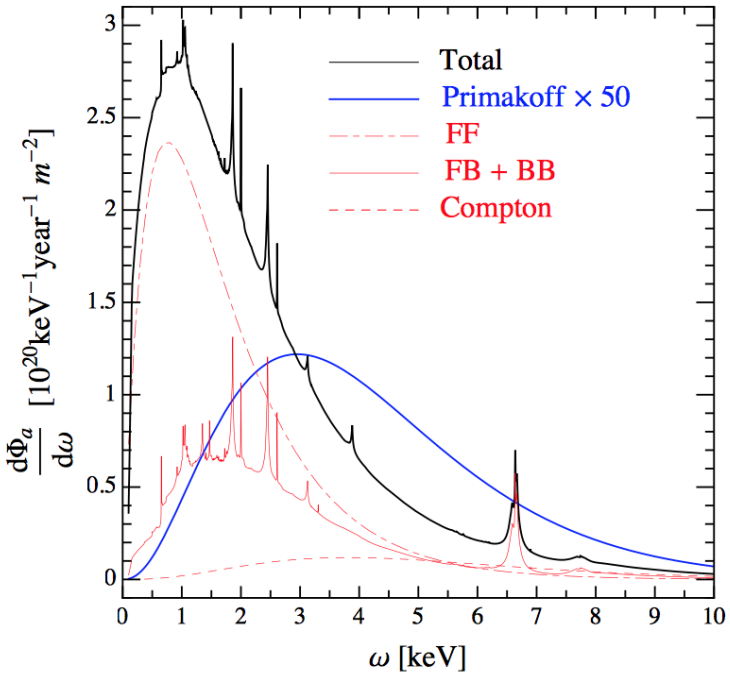

Figure 5.3 *The flux of solar axions due to the axion-electron coupling driven processes, as presented in Ref. [60], for an arbitrary value of the coupling ($g_{Ae} = 10^{-13}$). The total flux is the solid black line, while the different contributions are drawn as red lines: atomic recombination and deexcitation (solid, FB+BB), bremsstrahlung (dot-dashed, FF), Compton (dashed). The Primakoff flux × 50 is the solid blue line, included for comparison only.*

The expected energy spectrum from a massless solar axion is obtained by

multiplying the axio-electric cross section (Eq. 5.1) by the total solar axion flux, resulting in the dashed blue line in Fig. 5.4. The event rate for solar axions is directly proportional to the fourth power of the coupling, as both the axio-electric cross section and the solar axion flux carry a g_{Ae}^2 factor. Such a spectrum represents the theoretical input to the analysis and will be modified by detector resolution and efficiency effects, resulting in the expected LUX experimental spectrum, presented as the solid red distribution in Fig. 5.4.

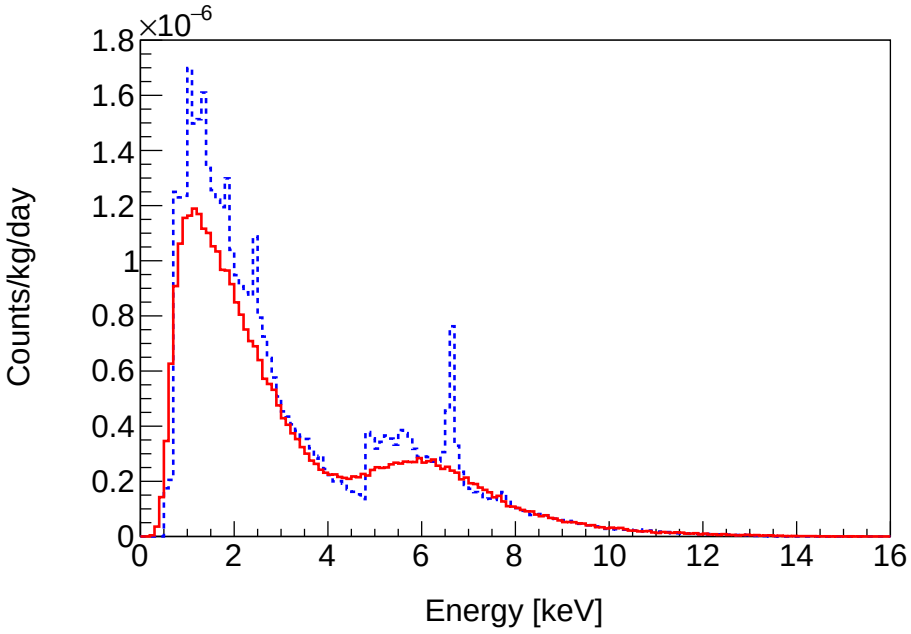

Figure 5.4 *Solar axion energy spectrum. Dashed blue distribution: expected energy spectrum from a massless solar axion, assuming a coupling $g_{Ae} = 10^{-12}$. The shape arises from a continuous contribution to the axion flux due to bremsstrahlung and Compton scattering, together with features associated with atomic recombination and deexcitation reactions. Solid red distribution: the expected LUX experimental solar axion energy spectrum, as modelled with NEST [134, 135, 150].*

As described in Chapter 3, the electron-recoil band has been calibrated with a tritium source. This calibration (Fig. 3.27) results in an efficiency curve, shown in Fig. 5.5, deduced by considering the ratio of the measured energy spectrum of the tritium source and the expected theoretical spectrum, convolved with the detector resolution. The efficiency loss at energies below 2 keV causes the drop in the event rate that is visible at those energies in the solid red spectrum in Fig. 5.4, as opposed to the dashed blue distribution on the same plot.

Another feature distinguishing the solid red curve from the dashed blue one in Fig. 5.4 is the different resolution, whose trend was described in Chapter 3.

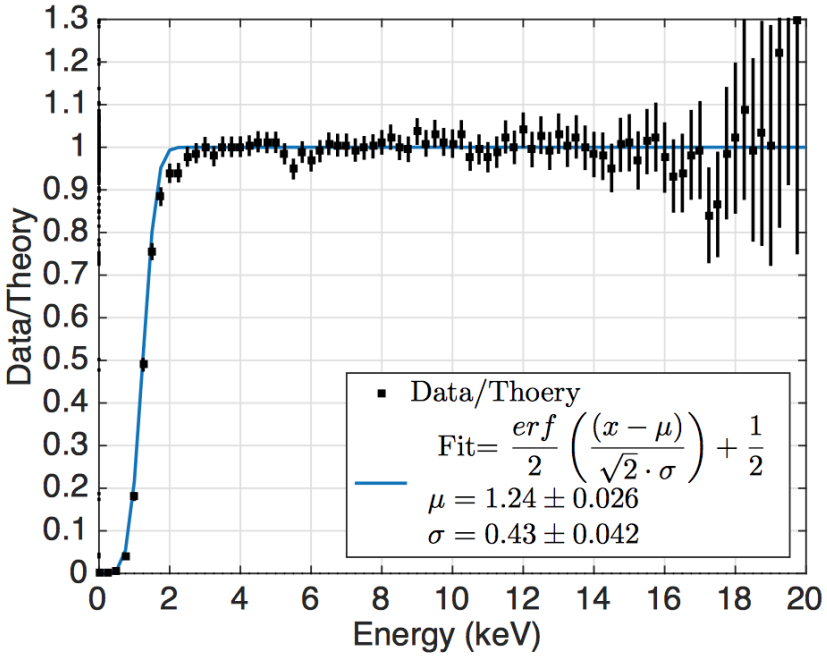

Figure 5.5 *Efficiency for electron recoils in LUX, estimated as the ratio of the measured tritium energy spectrum (c.f. Fig. 3.27) and the theoretical expectation convolved with the experimental resolution, fitted to an error function [133].*

The theoretical spectrum is smeared by taking into account the experimental resolution, resulting in the LUX expected spectrum. The resolution is modelled with the Noble Element Simulation Technique (NEST) package [134, 135, 150], and washes out the several theoretical spiky features (due to atomic shell) making them indistinguishable for LUX.

As discussed in Chapter 3, NEST is a powerful tool to translate the theoretical energy information to LUX-specific experimental quantities, associating $S1$ and $S2$ values to the true energy deposited in the detector. This leads to a subtle difference between the two spectra in Fig. 5.4. While the expected energy distribution is a function of the electron recoil energy in keV, the LUX-expected distribution is constructed on the combined energy scale:

$$E = [S1_c/g_1 + S2_c/(\epsilon g_2)]W, \tag{5.2}$$

where $S1_c$ is the $S1$ signal size corrected to equalize the response throughout the active volume to the response at the centre of the detector, while $S2_c$ is the $S2$ signal size corrected to equalize the response to that at the surface. For the $S1s$, corrections are $\pm 10\%$, while corrections from 0 to 50% are expected for the $S2s$.

$g_1 = 0.117 \pm 0.003$ phd/photon and $g_2 = 12.1 \pm 0.8$ phd/electron are the gain factors, defined by the expectation values of $S1$ and $S2$ (c.f. Chapter 3). The efficiency for extracting electrons from the liquid to the gas is $\epsilon = 49\% \pm 3\%$, and $W = (13.7 \pm 0.2)$ eV is the work function for the production of either a photon or an electron.

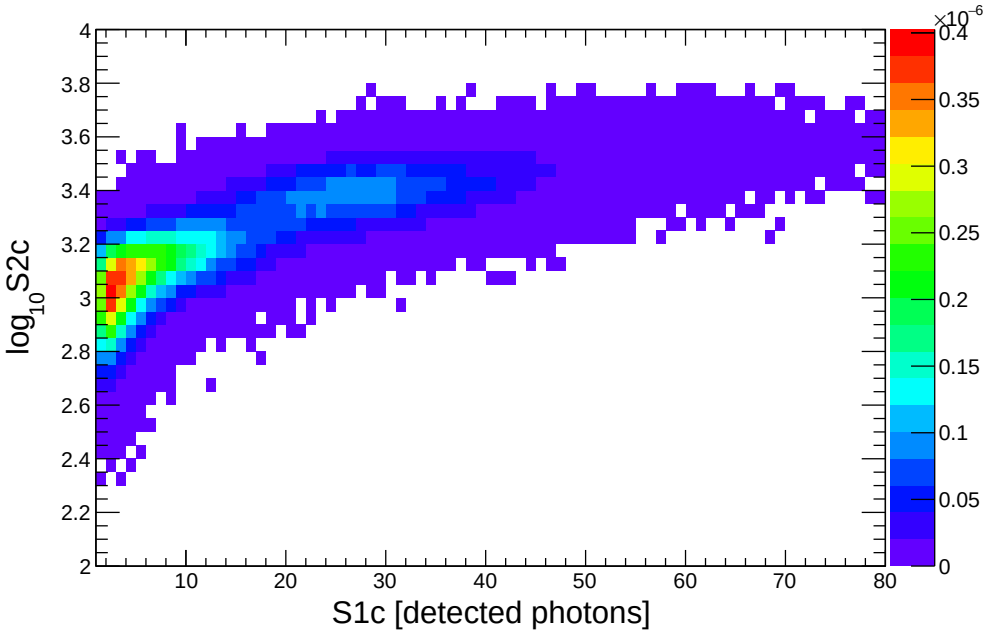

Figure 5.6 *Signal model projected in the two-dimensional space of* $\log_{10} S2_c$ *as a function of* $S1_c$*, for massless solar axions. The distribution peaks at low energies (corresponding to few units of detected photons in* $S1_c$*) and smoothly goes down to zero as the energy increases. The distribution falls in the electron-recoil band on the* $\log_{10} S2_c$ *axis, while on the third axis, coming out of the page, the scale of the distribution is proposed for an arbitrary choice of the coupling constant,* $g_{Ae} = 10^{-12}$.

So far we have discussed details of the axion signal model in terms of its energy distribution, without including any spatial information about the event location. According to theoretical expectations, potential axion interactions would result in additional events spread uniformly within the TPC. We are not expecting any feature in the radial distribution or in the depth placement of the signal events, as opposed to some of the background sources, that will be characterised by non-uniform spatial distributions. In order to obtain the axion spectrum on the spatial phase space, the LUX simulation package, LUXSim [136], has been used. Macros have been written to simulate energy depositions of the events, and distribute them uniformly throughout the active volume of the detector. For each of the simulated events, both position and energy information are obtained, to

be given in input to NEST. The LUX-specific quantities evaluated by NEST can be used either to produce the expected spectrum (Fig. 5.4), or to construct the four-dimensional signal model for massless solar axions. Consistently with the WIMP searches, the four dimensions are the four most informative experimental quantities in LUX: the prompt scintillation ($S1$), the base 10 logarithm of the proportional ($S2$) signal, and the radial (r) and vertical (z) position of the event location within the TPC.

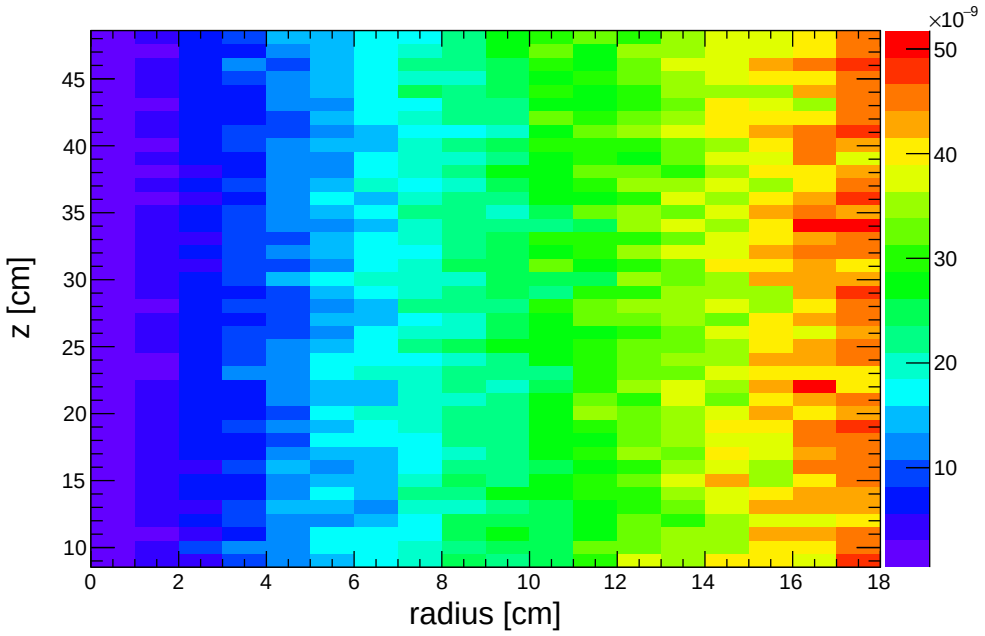

Figure 5.7 *Signal model projected in the two-dimensional space of z as a function of r, for massless solar axions. The distribution is uniform throughout the fiducial volume. On the third axis, coming out of the page, the scale of the distribution is proposed for an arbitrary choice of the coupling constant, $g_{Ae} = 10^{-12}$.*

Figure 5.6 presents the projection of the full PDF on the two-dimensional space of $\log_{10} S2_c$ as a function of $S1_c$. The signal events are distributed according to the event rate, peaking at low energies (corresponding to few units of detected photons in $S1_c$) and smoothly reduced to zero as the energy increases. On the $\log_{10} S2_c$ axis, the distribution falls in the electron-recoil band, because the signal is due to the electrons that are ejected from atoms when an axion is absorbed. On the third axis, colourful and coming out of the page, the scale of the distribution is proposed for an arbitrary choice of the coupling constant, $g_{Ae} = 10^{-12}$. The plot also shows the analysis cuts applied to the energy variables: $S1$ pulses are required to have two PMTs in coincidence and an $S1$ value in the range 1 – 80 detected photons, while the $S2$ signal is required to be in the range 100 – 10000

detected photons. With respect to the cuts described in Chapter 4, the upper threshold in energy for the axion analyses has been pushed from 50 phd up to 80 phd, to allow for the test of ALPs with masses up to 16 keV.

Figure 5.7 presents the projection of the full PDF on the two-dimensional space of z as a function of r, where z indicates the depth of the event location within the detector in cm, and r indicates the radial distance from the centre of it, in cm as well. The signal events are distributed uniformly throughout the volume, showing the fiducial selection made on the spatial coordinates. A radial cut is placed at 18 cm, and the range in depth is set to be 48.6 – 8.5 cm above the faces of the bottom PMTs. Consistently with Fig. 5.6, on the third axis, coming out of the page, the scale of the histogram is proposed for an arbitrary choice of the coupling constant, $g_{Ae} = 10^{-12}$.

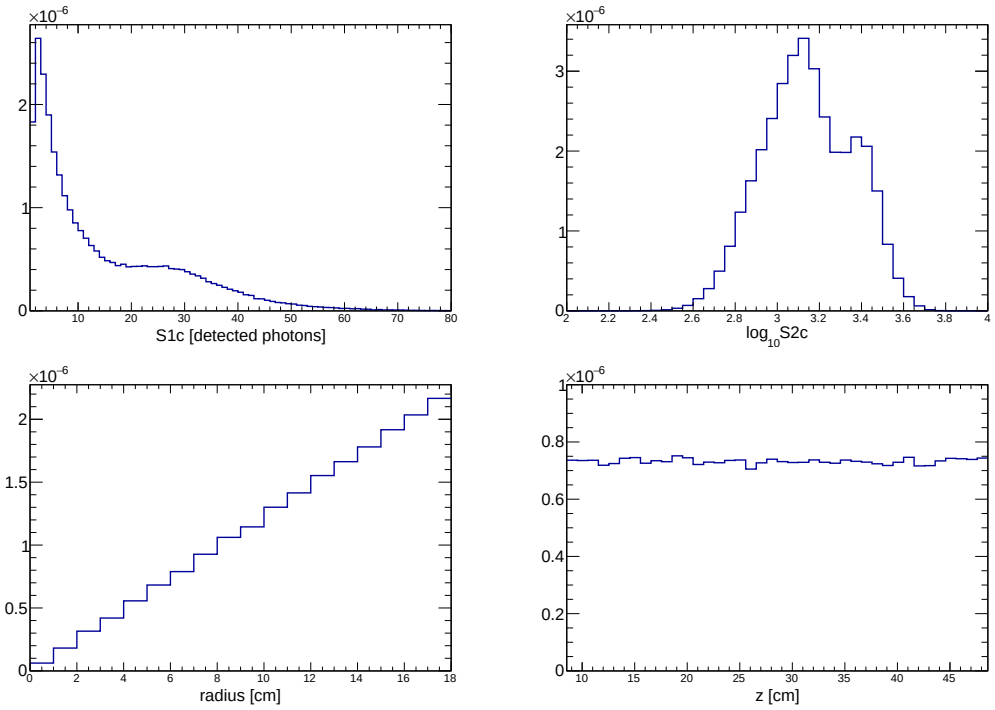

Figure 5.8 *The four panels show the projections of the four-dimensional signal model for massless solar axion on the four dimensions: $S1_c$ (top left), $log_{10}S2_c$ (top right), radial coordinate (bottom left), and vertical coordinate (bottom right).*

While the two-dimensional distributions help visualising the complexity of the full model, the projections on the single dimensions show some interesting features. The top left panel of Fig. 5.8 is the distribution of the primary scintillation signal $S1_c$, that shares its trend with the expected energy spectrum in Fig. 5.4. Peaked at low units of detected photons, it smoothly drops as the

number of photons increases. On the top right panel, the distribution on $\log_{10} S2_c$ is peaked at values falling in the centre of the electron-recoil band. The uniform spatial distribution is shown in both the bottom left and bottom right panels, in which we can see, respectively, a linearly rising trend in radius and a constant trend on the vertical coordinate.

5.1.3 Axion-like particles

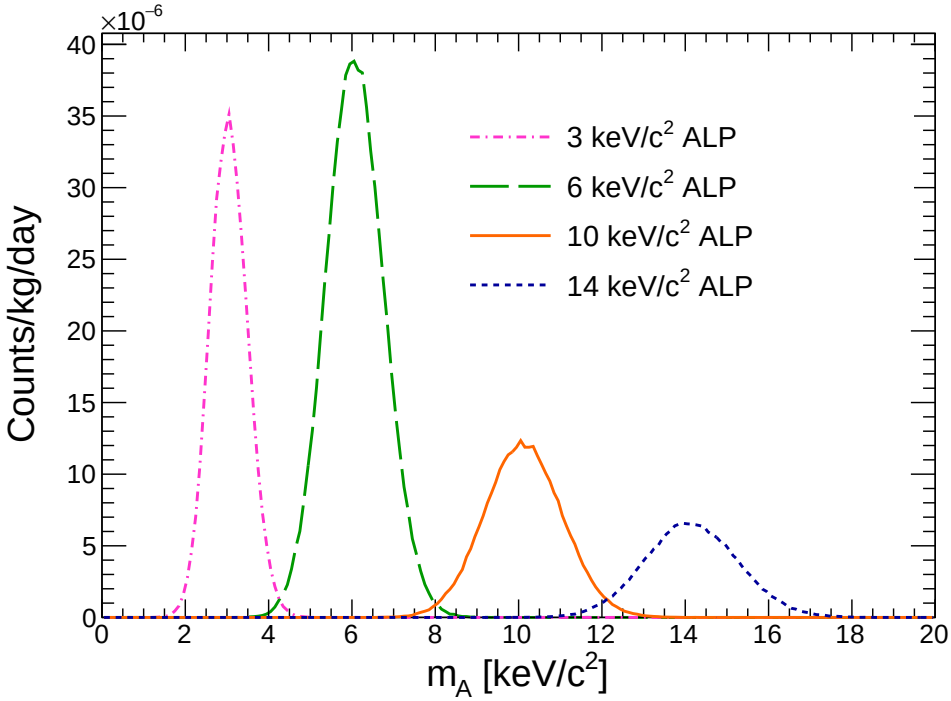

Figure 5.9 *A sample of axion-like particle energy spectra, for a selection of masses: $m_A = 3$ keV/c^2 (dot-dashed pink curve), $m_A = 6$ keV/c^2 (dashed green curve), $m_A = 10$ keV/c^2 (solid orange curve), and $m_A = 14$ keV/c^2 (dotted blue curve). The scale of the distributions is proposed for an arbitrary choice of the coupling constant, $g_{Ae} = 10^{-13}$.*

The model for solar axions is only one of the many different signal models to be tested in this analysis framework. While in the axion case we assume a massless candidate, the search for ALPs is quite different. ALPs do not arrive at Earth via a constant flux, but are non-relativistic particles present in the Galaxy and expected to interact with the electrons of the LUX detector. Being candidates for dark matter of unknown mass, the searches for ALPs are basically scans in

mass. The mass range LUX is sensitive to is 1 – 16 keV/c^2, limited by the energy scale over which precise knowledge of light and charge yield is determined through the tritium calibration described in Chapter 3. The analysis consists in testing LUX 2013 data against 31 different signal models, each of them representing a potential ALP with mass in the 1 – 16 keV/c^2 range, in steps of half a keV. The procedure to build all these models is very similar to the one just described for the solar axion case, but there are a few important differences to mention.

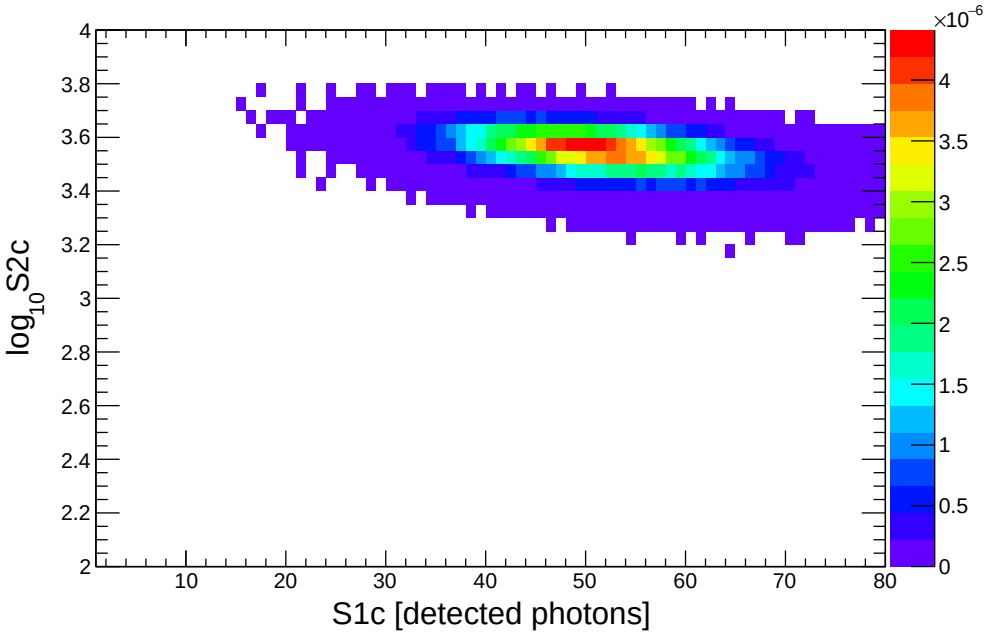

Figure 5.10 *Signal model projected in the two-dimensional space of* $\log_{10} S2_c$ *as a function of* $S1_c$*, for 10 keV/*c^2 *mass galactic ALPs. The distribution is a "blob" centred at the number of detected photons corresponding to the ALP mass, located in the electron-recoil band. On the third axis, coming out of the page, the scale of the distribution is given for an arbitrary choice of the coupling constant,* $g_{Ae} = 10^{-13}$.

As opposed to the solar axion case, the event rate for ALPs is directly proportional to g_{Ae}^2, rather than g_{Ae}^4, because of the absence of an incoming flux from the Sun. Being non-relativistic particles, if there is an interaction within the detector, the theoretical expectation is an axio-electric absorption leading to an electron recoil with kinetic energy equal to the mass of the ALP. Such an interaction produces a mono-energetic spectral feature, that may be turned to a signal model by including the effects of finite resolution, as described in the previous section. As a result, the expected LUX experimental energy spectrum for an ALP is a peak, centred at an energy equal to the mass of the candidate,

and with a width determined by the experimental resolution. As for the solar axion case, LUXSim and NEST have been used to convert the theoretical spectra into LUX models.

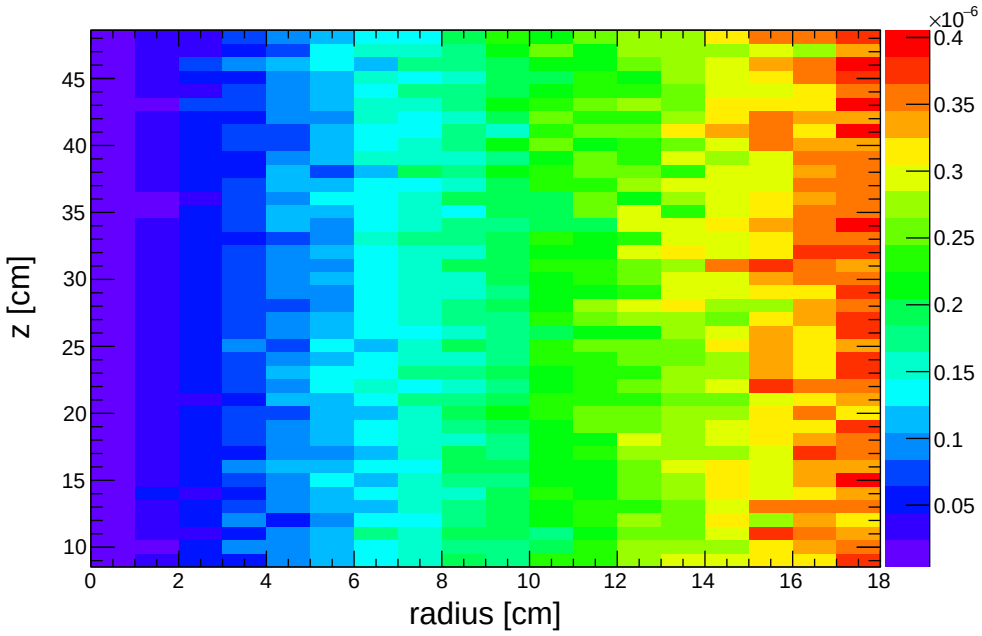

Figure 5.11 *Signal model projected in the two-dimensional space of z as a function of r, for 10 keV/c^2 mass galactic ALPs. The distribution is uniform throughout the fiducial volume. On the third axis, coming out of the page, the scale of the distribution is proposed for an arbitrary choice of the coupling constant, $g_{Ae} = 10^{-13}$.*

To give an example of what a spectrum looks like, Fig. 5.9 presents several such energy spectra, for $m_A = 3$ keV/c^2 (dot-dashed pink curve), $m_A = 6$ keV/c^2 (dashed green curve), $m_A = 10$ keV/c^2 (solid orange curve), and $m_A = 14$ keV/c^2 (dotted blue curve). All the models have been generated assuming a value for the axio-electric coupling ($g_{Ae} = 10^{-13}$), and all of them are plotted on the reconstructed energy scale in keV (c.f. Eq. 5.2). There are two features worth mentioning about these distributions. The first one is the relative scale of the different peaks, that reflects the trend of the axio-electric effect. From a comparison between Fig. 5.9 and Fig. 5.2 it is clear that the scale of the signal model for different masses is affected by different level of suppression due to the shape of the cross section. The underlying axio-electric cross section can also be traced via residual features, such as the non-smooth peak of the 10 keV/c^2 mass ALP. The four models also differ with respect to their characteristic resolution. This reflects the LUX energy-dependent resolution, that gets worse as the energy increases (c.f. Chapter 3).

The signal models for the axion-like particles are four-dimensional probability density functions. Figure 5.10 shows the projection of the signal model for a 10 keV/c^2 ALP on the two-dimensional space of $\log_{10} S2_c$ as a function of $S1_c$. The solid orange peak feature on the energy scale (Fig. 5.9) appears as a blob, with a density scale corresponding to an arbitrary choice of the coupling, $g_{Ae} = 10^{-13}$. The smearing on the x axis is directly related to the energy resolution, and the blob is centred on the electron-recoil band of the y axis.

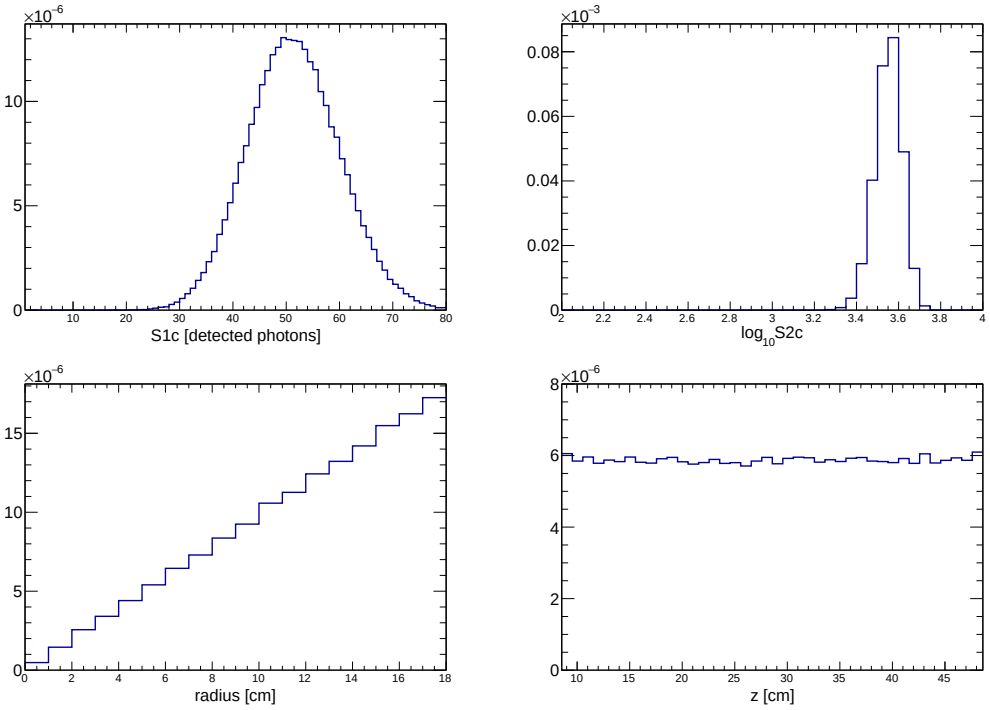

Figure 5.12 *The four panels show the projections of the four-dimensional signal model for 10 keV/c^2 mass galactic ALPs on the four dimensions: $S1_c$ (top left), $log_{10}S2_c$ (top right), radial coordinate (bottom left), and vertical coordinate (bottom right).*

ALP interactions would result in events spread uniformly within the detector. The projection of the full model on the two-dimensional space of the depth of the event location, z, as a function of the radial distance, r, is shown in Fig. 5.11. The same features discussed so far are shown on the projections on the single dimensions of the model in Fig. 5.12. The top left panel shows the peaked distribution on the primary scintillation signal, $S1_c$, while the top right panel shows the distribution on $\log_{10} S2_c$, centred at values falling in the electron-recoil band. As for the spatial projections, the trends are the same as in the solar axion case: a linearly rising distribution in radius and a constant trend on the z coordinate, indicating the spatial uniform distribution.

While the signal model is certainly the most informative ingredient of the data analysis, an accurate description of the expected background sources is essential to maximise the chances of signal discovery.

5.2 Background model

The sources of background that are expected in LUX were presented in Chapter 3, while the description of the modelling of the expectations within the LUX analysis framework was discussed in Chapter 4. This section provides a few details about adapting that background model to the axion analysis. Only backgrounds populating the electron-recoil band are considered, because they totally dominate over nuclear-recoil background events.

What distinguishes axion and ALP searches from WIMP searches is that, in the former case, the signal model is expected to be in the electron-recoil band, where also most of the backgrounds are expected, rather than in the nuclear-recoil band. This makes an accurate description of the contributions to the background essential, while making axion and ALP analyses challenging and very interesting.

5.2.1 The electron-recoil band populations

The electron-recoil band is mainly populated by Compton scattering of γ rays interacting within the active volume of the detector. These γ rays are usually generated from the decay of impurities in the detector components, but this is not the only source of this kind of background. An additional γ-ray population arises from heavily down-scattered emission from the ^{238}U chain, the ^{232}Th chain, and ^{60}Co decays in the centre of a large copper block sitting below the PMTs [131].

Electron-recoil events are also linked to radioisotopes decaying in the liquid xenon target. ^{85}Kr and Rn-daughter contaminants in the xenon undergo β decays, where the associated γ rays are not detected. Moreover, we expect γ rays from ^{85}Kr and Rn in the liquid xenon.

Another contribution is generated by x rays emitted as a consequence of those ^{127}Xe electron-capture decays where the coincident γ ray escapes the active volume. As already discussed in previous chapters, the ^{127}Xe background is due to cosmogenic activation of the isotope, that happened during the surface run

before the experiment was taken underground.

5.2.2 The model and the LUX data

As well as the signal models, each background component has been modelled as a four-dimensional probability density function. The four experimental quantities are, as usual, the prompt scintillation ($S1$), the base 10 logarithm of the proportional ($S2$) signal, the radial distance (r), and the depth (z) of the event location within the TPC. The resulting background model is shown in Fig. 5.13 as a stacked coloured histogram, superimposed with LUX 2013 electron-recoil data.

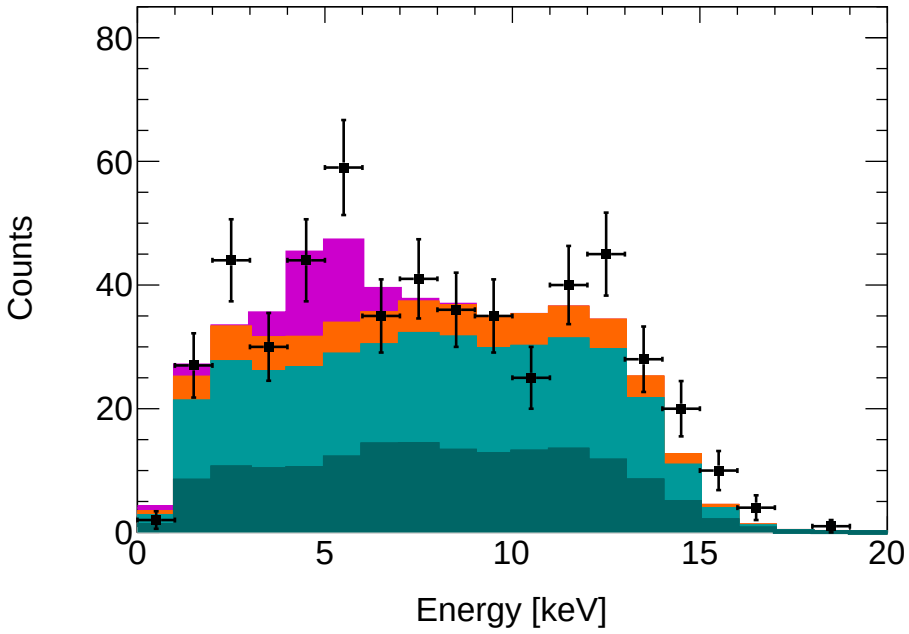

Figure 5.13 *Energy spectrum of the LUX 2013 electron recoil background. Data are filled black squares with error bars; the individual contributions to the background model sum up in the stacked coloured histogram: low-z-origin γ rays (dark green), other γ rays (light green), β decay of ^{85}Kr or Rn-daughter contaminants (orange), x rays due to ^{127}Xe (purple).*

The cutoff at higher energies is due to the cut in $S1$, that is required to be in the range of 1 – 80 detected photons. The γ-ray events are those in green, with a distinction being made between the ones originating at the bottom of the detector (dark green) and all the others (light green). β decays of ^{85}Kr and

Rn-daughter contaminants fill the orange component of the histogram, while x rays due to ^{127}Xe decay are the events in purple. All populations but ^{127}Xe are contributing as an almost flat trend to the overall shape, while the x-ray events due to ^{127}Xe decay appear as a peak centred at 5.2 keV. Sampling of the liquid xenon target, screening of detector materials (c.f. Fig. 3.18), and measurements of LUX data, have been employed to determine the expected activity for each of the background components [130].

Data are shown in Fig. 5.13 as filled black squares with error bars. The axion and ALP analyses test the coupling g_{Ae} using data collected in the period April 24th to September 1st, 2013, totalling an exposure of 118 kg fiducial mass over a 95 live days period. Selection cuts have been already discussed in Chapter 3.

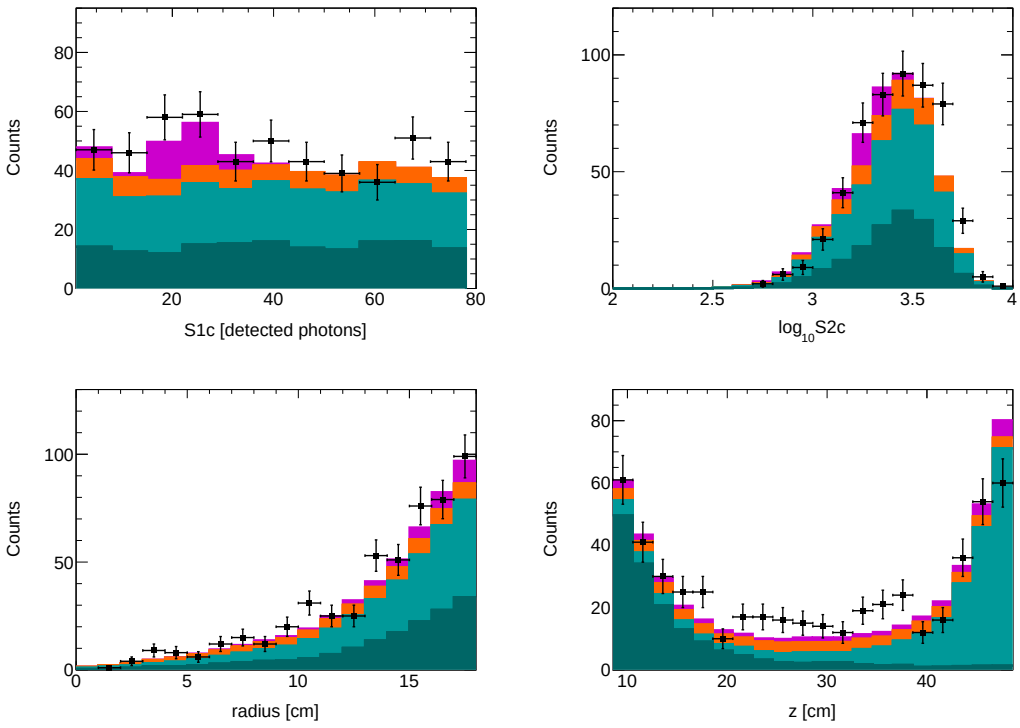

Figure 5.14 *LUX 2013 electron recoil data (filled black squares with error bars) together with the background model, comprised of contributions from low-z-origin γ rays (dark green), other γ rays (light green), β decay of ^{85}Kr or Rn-daughter contaminants (orange), and x rays due to ^{127}Xe (purple). The four panels show the distributions in terms of the usual four dimensions: $S1_c$ (top left), $\log_{10} S2_c$ (top right), radial coordinate r (bottom left), and vertical coordinate z (bottom right).*

Figure 5.14 shows the projections of both data and model on the usual four dimensions, using the same colour code as in Fig. 5.13. The $S1_c$ distribution on

the top left panel shows the almost flat contribution of the different components, above which the ^{127}Xe activation line arises. The top right panel has the usual electron-recoil band shape of the $\log_{10} S2_c$ variable. The radial distribution on the bottom left panel gives evidence of the self-shielding property of liquid xenon, showing all the background rates decreasing as approaching the centre of the detector. Finally, on the bottom right panel, we can see the distribution on the vertical coordinate of the event location: while the orange and purple histograms are uniformly distributed along the height of the TPC, the green component shows the distinction between the γ rays originating at the bottom of the detector (dark green, peaked at low-z values) and the other γ rays (light green, almost uniform along z).

Given a model, statistical tools exist to assess the goodness of the model as compared to the data. In this case, the unbinned Kolmogorov-Smirnow (KS) test has been chosen. It compares a data sample with a reference probability distribution, quantifying the maximum difference between the distribution function of the sample and the cumulative distribution of the reference model [151, 152]. The p values obtained for the distributions in Fig. 5.14 are 0.76 on $S1_c$, 0.03 on $\log_{10} S2_c$, 0.60 on r, and 0.09 on z. The low values in $\log_{10} S2_c$ and z quantize the discrepancies between data and model that can be noticed on the corresponding plots. Nevertheless, in a KS test, p values are expected to be uniformly distributed between 0 and 1. The obtained values average at 0.37, and are then sufficently close to expectation.

5.3 Analysis technique

The aim of the axion and ALP analyses is testing the signal models against LUX 2013 data, given the description of the expected background rate. When searching for signal, if no evidence can be found, a statistical limit on the number of signal events can be set. We chose the same statistical approach as in the standard WIMP searches presented in Chapter 4: a Profile Likelihood Ratio (PLR) analysis [142]. This section is dedicated to a detailed discussion about the PLR optimisation for electron-recoil band searches, as this is the first such analysis performed in the LUX Collaboration.

5.3.1 Profile Likelihood Ratio hypothesis test

Statisticians usually refer to "likelihood" as a function of the parameters of a statistical model, given some data. Likelihood functions can then be used to estimate parameters. In search experiments, the Profile Likelihood Ratio approach allows to identify confidence intervals (upper or lower limits) for the parameters of the theory that has been tested against the data.

Assuming that a selection procedure has been applied, the selected events can fill histogram with M bins. The number of events in the ith bin is n_i, while the number of expected events in the same bin can be expressed as $\mu s_i + b_i$, i.e. the sum of the number of events due to all known processes, b_i, and the number of events due to the signal, μs_i,. The quantity μ is the parameter of interest of the analysis, and identifies a chosen rate for the signal hypothesis. The background-only hypothesis is characterised by a null value of μ. All the other parameters involved in the analysis are called nuisance parameters, $\underline{\theta}$ (c.f. Chapter 4).

The likelihood function can be built as:

$$L(\underline{n}|\mu, \underline{\theta}) = \prod_{i=1}^{M} \frac{(\mu s_i + b_i)^{n_i} \cdot e^{-(\mu s_i + b_i)}}{n_i!}. \tag{5.3}$$

The test statistic, q_μ, is then obtained taking the ratio of two likelihoods:

$$q_\mu = -2ln\frac{L(\mu, \widehat{\widehat{\underline{\theta}}})}{L(\widehat{\mu}, \widehat{\underline{\theta}})}, \tag{5.4}$$

where $\widehat{\widehat{\underline{\theta}}}$ are the values of the nuisance parameters that maximize L at μ fixed, while $\widehat{\mu}$ and $\widehat{\underline{\theta}}$ are the best values of the parameters obtained by maximizing L.

The statistical analysis consists of a scan over different values of signal rate, μ, to establish the likelihood of the corresponding alternative hypothesis, H_μ, as opposed to the background-only hypothesis, H_0, built for $\mu = 0$. If we call $f(q_\mu|\mu)$ the probability density function of the test statistic q_μ given the hypothesis H_μ, and $f(q_\mu|0)$ the one of q_μ given H_0, then the separation between the two PDFs determines the capability to discriminate between the two hypotheses. The alternative hypothesis, H_μ, is usually referred to as the signal plus background hypothesis, with μ indicating the number of signal events.

We scan over the number of signal events to be tested, and for each of them the hypothesis test produces 1000 [1] pseudo-experiments according to the two hypotheses. The distributions of the test statistic for both H_μ and H_0 are built, and the test statistic on the data, q_{obs}, is evaluated. This information will be used to extract the confidence level for the alternative hypothesis.

5.3.2 Analysis parameters

Before moving on to the data interpretation, we give a few more details about the experimental observables and the nuisance parameters used in the analysis.

Given the signal (P^{sig}) and background (P_i^{bkg}) models defined in the previous sections, we can define the full model, P^{tot}, as:

$$P^{tot} = nSig \cdot P^{sig} + \sum_i nBkg_i \cdot P_i^{bkg}, \tag{5.5}$$

where the sum $\sum_i$ is a sum over the $nBkg_i$-events background contributions. A full model exists for each of the signal models available, and the number of signal events, $nSig$, is the parameter of interest. The hypothesis of the background model fitting the data properly is H_0, while the hypothesis of the data being better described by the full model is H_μ.

The models are built on the usual experimental observables, that represent the variables the PLR discriminates against, given the two hypotheses. Table 5.1 summarises the minimum and maximum value allowed for each of the observables.

Observable	Minimum	Maximum	Description
$S1_c$	1 phd	80 phd	Prompt scintillation
$\log_{10} S2_c$	2	4	Base 10 log of the proportional signal
r	0 cm	18 cm	Radius of the event location
z	8.5 cm	48.6 cm	Depth of the event location

Table 5.1 *The observables used in the PLR analyses for axion and ALP searches, reported with their selected ranges and a brief description.*

[1] The number of pseudo-experiments has been chosen to get the best compromise between high enough statistics and reasonable computing time.

Consistently with WIMP analyses (c.f. Chapter 4), the nuisance parameters in the axion and ALP searches are the background rates. The number of events of each of the background components is given to the PLR as a Gaussian distribution, centred at the expectation value and having a width determined by the level of precision that component is estimated with. The PLR is then allowed to vary the number of counts of each contribution according to its Gaussian probability distribution, in order to find the best fit to the data, treating the background rates as systematic uncertainties.

Table 5.2 lists the nuisance parameters with their expectation values, for an exposure of 95 live days × 118 kg, and the standard deviations of their Gaussian distributions.

Parameter	Expectation value	Standard deviation
Low-z-origin γ counts	161	69
Other γ counts	223	96
β counts	67	27
^{127}Xe counts	39	12

Table 5.2 *The nuisance parameters: each of them is listed with the mean and the standard deviation of its Gaussian distribution. Event counts are after analysis cuts and thresholds, as described in Chapter 4.*

5.3.3 Data interpretation

The Profile Likelihood Ratio analysis can be used to extract the confidence level of each of the alternative hypotheses, given a choice of observables and parameters. The pseudo-experiments used for this purpose are generated through a ROOT class [153], that has been adapted to the axion and ALP searches in LUX. To provide an example of the working principle of the analysis framework, we discuss the case of an axion-like particle candidate.

Given a value of μ, the hypothesis test produces 1000 pseudo-experiments according to both H_μ and H_0, populating two histograms. These histograms represent the distributions of the test statistic, q_μ, and are shown in Fig. 5.15, for 15 different choices of μ. The blue and red histograms represent, respectively, the distributions of the test statistic for the background-only hypothesis, H_0, and for the signal plus background hypothesis, H_μ. The black vertical line identifies q_{obs}, that is the test statistic evaluated on real data.

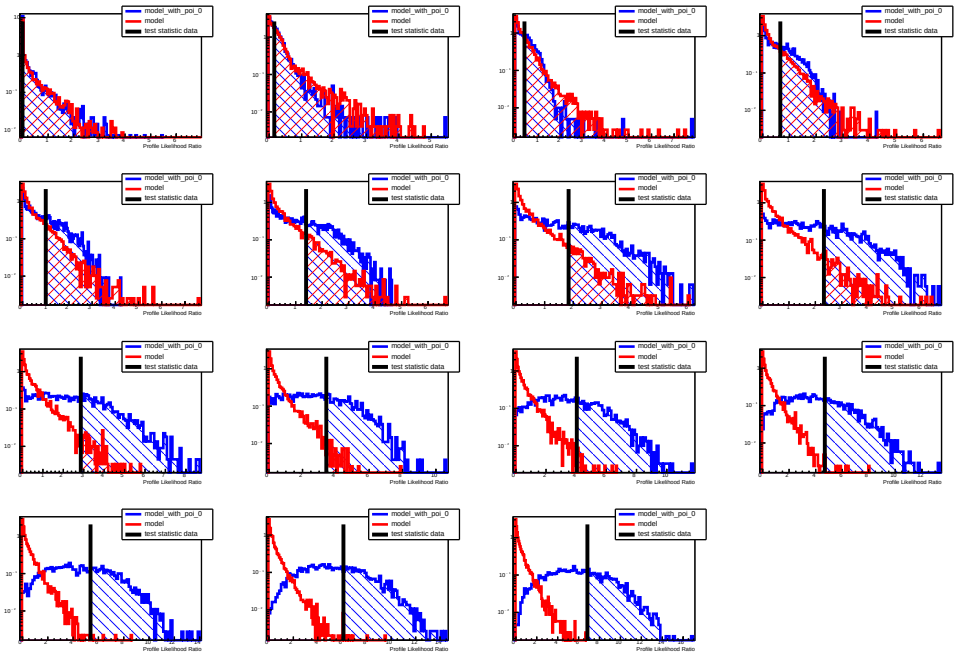

Figure 5.15 *For 15 different number of signal events, the blue and red histograms represent, respectively, the distributions of the test statistic for the background-only hypothesis, H_0, and for the signal plus background hypothesis, H_μ. The black vertical line identifies q_{obs}, that is the test statistic as evaluated on real data.*

Moving from one panel of Fig. 5.15 to the next, the larger is the number of signal events, the more the two histograms are separated. The PLR evaluates the confidence level for the signal plus background hypothesis as:

$$CL_{s+b} = \int_{q_{obs}}^{\infty} f(q_\mu|\mu)dq_\mu, \tag{5.6}$$

that corresponds to the area of $f(q_\mu|\mu)$ (the red histogram) to the right of q_{obs}. This quantity is a probability content, and is called the p value. For the axion and ALP analyses in LUX, we work at 90% confidence level, thus p values below 10% are rejected. Given the maximum likelihood estimator, $\widehat{\mu}$, that we have already defined as the value of μ that maximizes the likelihood (Eq. 5.3), a low p value can be obtained in two ways. The estimated $\widehat{\mu}$ may be found to be either greater or less than μ. As a consequence, the set of μ values that are rejected because of their p value being lower than 10% may lie to either side of accepted μ values. This means that we can set a two-sided limit [2] on the parameter of interest [142].

[2]Confidence intervals can be either one- or two-sided. The former case applies to searches where the maximum likelihood estimator for the parameter of interest is expected to be only

The 15 p values obtained from Fig. 5.15 are plotted as a function of the number of signal events in Fig. 5.16. The red dots represent the CL_{s+b} (Eq. 5.6), while the black dots correspond to the p values of the background-only hypothesis, CL_b, defined as the area of $f(q_\mu|0)$ (the blue histogram) to the right of q_{obs}:

$$CL_b = \int_{q_{obs}}^{\infty} f(q_\mu|0)dq_\mu. \tag{5.7}$$

The blue dots correspond to the ratio of the confidence levels, $CL_s = CL_{s+b}/CL_b$, that has not been used in these analyses.

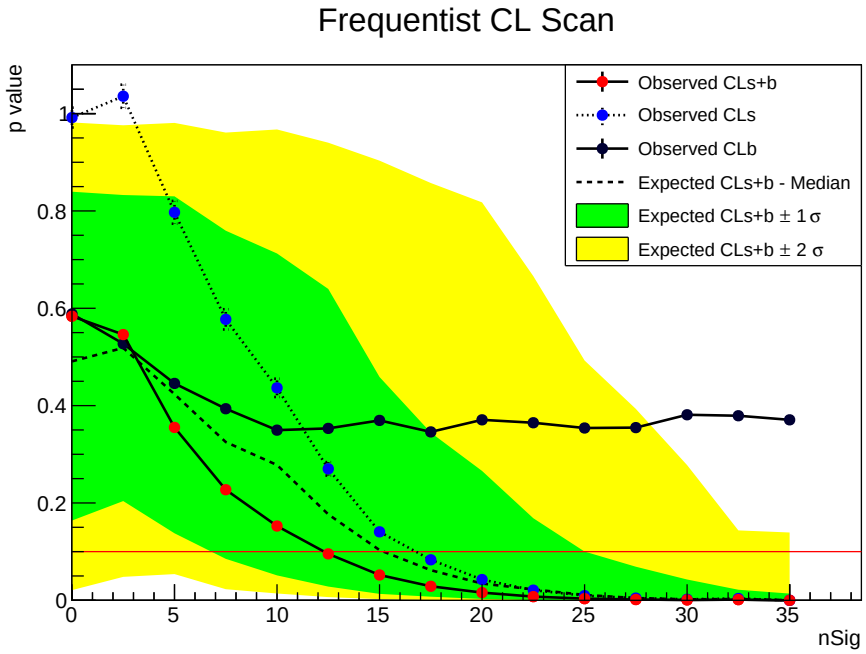

Figure 5.16 *The p value as a function of the number of signal events. The confidence level for the full model, CL_{s+b}, is shown as the red dots, while CL_b as the black dots; the ratio of the two is represented by the blue dots. The dashed black line shows the trend of the expected CL_{s+b}, and the green and yellow bands indicate, respectively, the $\pm$ 1 σ and $\pm$ 2 σ from the expectation.*

The dashed black line and the coloured bands on Fig. 5.16 represent the expectations. In this case the CL_{s+b} is evaluated given the value of q_{obs} obtained from a data set generated on the background-only hypothesis, rather than from real data. The expected CL_{s+b} is represented by the dashed black line, with a green and yellow band showing, respectively, the $\pm$ 1 σ and $\pm$ 2 σ from the expectation.

greater or less than μ. In such situations, one can only set a lower or upper limit.

Several informations can be extracted from Fig. 5.16. First of all, the comparison between the expected and observed CL_{s+b} gives an indication of the compatibility of data and background model. In this example, the distribution of the observed CL_{s+b} lays within the $\pm$ 1 σ band of expectations, indicating no evidence for signal in real data. The horizontal red line in Fig. 5.16 represents the 10% threshold in p value we have already discussed. Values of μ corresponding to p values below the threshold are excluded. In this example, an upper limit is obtained, and we exclude the signal plus background hypothesis for that chosen ALP candidate, for numbers of signal events larger than 12.3, at 90% C.L.

The limit on the number of signal events is then converted to a limit on the coupling constant between axion or ALP and electrons, g_{Ae}, by exploiting the proportionality between the signal event rate and the coupling. The event rate for a solar axion signal scales with g_{Ae}^4, while an ALP would interact with a rate proportional to g_{Ae}^2. Inverting these relationships, the coupling is proportional to the α-power of the number of signal events:

$$g_{Ae}(90\%CL) = g_{Ae}(0) \cdot \left(\frac{nSig(90\%CL)}{nPDF(0)} \right)^{\alpha}, \tag{5.8}$$

with $\alpha = 0.25$ in the solar axion case, and $\alpha = 0.50$ for galactic ALPs. In Eq. 5.8, $nSig(90\%CL)$ is the 90% C.L. limit on the number of signal events returned by the PLR, while the other two parameters depend on each other. Indeed, $g_{Ae}(0)$ is the arbitrary value assumed for the coupling constant when generating the signal model, and $nPDF(0)$ is the resulting number of signal events [3].

As the CL_{s+b} observed on the data is compatible with the expectations based on the background-only hypothesis (c.f. Fig. 5.16), the statistical analysis did not return any evidence for discovery of a signal due to the candidate searched for. Therefore, we can exclude the signal hypothesis at the chosen level of confidence. In case of discovery, a discrepancy between the observed and expected distribution would arise, resulting in very different p values for the same value of μ [4].

[3] $nPDF(0)$ represents the integral of the signal model used in the analysis (e.g. the area of the probability density function in Fig. 5.6).

[4] In order to state that the PLR found evidence for signal, and that there was a discovery in the data, the observed CL_{s+b} is usually requested to be 5σ away from the expected.

5.4 Results

The analysis technique described in the previous section has been applied to the search for both axions and axion-like particles in the 95 live days × 118 kg exposure of LUX 2013 data. The results obtained follow.

5.4.1 The solar axions limit

The data have been first searched for a feature compatible with the solar axion signal model (Fig. 5.4, 5.6, and 5.7). Systematic uncertainties in the background rates are treated as nuisance parameters. Table 5.3 summarizes the contributions from the background sources, listing the number of events expected in the total exposure and the best fit value returned by the PLR in the solar axion search. As previously discussed, the constraints are Gaussian distributions, with means and standard deviations indicated.

The KS test is performed on the background model distributions in Fig. 5.14, and then repeated at the end of the analysis, when the contributions were scaled according to the best fit values reported in Table 5.3. The resulting p values for the solar axion best fit are 0.72 on $S1_c$, 0.03 on $\log_{10} S2_c$, 0.57 on r, and 0.54 on z. The still poor value in $\log_{10} S2_c$ quantifies the discrepancy between data and model on that observable. Nevertheless, the average p value of 0.47 indicates sufficiently good fits, and therefore does not justify any change in the background model to further improve the match with data.

Parameter	Constraint	Fit value (solar axions)
Low-z-origin γ counts	161 ± 69	157 ± 17
Other γ counts	223 ± 96	175 ± 18
β counts	67 ± 27	113 ± 18
^{127}Xe counts	39 ± 12	42 ± 8

Table 5.3 *Nuisance parameters in the best fit to the LUX 2013 data for the solar axion search. Constraints are Gaussian with means and standard deviations indicated. Fit values are the best ones found by the PLR.*

A study of the correlation between the nuisance parameters themselves and between the nuisances and the parameter of interest has been performed. Results are summarized in Table 5.4.

	Low-z-origin γ	Other γ	β	^{127}Xe	Signal events
Low-z-origin γ	1				
Other γ	-0.004	1			
β	-0.26	-0.31	1		
^{127}Xe	-0.10	-0.14	0.03	1	
Signal events	-0.11	-0.10	-0.38	-0.08	1

Table 5.4 *The indexes of correlation between the nuisance parameters themselves and between the nuisances and the parameter of interest, in the solar axion search.*

Figure 5.13 and 5.14 can be used to visualise the correlations. The correlation indexes are mostly negative, as the increase in the activity of one of the background components tends to lead to a decrease in the others. The low-z-origin γ and other γ counts are not strongly correlated with each other, as they have different spatial distributions. Both of them show a considerable correlation with β counts – a correlation driven by the energy distributions of the three components. The ^{127}Xe background has a weak correlation with all the other components because of its peculiar energy distribution. The number of signal events is mostly correlated with β counts, because this background component is the only one with a uniform spatial distribution (as well as the solar axion signal) and with an energy distribution similar to the signal. The correlation with γ counts is not strong because of the different spatial distributions, while the correlation with the ^{127}Xe component is tiny because the peaked energy distribution of the background is not compatible with the signal shape.

No evidence for signal has been found, and an upper limit on the coupling, g_{Ae}, has been set, at 90% C.L. The result is shown, as a function of the candidate mass, in Fig. 5.17, along with the limits set by the previous experiments [69, 111, 154, 155], the astrophysical limit set via the Red Giant cooling process [156], and the theoretical models describing QCD axions [55–58] that have been described in Chapter 2. The LUX 2013 data set excludes a coupling larger than 3.5×10^{-12} at 90% C.L., reporting a limit that is worse than the expected sensitivity [5] but still laying within the $\pm$ 2 σ band. The result is the most stringent such limit reported to date, as published in 2017 in Ref. [146].

Model-dependent limits on the candidate mass can also be set. Assuming

[5] An explanation for the upper limit being worse than the expected sensitivity can be found in the slight excess of data with respect to the expectation (c.f. Fig. 5.13 and 5.14).

the Dine-Fischler-Srednicki-Zhitnitsky model, the upper limit on the coupling corresponds to an upper limit on axion mass of 0.12 eV/c^2, while for the Kim-Shifman-Vainshtein-Zhakharov description, masses above 36.6 eV/c^2 are excluded.

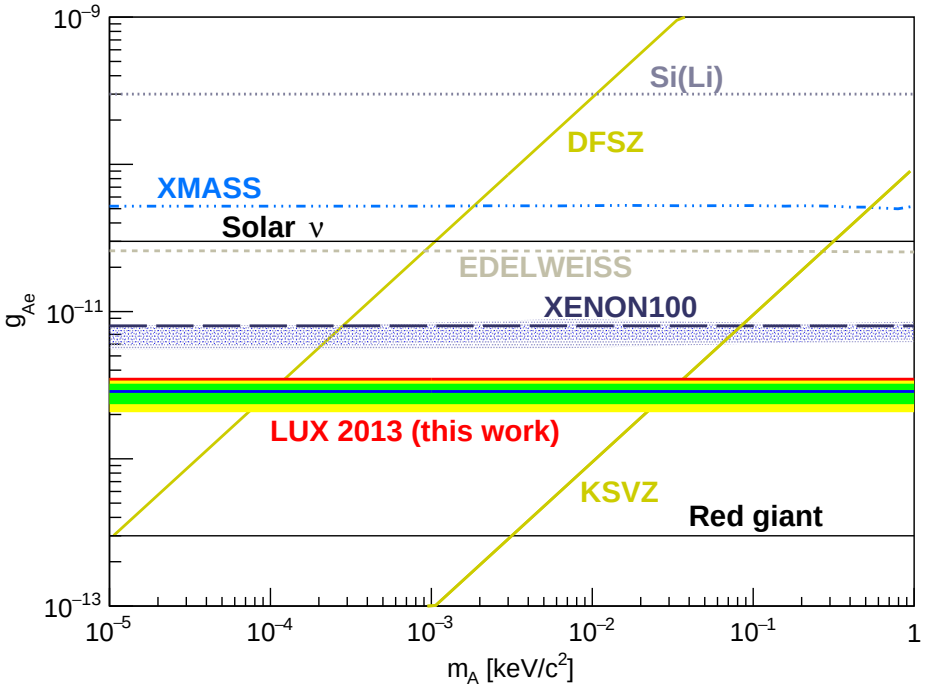

Figure 5.17 *Red curve: LUX 2013 data 90% C.L. upper limit on the coupling between solar axions and electrons. Blue curve: 90% C.L. sensitivity, ± 1 σ (green band), and ± 2 σ (yellow band). Results from other experiments are included (as published in 2017 in Ref. [146]), as well as the astrophysical limit set via the Red Giant cooling process, and the theoretical models describing QCD axions.*

5.4.2 The Look Elsewhere Effect and the ALPs limit

The LUX 2013 data have also been tested against 31 signal models, each representing an ALP with mass in the 1 – 16 keV/c^2 range. Masses have been chosen in steps of half a keV within this range. The local significance of observing a feature compatible with an ALP signal at one particular mass must be moderated by the number of trials undertaken, in order to calculate a global significance across the entire energy range that is explored [157]. The local p value refers to a single mass, and is the probability of finding an excess even if

there is no real ALP signal at that mass.

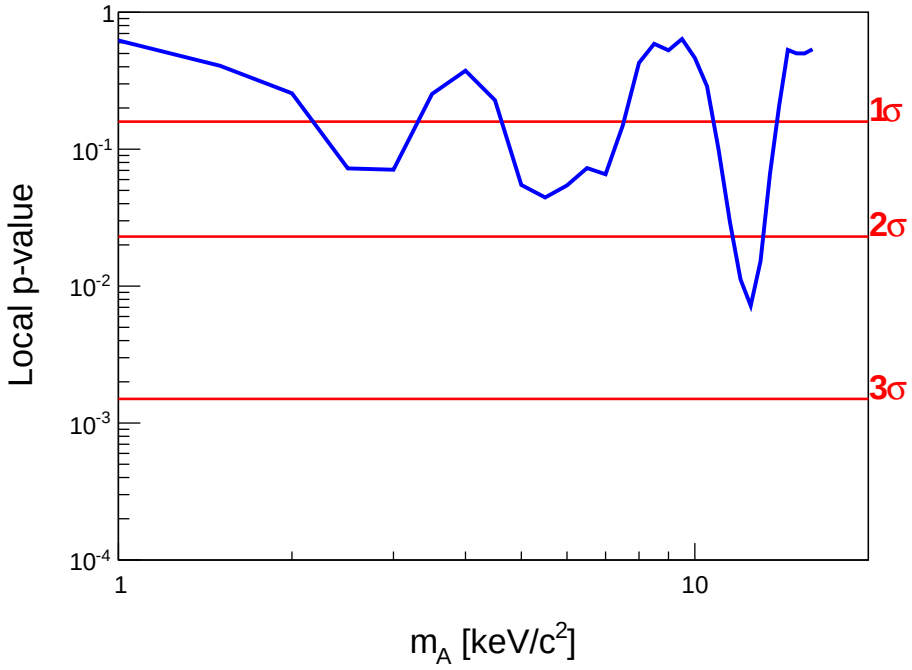

Figure 5.18 *The local p value as a function of the ALP mass. The minimum is reached at 12.5 keV/c^2, where the local p value is 7.2 × 10^{-3}, corresponding to a 2.4 σ local deviation.*

In Fig. 5.18, the local p value for each of the ALP masses selected is shown. The corresponding number of standard deviations (σ) away from the background-only hypothesis is also reported. The trend of the local p value can be justified by the spectrum shown in Fig. 5.13. Downward peaks in p value correspond to large deviations between the data and the background model. In regions where the data are fluctuating above the background expectation level, the PLR is easily recognising a potential peaked signal due to ALP interactions. At 12.5 keV/c^2 mass, a local p value of 7.2×10^{-3} corresponds to a 2.4 σ deviation. Following the procedure outlined in Ref. [158] (where it was applied to searches for the Higgs boson), a boost factor has been calculated that evaluates the likelihood of finding a deviation for a number of searches as compared to the significance that would apply to a search performed only once. Such an approach reduces the significance of any excess found, to take into account that the probability of having an upward fluctuation in the data becomes higher over a wide energy window as opposed to a narrow one. Consequently, the global p value at 12.5 keV/c^2 is estimated to be 5.2×10^{-2}, corresponding to a 1.6 σ rejection of the background-only hypothesis. As the global deviation is within the 2 σ band, the excess seen in the data at that

energy can be considered an upward fluctuation and not an evidence for signal discovery.

The goodness of the PLR fit has been studied also in the ALP search. We report the p values for the 12.5 keV/c^2 mass case only, as it is the one that deviates most from the background-only hypothesis. P values of 0.67 on $S1_c$, 0.02 on $\log_{10} S2_c$, 0.52 on r, and 0.49 on z have been found. The only still poor agreement appears in the $\log_{10} S2_c$ distribution, consistently with what has been obtained in the solar axion search.

As for the parameters' correlation study, tables for all the ALP masses analogous to Table 5.4 are not inserted for length reasons, but it is worth mentioning that a 5 keV/c^2 ALP signal has a -0.37 correlation index with ^{127}Xe counts. Such a strong correlation is justified by the very similar energy distributions of signal and background, given that the ^{127}Xe line is centred at 5.2 keV.

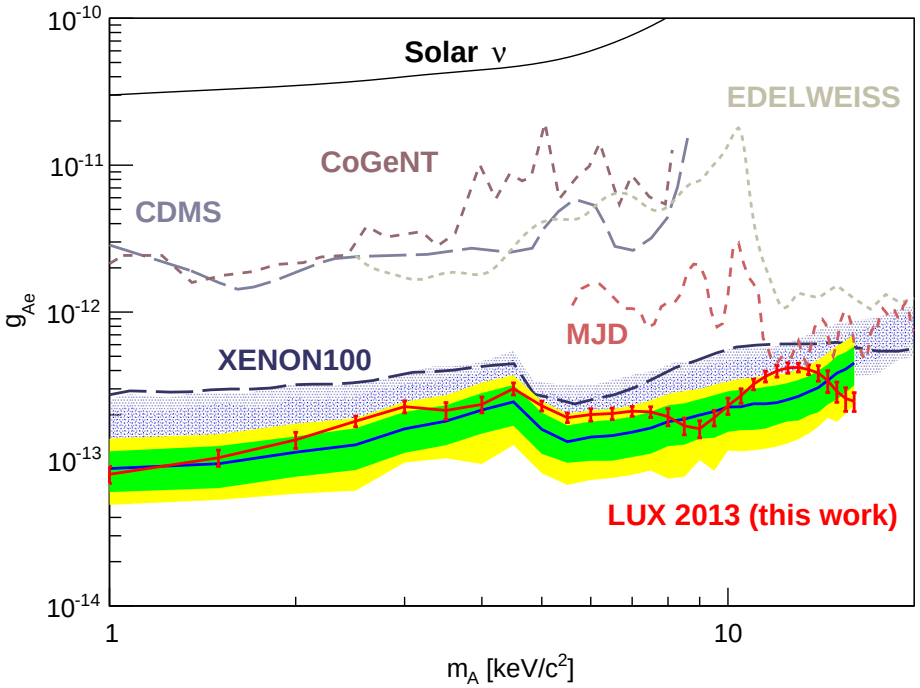

Figure 5.19 *Red curve: LUX 2013 data 90% C.L. upper limit on the coupling between galactic axion-like particles and electrons. Blue curve: 90% C.L. sensitivity, ± 1 σ (green band), and ± 2 σ (yellow band). Results from other experiments are also included (as published in 2017 in Ref. [146]).*

Axion-like particle searches in LUX did not return any evidence for signal. Assuming that ALPs constitute all of the galactic dark matter, the 90% C.L. upper limit on the coupling between ALPs and electrons is shown in Fig. 5.19 as a function of the mass. Results set by other experiments are inserted for comparison [69, 111, 154, 159–161]. Again, this is the most stringent such limit reported to date in this mass range [146]. LUX constrains values of the coupling to be no larger than 4.2×10^{-13}, across the full range.

The expected LUX limit (blue curve on Fig. 5.19) mimics the trend of the XENON100 result, as the overall shape is given by the axio-electric cross section on the target material (Fig. 5.2) that is xenon in both experiments. The red curve on Fig. 5.19 shows that the LUX limit deviates from the expectation for certain masses. The deviations can be interpreted, once again, as a consequences of the deviation between the data and the background model (c.f. Fig. 5.13 and 5.18).

The limits set by LUX and the other experiments of the current generation are covering an interesting phase space. Nevertheless, next generation experiments will be able to probe even wider regions of the parameter space. This is the case of the upgrade of LUX, the LUX–ZEPLIN experiment.

5.5 Beyond LUX

LUX has finished its operations in the summer 2016 and has been decommissioned starting in September 2016. The end of LUX opens the way to its upgrade, the LUX–ZEPLIN (LZ) experiment, that will be installed in the Davis Cavern at the Sanford Underground Research Facility, taking place in the same water tank that hosted LUX. First data taking is planned to start in 2020, and LZ is expected to run for 1000 live days.

5.5.1 The LZ experiment

The LZ experiment is a dual-phase xenon time projection chamber containing 7 active tonnes (out of 10 tonnes total) of liquid xenon. The working principle of such a device has been fully described in Chapter 3. Figure 5.20 shows a three-dimensional model of the LZ detector, as placed in the already existing water tank. The design takes advantage from the previous experiences of LUX and

ZEPLIN, the two experiments LZ is named after. An important improvement with respect to its progenitors is the addition of a nearly hermetic liquid organic scintillator (gadolinium–loaded linear alkyl benzene) outer detector, that surrounds the central cryostat vessels and the TPC. The PMTs mounted in the outer water shield simultaneously view the light from the scintillator and the inner water volumes. The benefits of such an outer detector are many. First of all, together with the so-called "skin", it acts as a veto system against internally generated backgrounds (both γ rays and neutrons), allowing an increase in the fiducial volume, as those events are mainly expected in the outer regions of the detector. The skin is composed by the liquid xenon located between the PTFE (polytetrafluoroethylene or Teflon) structure surrounding the active region and the cryostat wall, and the liquid xenon laying beneath the bottom PMT array. In addition to this, combined with the inner xenon detector, the outer scintillator will provide direct measurements of the internal radioactivity backgrounds.

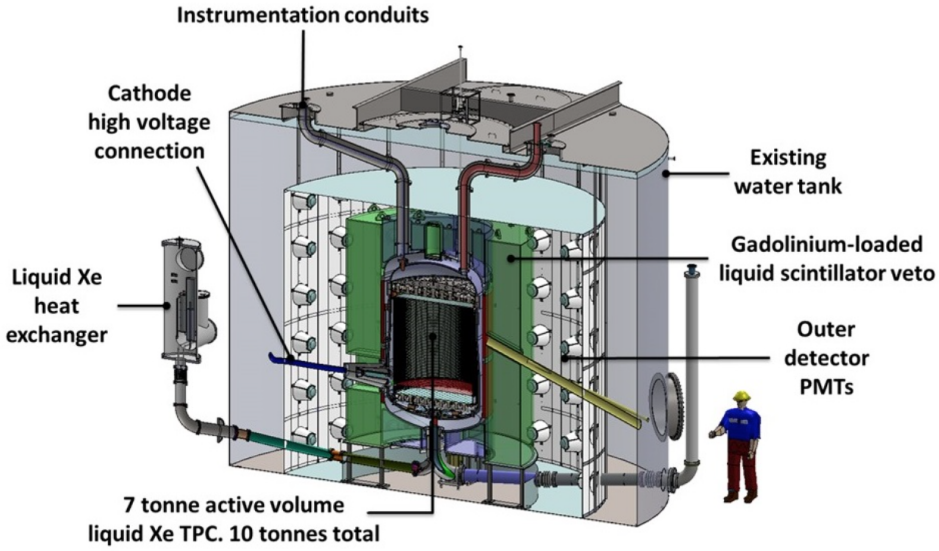

Figure 5.20 *A three-dimensional model of the LZ detector [162].*

Three source tubes enter the water and the organic scintillator to enable detector calibrations, allowing neutron and γ-ray sources to be positioned next to the inner cryostat. A xenon gas system will be used to introduce other sources (such as krypton and tritiated methane) directly into the liquid xenon, while an external neutron generator, producing neutrons through a deuterium-deuterium fusion reaction, will be employed for nuclear recoil calibrations. These are very important as the LZ experiment has been optimised for direct dark matter searches of WIMPs. Nevertheless, the scientific programme includes a

variety of studies to be performed on LZ data, and the axion and ALP analyses are at the top of the list.

5.5.2 The LZ analysis framework

As opposed to the analysis performed on the LUX data, in LZ, as in any other experiment that has not collected data yet, we are not able to set any limits (neither claim a discovery). What can be done though is to estimate the sensitivity reach of the experiment. Assuming that no evidence for signal will be found in the expected 1000 live days × 5.6 tonnes exposure, we can estimate the region of the parameter space that LZ will be able to cover. The statistical approach to such an analysis is, again, a Profile Likelihood Ratio technique. Real data are replaced by simulations, and a data set of given exposure is randomly generated on the background model. The rest of the analysis chain mostly mimics the one described for LUX, thus this section only points out the main differences.

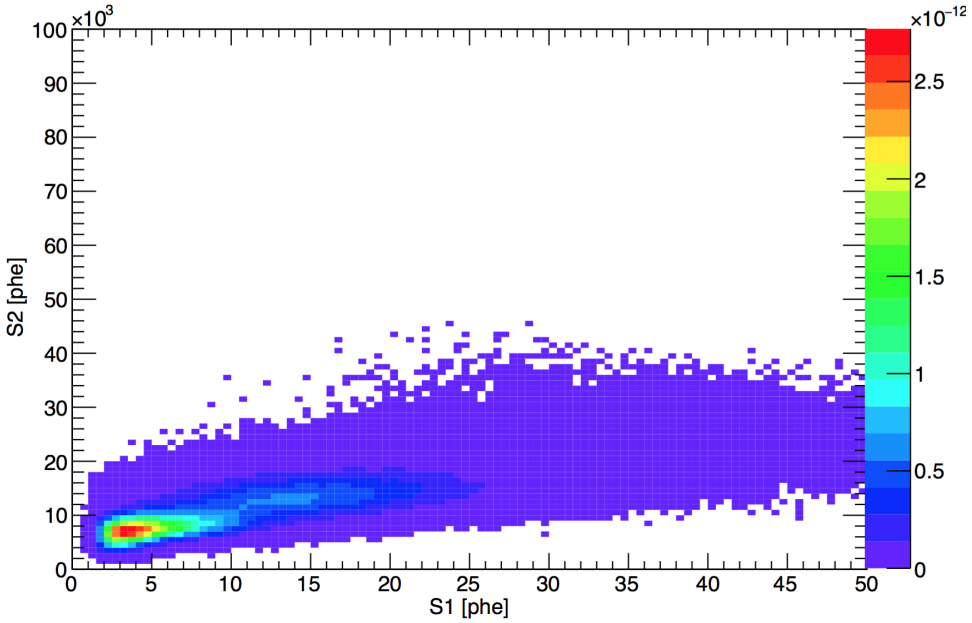

Figure 5.21 *Signal model projected in the two-dimensional space of S2 as a function of S1, for massless solar axions. The distribution peaks at low energies (corresponding to few units of photoelectrons in S1) and smoothly goes down to zero as the energy increases. The range of S2 values covered by the distribution is part of the electron-recoil band, while the scale on the third axis, coming out of the page, is proposed for an arbitrary choice of the coupling constant,* $g_{Ae} = 10^{-13}$.

The LZ statistical framework has been built to use only two observables: $S1$, the number of detected photons from the prompt scintillation, and $S2$, the number of detected photons of the proportional signal. Selection cuts impose $S1$ pulses to have a 3-fold coincidence between PMTs in the target volume. Moreover, $S1$ and $S2$ values are required to be in the range $(0 - 150)$ and $(350 - 10^5)$ photoelectrons, respectively.

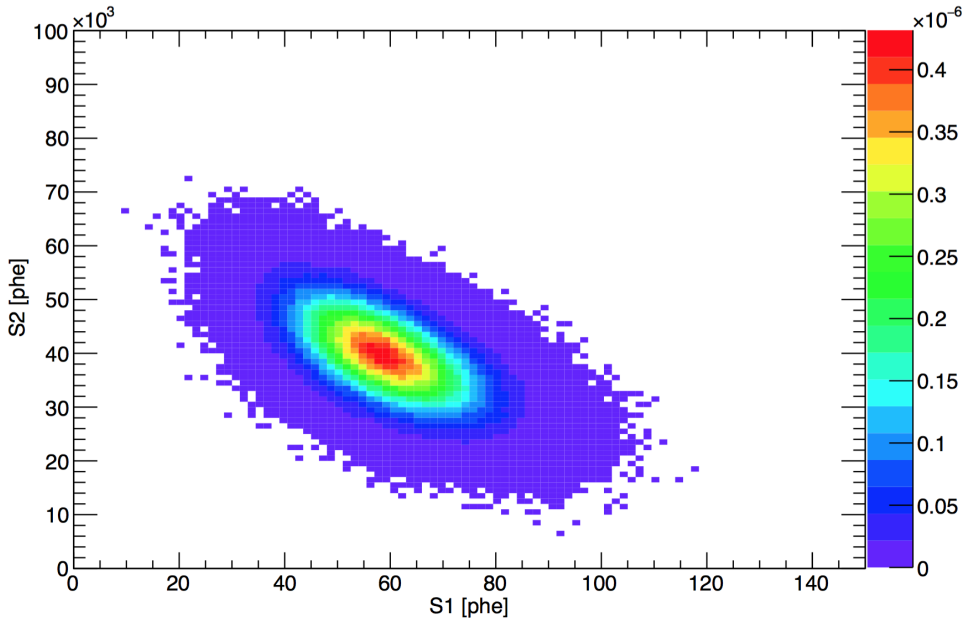

Figure 5.22 *Signal model projected in the two-dimensional space of $S2$ as a function of $S1$, for 20 keV/c^2 mass galactic ALPs. The distribution is a blob centred at the number of photoelectrons corresponding to the ALP mass and laying in the electron-recoil band on $S2$. On the third axis, coming out of the page, the scale of the distribution is proposed for an arbitrary choice of the coupling constant, $g_{Ae} = 10^{-13}$.*

The signal models for massless solar axions and non-relativistic galactic axion-like particles have been built as two-dimensional probability density functions, in the $S2$ versus $S1$ space, by using NEST. The theoretical inputs to the models are the same as described in the previous sections of this chapter. Figure 5.21 shows the axion signal model, generated for an arbitrary value of the coupling, $g_{Ae} = 10^{-13}$. The distribution is peaked at few units of photoelectrons, as required by the expected spectrum, and lays in the electron-recoil band. As for the axion-like particles, the sensitivity study has been done in the $1 - 40$ keV/c^2 mass range, in steps of 1 keV/c^2, testing 40 different signal models. A 20 keV/c^2 ALP example is shown in Fig. 5.22. The distribution has the typical blob shape, representing

the expected peaked energy spectrum, centred at the mass of the candidate.

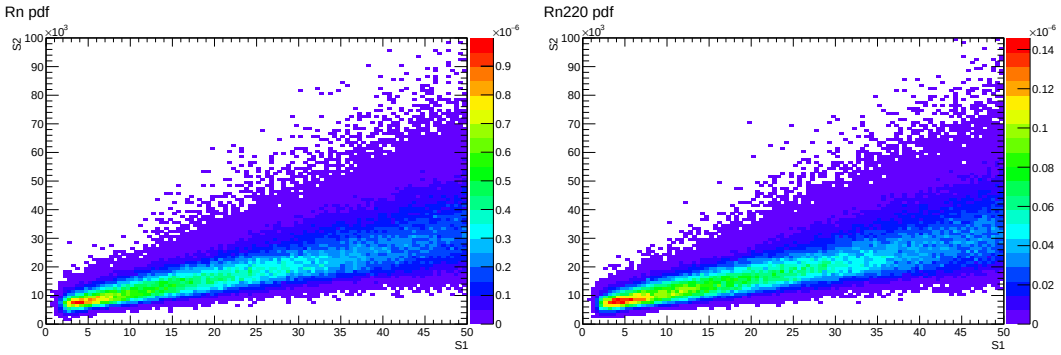

Figure 5.23 *The main contribution to the LZ background model is radon. We expect intrinsic radioactive contamination of the liquid xenon from ^{222}Rn and ^{220}Rn from the ^{232}Th decay chain.*

The LUX–ZEPLIN Technical Design Report [162] gives a deep insight in the dominant backgrounds that are expected in LZ, and the background model has been derived according to the expectations, by using a simulation of the experiment in the LUXSim framework. We expect different sources of background, but not all of them contribute at the same level. The axion and ALP sensitivity studies are mainly affected by the radon background, that is shown in Fig. 5.23, and consists of intrinsic radioactive contamination of the liquid xenon from ^{222}Rn and ^{220}Rn produced in the ^{232}Th decay chain. The expected rates in the fiducial target are 11.2 mBq of ^{222}Rn, and 0.1 μBq/kg of ^{220}Rn. Background rates are treated as nuisance parameters in the analysis. The parameter of interest is the number of signal events, converted to the coupling according to Eq. 5.8.

5.5.3 Axion and axion-like particle sensitivity projections for LZ

Figure 5.24 shows the coupling between solar axions and electrons as a function of the axion mass. Solar axion has been assumed massless and the mass range is limited at 1 keV/c^2 because of the theoretical conditions on the solar flux estimation. The sensitivity reach of LZ is to exclude values of the coupling, g_{Ae}, larger than 1.5×10^{-12} at 90% C.L. For axion-like particles, a scan over masses within the range 1 – 40 keV/c^2 constrains expected values of the coupling to be no larger than 5.9×10^{-14}, across the full range (Fig. 5.25). The sensitivity is driven by the axio-electric cross section on xenon (Fig. 5.2), resulting in a similar

trend to XENON100 and LUX limits.

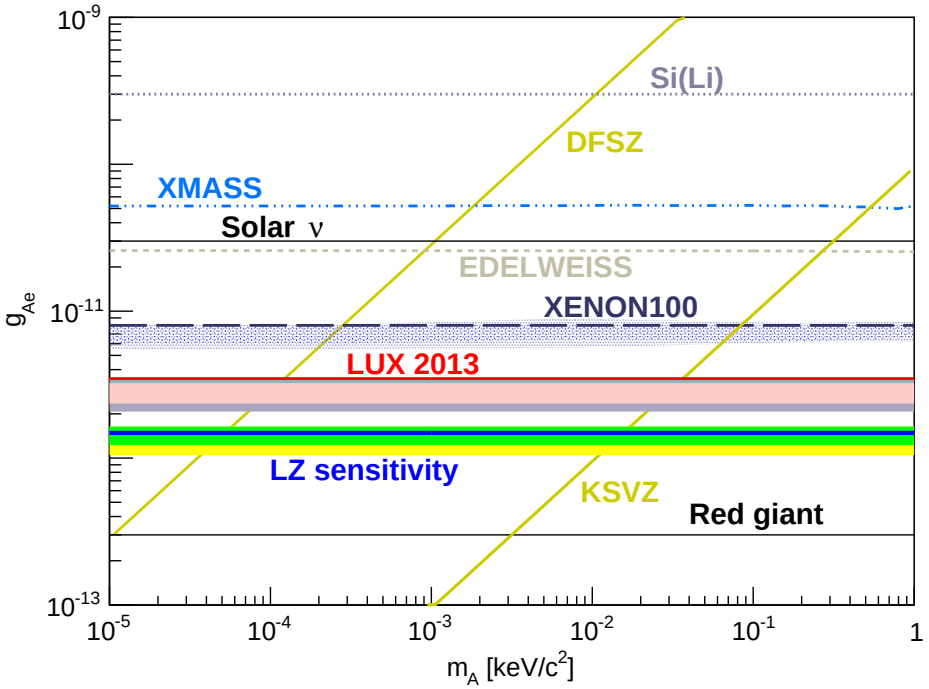

Figure 5.24 *Blue curve: 90% C.L. sensitivity on the coupling between solar axions and electrons, ± 1 σ (green band), and ± 2 σ (yellow band). Results from other experiments are included (as published in 2017 in Ref. [146]), as well as the astrophysical limit set via the Red Giant cooling process, and the theoretical models describing QCD axions.*

Comparing Fig. 5.24 and 5.25, the gain in sensitivity is not the same in the two studies. This is due to the different dependences of the signal rates on the coupling, as previously discussed. Anyway, the improvement gained by LZ is relevant in both cases.

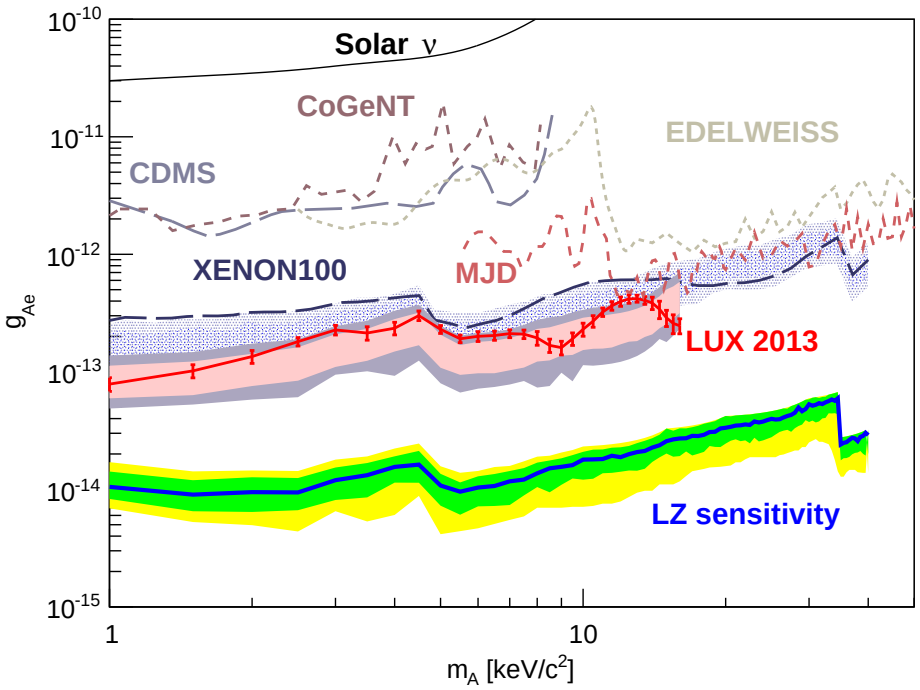

Figure 5.25 *Blue curve: 90% C.L. sensitivity on the coupling between galactic axion-like particles and electrons, ± 1 σ (green band), and ± 2 σ (yellow band). Results from other experiments are also included (as published in 2017 in Ref. [146]).*

5.6 The big picture

Interest in axions and axion-like particles has recently grown in the community, and searches have been included in the scientific programmes of many experiments. This chapter described the approach to axion searches proper of direct dark matter detection experiments, that are able to probe the coupling between axions or axion-like particles and electrons, g_{Ae}. This is not the mainstream in the field though.

5.6.1 Axion-photon coupling

Dedicated axion experiments are usually designed to test the coupling with photons, $g_{A\gamma}$, that has dimension (energy)$^{-1}$. This is the case of the CERN Axion Solar Telescope (CAST), a helioscope using a 9 T LHC dipole magnet directed towards the Sun to convert axions to x rays. The target of such a device

is the axion flux coming from the Sun. CAST took data since 2003. In 2017 the CAST collaboration delivered the most recent exclusion result in the phase space of $g_{A\gamma}$ versus axion mass, shown as the solid blue line in Fig. 5.26. For axion masses smaller than 0.02 eV, CAST excludes values of $g_{A\gamma}$ larger than 0.66 $\times$ 10^{-10} GeV^{-1}, at 95% C.L. [70], reaching similar levels to the most restrictive astrophysical axion bounds (c.f. Chapter 2).

Figure 5.26 also includes other results, such as the one from the previous helioscope, Sumico, and the one from DAMA. Latest limits from the laser propagation experiments OSQAR and PVLAS are also shown, together with exclusion regions set by the high-energy photon propagation in astrophysical B-fields (H.E.S.S.), the SN1987A observation, and the telescope for cosmic axion decay lines. The diagonal yellow band covers the scope of typical QCD axion models, with the KSVZ model highlighted as a green line. The vertical dashed red line represents the limit for cosmic hot dark matter.

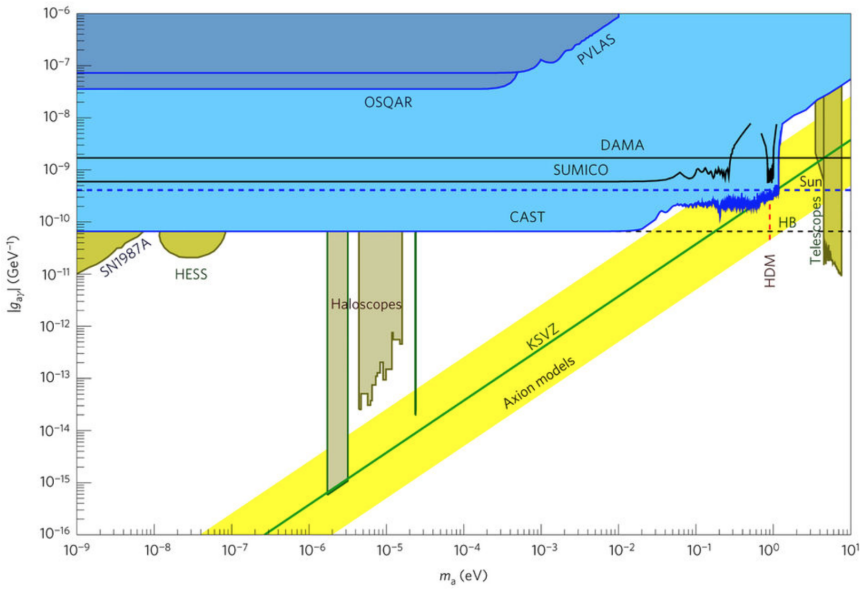

Figure 5.26 *The axion-photon coupling, $g_{A\gamma}$, in GeV^{-1}, as a function of the axion mass in eV. Solid blue line: exclusion from the latest CAST data taking, 2013 – 2015 run. Diagonal yellow band: typical QCD axion models. Diagonal green line: the KSVZ axion model. Results from other experiments are also shown [70].*

The future of searches targeting the axion-photon coupling, $g_{A\gamma}$, will be dominated by the proposed helioscope, called International AXion Observatory (IAXO) [163], and, for small masses, by the upcoming ALPS-II laser propagation experiment at DESY [164].

5.6.2 Complementarity

A discussion on the complementarity of the results obtained from different experimental approaches closes this chapter. It is interesting to understand how a limit on the coupling with electrons can be converted to a limit on the coupling with photons. The answer is not straightforward, and a model-independent conversion is not possible. Limits on either couplings are set as a function of the candidate mass (c.f. Fig. 5.17 and 5.26). Under the assumption of one of the theoretical models describing QCD axions, limits on the coupling can be converted to limits on the mass. A comparison of the results is then possible, although being strongly model-dependent.

An interesting attempt to constrain both couplings at once has been done by the CAST Collaboration, who managed to constrain the product of the two to be $g_{Ae} \times g_{A\gamma} \lesssim 8.1 \times 10^{-23}$ GeV^{-1}, for axion masses smaller than 10 meV [165], by using the first set of data as in 2013. The result of their study, shown in Fig. 5.27, is only valid for the particular choice of mass, and implies a strong correlation level.

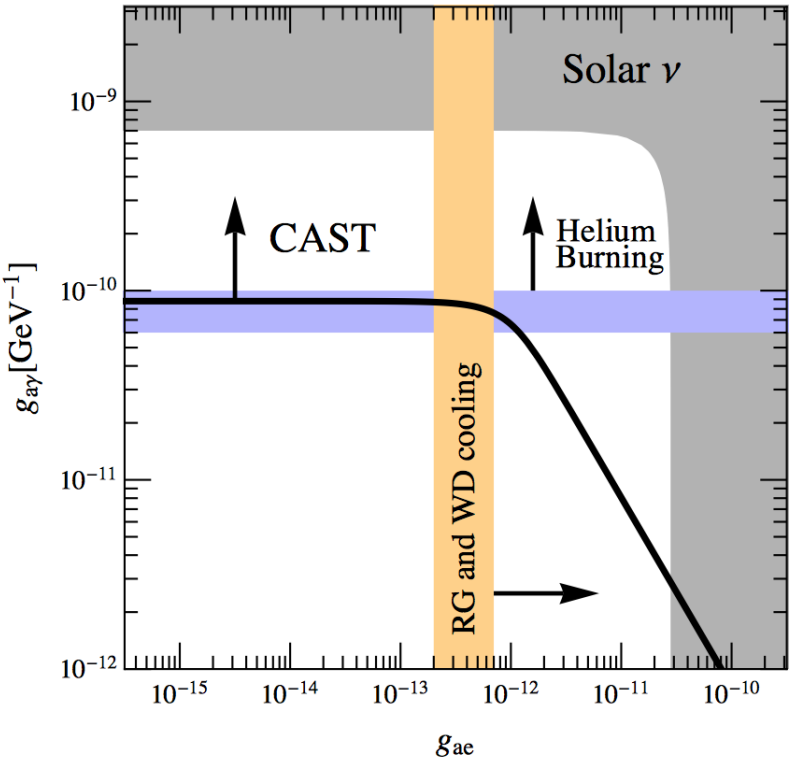

Figure 5.27 *Constrains on g_{Ae} and $g_{A\gamma}$ for axion masses smaller than 10 meV. CAST data exclude the region above the solid black line. The vertical orange band represents values of g_{Ae} affected by red giant evolution and white dwarf cooling, processes which exclude larger values of g_{Ae}. The horizontal blue band identifies values of $g_{A\gamma}$ excluded by helium-burning stars. Finally, the grey region is ruled out by solar neutrino experiments [165].*

This chapter has been dedicated to searches for axions and axion-like particles, with a very detailed insight in the analyses performed on the LUX 2013 data. Predictions on the sensitivity of LZ have been discussed, as well as an overview of the wider landscape of axion searches. Interest in axions and ALPs is growing, and a detection is expected to come with the next generation experiments.

Chapter 6

Two-neutrino double electron capture searches

Dark matter detectors, and dual-phase time projection chambers in particular, can be multi-task devices. Indeed, they can be used to search for a variety of rare phenomena beside dark matter interactions. TPCs offer a quiet fiducial volume to explore signals generated by different sources, and we have already discussed that various candidates for dark matter can be accessible through the LUX detector (c.f. Chapter 4 and 5). In this chapter, we focus on a neutrino-related topic.

Neutrinos are of great interest in particle physics, as there are several questions yet to be answered, such as whether neutrinos are Dirac or Majorana particles. As introduced in Chapter 1, there is more than one channel available to test the nature of neutrinos. Some of these phenomena share the same theoretical framework, and this makes the two-neutrino double electron capture (2νDEC) an interesting topic.

Data collected in 2013, with an exposure totalling 63.8 live days $\times$ 145 kg, have been searched for ^{124}Xe two-neutrino double electron capture signal in the LUX detector. This chapter presents a detailed description of the analysis. The production of the signal model is described. Background expectations are outlined, given that the region of interest of this study is not the same as in the dark matter analyses previously discussed. The analysis technique and the obtained results close the chapter.

6.1 Signal model

6.1.1 ^{124}Xe 2νDEC

Natural xenon consists of eight isotopes, including 0.095% by mass ^{124}Xe. The decay process for 2νDEC of ^{124}Xe is:

$$^{124}Xe + 2e^{-} \rightarrow ^{124}Te + 2\nu_e, \tag{6.1}$$

where the reaction Q-value is 2864 keV. The branching ratio for events in which both electrons are captured from the K-shell is estimated as 76.6% [27], and leads to a cascade of x rays and Auger electrons being emitted from the daughter ^{124}Te atom as the newly created K-shell vacancies are refilled. Consequently, the expected signal consists of the fast emission of two or more x rays and/or Auger electrons with energies totalling 63.6 keV. The nuclear recoil energy in this case is of the order of 30 eV, and is therefore negligible.

Mei *et al.* [27] and Barros *et al.* [166] proposed that such a signal could be detected in large-scale liquid xenon dark matter detectors, as they provide good sensitivity to energy depositions in the range of tens keV. Moreover, these devices have large enough fiducial volumes to provide a sufficient exposure, even if the isotopic abundance of ^{124}Xe is quite low. In this analysis, 138 g of ^{124}Xe have been observed for 63.8 live days.

6.1.2 LUX 2νDEC expected signal

In LUX, x rays and Auger electrons primarily deposit energy through interactions with electrons in the liquid xenon. Thus, a 2νDEC signal would result in additional events within the electron-recoil band. Given that the signal arises from the simultaneous deposition of x rays and/or Auger electrons, the expected experimental signature will be a peak centred at 63.6 keV. To assess whether the width of the peak depends on the multiplicity of the contributing energy depositions, perhaps due to energy dependent changes in the scintillation and ionization yields, simulations have been conducted with the Noble Element Simulation Technique (NEST) package [134, 135, 150]. Energy depositions from a single 63.6 keV γ ray showed no significant difference to those of simultaneous

31.8 keV γ rays (or electrons or x rays), and both peaks were well described by Gaussians. To give an example, Fig. 6.1 shows the simulation of energy deposition of two simultaneous 31.8 keV γ rays on the combined energy scale.

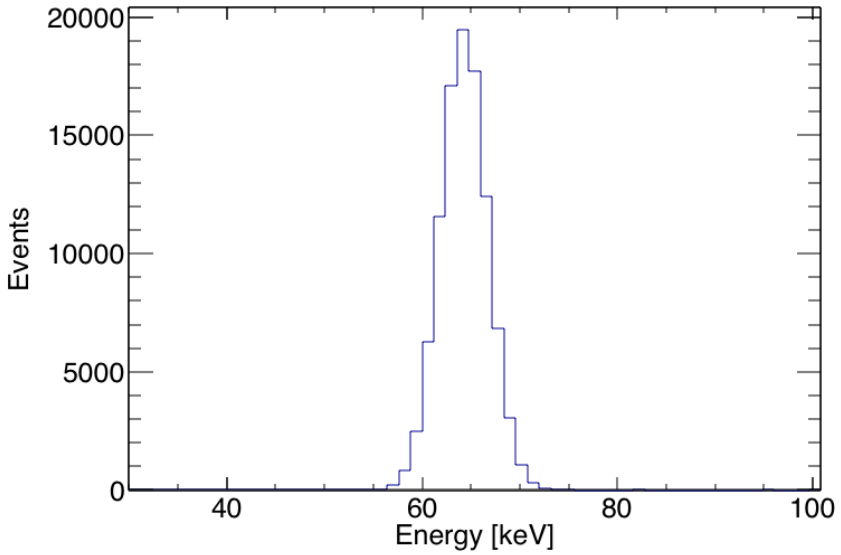

Figure 6.1 *Simulation of energy deposition of simultaneous 31.8 keV γ rays. The simulation represents ^{124}Xe 2νDEC signal as expected in LUX. Events are plotted on combined energy scale (Eq. 5.2) and the resulting peak is well described by a Gaussian.*

Having confirmed that the width of the peak does not depend on the multiplicity of the contributing energy depositions, a calibration-driven approach has been chosen to estimate the predicted experimental energy resolution for the 2νDEC signal. The internal ^{83m}Kr and external ^{137}Cs calibrations of the LUX detector have been discussed in Chapter 3, as well as the cosmogenic activation of ^{127}Xe and ^{131m}Xe. The lines arising from these contributions provide an accurate knowledge of the experimental energy resolution over a broad range of energies, as described in Ref. [125] and shown in Fig. 3.30. By fitting and interpolating the energy dependent width of the peaks, the width expected at 63.6 keV has been estimated to be (2.63 $\pm$ 0.08) keV.

6.2 Energy spectrum

6.2.1 Background expectations

Energy depositions in the LUX 2013 data set are presented in Fig. 6.2. Compton scattering of higher energy γ rays emitted from ^{238}U, ^{232}Th and ^{40}K contaminants of detector components, and from ^{222}Rn in the xenon target, are expected to contribute to a broadly continuous background of events. The data are consistent with the expectations (c.f. Fig. 3.18), in terms of rate and profile. The peak seen around 33 keV is due to the decay of cosmogenically activated ^{127}Xe, as already discussed in Chapter 3 (c.f. Fig. 3.19).

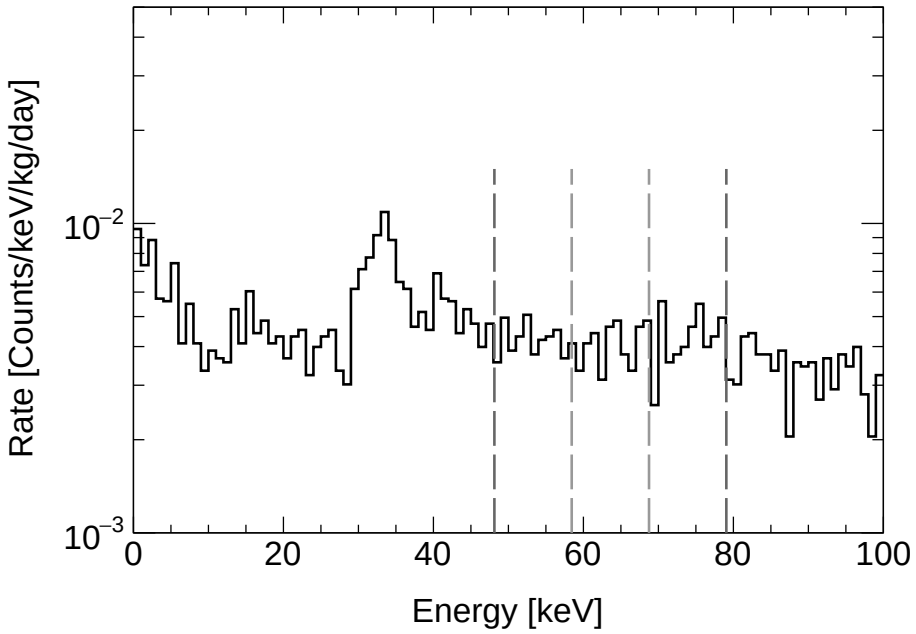

Figure 6.2 *Rate of energy depositions between 0 and 100 keV, as a function of the deposition energy, for the LUX 2013 data set. Only events within the 145 kg fiducial volume have been considered, applying cuts in radius ($r < 20$ cm) and vertical coordinate (8.5 cm $< z <$ 48.6 cm). This is an expanded view of the region where the signal from 2νDEC is anticipated, with the dashed grey lines identifying the region of interest and the side bands.*

6.2.2 Analysis cuts

Figure 6.2 only shows events within the 145 kg fiducial volume selected for the analysis. A radial cut has been applied to remove events with radius larger than 20 cm. Cuts on the vertical coordinate require that 8.5 cm $< z <$ 48.6 cm.

The results described in Chapter 4 and 5 have been obtained from a 95 live days exposure, that includes ^{83m}Kr calibration periods. As presented in Chapter 3, periodic injections of ^{83m}Kr in the detector gas system were used to monitor the detector activity and response. Once injected, ^{83m}Kr nuclei decay by internal transition with a half life of 1.83 hours, emitting sequential 32.2 and 9.4 keV γ rays that may then be detected as a single event. As a consequence of the injections, the event rate is typically raised by 100 Hz, and the resulting signal may contaminate the 2νDEC region of interest. For this reason, the data used in this analysis omit selected periods to reduce possible ^{83m}Kr contamination down to a single event. The resulting exposure is 63.8 live days.

6.3 Analysis technique

6.3.1 The region of interest

The vertical light and dark grey dashed lines in Fig. 6.2 identify, respectively, the region of interest (ROI) and side bands that have been chosen for the 2νDEC analysis. An appropriate width of 10.31 keV for such regions has been estimated, based on the experimental energy resolution for the signal, while the expected energy of the 2νDEC summed peak fixes the centre of the ROI at 63.6 keV.

Assuming that the centroid and the width of a signal peak are reconstructed correctly, the ROI has been set to accept 95% of 2νDEC events. The uncertainty in the acceptance is calculated as having independent contributions from the error on the width of the peak, and from the expected rms deviation from its true energy. The latter has been estimated to be 0.60 keV, because this is the rms deviation from known values of the centroids of the calibration peaks (c.f. fits in Ref. [125]). The resulting ROI acceptance is then $95.0^{+2.1}_{-5.5}$%.

Two factors contribute to the overall efficiency for a 2νDEC signal detection

in the ROI:

$$\epsilon_{tot} = \epsilon_{acc} \times \epsilon_{det} = 95\ \% \times 99.2\ \% = 94.2^{+2.1}_{-5.5}\ \%. \tag{6.2}$$

Here, ϵ_{acc} represents the ROI acceptance, while $\epsilon_{det} = (99.2 \pm 0.1)$ % is the signal detection efficiency. The latter has been evaluated with the LUX simulation package, LUXSim [136].

6.3.2 The statistical approach

The search for a 2νDEC signature within the data shown in Fig. 6.2 follows the frequentist statistical approach of Rolke *et al.* [167]. Such a strategy returns an upper limit on the number of signal events, given the estimate of the background rate in the ROI, the signal detection efficiency, and the number of events observed in the ROI. The upper limit on the number of signal events is broadly expected to be proportional to the square root of the background rate.

It might be argued why the analysis has not been conducted with the fully frequentist Feldman-Cousins method. Rolke's approach has been preferred in this case because it is capable of treating uncertainties by including nuisance parameters in the analysis. The Feldman-Cousins technique can be used when uncertainties on background expectation and signal detection efficiency are negligible, which is not the case of the LUX 2νDEC search.

The number of background events in the ROI is estimated as the average of the absolute number of events in the two side bands (Table 6.1), resulting in (406 ± 14) events. A Gaussian uncertainty is assumed on this estimate of the background rate, as well as on the signal detection efficiency, both treated as nuisance parameters.

Region of the spectrum	Absolute number of events
Region of interest	395 ± 20
Left side band	402 ± 20
Right side band	411 ± 20

Table 6.1 *The absolute number of events in the region of interest and side bands of the energy spectrum shown in Fig. 6.2. The numbers of events correspond to a 145 kg fiducial volume.*

The 90% C.L. upper limit on the number of signal events, μ_{up}, obtained with the Rolke analysis is then used as an input to the half life formula (c.f. Eq. 1.20), as reported by Mei *et al.* [27]:

$$T_{1/2}(0^+ \to g.s.) \geqslant \frac{ln(2)\ f_k\ \epsilon_{tot}\ a\ \frac{MN_A}{A}\ \Delta T}{\mu_{up}}, \tag{6.3}$$

where $f_k = 0.766$ is the fraction of 2K captures accompanied by the emission of two K x rays, ϵ_{tot} is the signal detection efficiency (Eq. 6.2), $a = 0.095\%$ is the isotopic abundance for ^{124}Xe, M is the fiducial mass in kg, N_A is the Avogadro constant, $A = 124$ is the atomic mass number for the selected isotope, and $\Delta T = 63.8$ days is the live time.

6.4 Results

A first iteration of the analysis returns the sensitivity of LUX. The number of events observed in the ROI is fixed at the expectation, so that we extract an expected limit based on the side bands only. Then, considering the real number of events in the ROI, we repeat the analysis to obtain the observed limit.

While a larger fiducial volume provides a greater exposure, the majority of the events clearly arise from radiological backgrounds penetrating from sources external to the liquid xenon itself. As previously discussed in this thesis, they are mainly due to detector components and external backgrounds (c.f. Chapter 3). Consequently, a possible optimisation has been considered, as in exploiting the self shielding property of the xenon target and analyse a more central volume, trading off a reduced fiducial mass for a lower background rate. To explore this, radial and vertical fiducial volume cuts were varied and the expected and observed limit on 2νDEC life time recalculated for each choice. Doing so revealed a weak dependency between the exposure and both the expencted and observed limit, as shown in Fig. 6.3. The ROI consistently has a deficit of events that induces an observed limit better than expectation for most of the fiducial choices.

It is generally considered unreasonable to allow a downward fluctuation to lead to limit being reported that is better than expectation. Thus the result has to be truncated at the expectation. Given the uniform trend of the expected limit as a function of exposure, an optimisation of the fiducial volume is not needed,

and the 145 kg mass seems a reasonable choice as consistent with other LUX analyses. The expected 90% C.L. upper limit on the number of signal events for this choice of exposure is $\mu_{up} = 42.8$ events. Application of Eq. 6.3 returns a lower limit for the half life for two–neutrino double electron capture from the K-shell of ^{124}Xe of 1.4×10^{21} years, at 90% C.L.

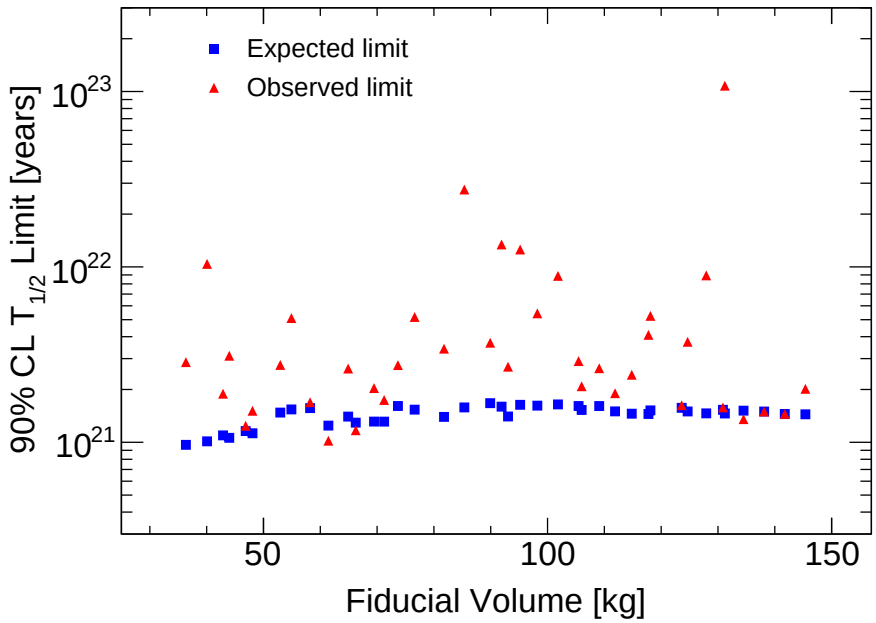

Figure 6.3 *The 90% C.L. lower limit on the 2νDEC lifetime as a function of the fiducial volume. For each fiducial volume, a blue square represents the expected limit, and a red triangle represent the limit observed on data. There is weak dependence on choice of fiducial volume, and the ROI consistently has a deficit of events that induces an observed limit better than expectation.*

Searches for two–neutrino double electron capture from the K-shell of ^{124}Xe have been conducted in the past. While LUX delivers a better result than XENON100, that reported a lower limit of 6.5×10^{20} years (90% C.L.) [112], the currently analysed LUX exposure of 2013 data is not enough to exceed the best result to date, a 2.1×10^{22} years (90% C.L.) limit recently reported by XMASS [168].

At the time of thesis submission, an effect associated with $S2$ pulse identification has been found, with a likely impact on the 2νDEC analysis. Work is continuing to resolve this issue, and the publication currently in preparation will likely report a different result than the one discussed in this work.

Chapter 7

Conclusions

This thesis has presented some of the world's most sensitive searches to date for certain types of axion dark matter, axion-like particles, and two-neutrino double electron capture. These have been conducted on the data taken by the Large Underground Xenon (LUX) experiment. While playing its main role in the hunt for dark matter, LUX also presents suitable characteristics to well perform in a broad range of rare event searches.

Evidence for dark matter and physics beyond the Standard Model of particle physics, coming from astrophysics, cosmology, and particle physics, has been discussed in Chapter 1. An overview of candidates that have been proposed for particle dark matter is outlined in Chapter 2, with main focus on axions and axion-like particles.

A discovery of particle dark matter would provide answers to many questions that are being raised about the nature of the universe, thus the experimental effort delivered in this field is massive and vary. Chapter 3 has presented the different possible approaches to dark matter detection. The LUX detector, a xenon time projection chamber, has been described in its components and operations, to provide the information useful to understand the direct detection search strategy employed in the rest of the thesis.

Chapter 4 has presented LUX direct searches for weakly interacting massive particles, the mainstream candidates for dark matter. Chapter 5 has been dedicated to LUX searches for axion dark matter and axion-like particle, that delivered world-leading results on the axion-electron coupling constant. The

chapter also included sensitivity studies made for the LUX-ZEPLIN experiment, the next generation project that will be able to reach surprising sensitivity thresholds in the dark matter phase space.

As an example of rare event search beyond dark matter, the LUX analysis for two-neutrino double electron capture of ^{124}Xe has been presented in Chapter 6. Although being allowed by the Standard Model, two-neutrino double electron capture shares the matrix element calculation framework with the neutrinoless channel of the same process, becoming of great interest in the scope of neutrino physics.

This work generally aims at describing the critical role played by dark matter and new physics in contemporary science, as well as reporting the multi-task and competitive nature of the Large Underground Xenon experiment.

Appendix A

List of publications

A.1 First Searches for Axions and Axion-like Particles with the LUX Experiment

The paper has been published on Physics Review Letters in 2017, and can be found in Ref. [146].

A.2 First Searches for two-neutrino Double Electron Capture of ^{124}Xe with the LUX Experiment

The paper has almost been completed, but not published yet.

Bibliography

[1] Planck Collaboration. *Astronomy & Astrophysics*, 594(A13), 2016.

[2] M.A. Luty. *Phys. Rev.*, D45:455–465, 1992.

[3] G. Bertone and D. Hooper. *arXiv:1605.04909 [astro-ph.CO]*, 2016.

[4] F. Zwicky. *Astrophysical Journal*, 86(217), 1937.

[5] S. Smith. *Astrophysical Journal*, 83(23), 1936.

[6] H.W. Babcock. *Lick Observatory bulletin*, 498:41–51, 1939.

[7] V.C. Rubin, W.K. Ford Jr., and N. Thonnard. *Astrophysical Journal*, 225:L107–L111, 1978.

[8] V.C. Rubin and W.K. Ford Jr. *Astrophysical Journal*, 159:379, 1970.

[9] D. Clowe, M. Bradac, A.H. Gonzalez, M. Markevitch, S.W. Randall, C. Jones, and D. Zaritsky. *Astrophysical Journal*, 648:L109–L113, 2006.

[10] G.F. Smoot et al. *Advances Space Research*, 11:193–205, 1991.

[11] G. Hinshaw et al. *Astrophysical Journal Supplement*, 208(25), 2013.

[12] D.J. Fixsen. *Astrophysical Journal*, 707:916–920, 2009.

[13] X. Li, J. Hjorth, and R. Wojtak. *Astrophys. J.*, 796(1), 2014.

[14] C. Patrignani et al. (Particle Data Group). *Chin. Phys.*, C40(100001), 2016.

[15] S. Pastor. *Physics of Particles and Nuclei*, 42:628–640, 2011.

[16] X. Qian and P. Vogel. *Prog. Part. Nucl. Phys.*, 83:1–30, 2015.

[17] E.W. Otten and C. Weinheimer. *Rept. Prog. Phys.*, 71(086201), 2008.

[18] D.N. Spergel et al. (WMAP Collaboration). *Astrophysical Journal Supplement*, 148:175–194, 2003.

[19] K.S. Hirata et al. *Phys. Rev.*., D38(448), 1988.

[20] M. Czakon, M. Zralek, and J. Gluza. *Acta Phys. Polon.*, B30:3121–3138, 1999.

[21] B. Kayser. *J. Phys.: Conf. Ser.*, 173(012013), 2009.

[22] F.T. Avignone III, S.R. Elliott, and J. Engel. *Rev. Mod. Phys.*, 80(481), 2008.

[23] J. Bernabeu, A. De Rujula, and C. Jarlskog. *Nucl. Phys.*, B223:15–28, 1983.

[24] Z. Sujkowski and S. Wycech. *Phys. Rev.*, C70(052501), 2004.

[25] J. Suhonen. *J. Phys.: Conf. Ser.*, 375(042026), 2012.

[26] J. Kotila, J. Barea, and F. Iachello. *Phys. Rev.*, C89(064319), 2014.

[27] D.M. Mei et al. *Phys. Rev.*, C89(014608), 2014.

[28] S.M. Bilenky and C. Giunti. *Int. J. Mod. Phys.*, A30(1530001), 2015.

[29] F. Šimkovic. *Prog. Part. Nucl. Phys.*, 66:446–451, 2011.

[30] F. Šimkovic. *Phys. Rev.*, C83(015502), 2011.

[31] M. Hirsch, K. Muto, T. Oda, and H.V. Klapdor-Kleingrothaus. *Z. Phys.*, A347(151), 1994.

[32] J. Suhonen and O. Civitarese. *Phys. Rep.*, 300(123), 1998.

[33] V.V. Kazalov V.V. Kuzminov S.I. Panasenko Y.M. Gavrilyuk, A.M. Gangapshev and S.S. Ratkevich. *Phys. Rev.*, C87:035501, 2013.

[34] O.V. Pravdivtseva A.P. Meshik, C.M. Hohenberg and Y.S. Kapusta. *Phys. Rev.*, C64:035205, 2001.

[35] P. Burnard M. Pujol, B. Marty and P. Philippot. *Geochim. Cosmochim. Acta*, 73:6834, 2009.

[36] R.D. Peccei. *Lect. Notes Phys.*, 741:3–17.

[37] J. Liu, C.Q. Geng, and J.N. Ng. *Phys. Rev. Lett.*, 63(589), 1989.

[38] E.M. Purcell and N.F. Ramsey. *Phys. Rev.*, 78(807), 1950.

[39] J.M. Pendlebury et al. *Phys. Rev.*, D92(092003), 2015.

[40] J.R. Primack. *arXiv:astro-ph/9707285*, 1997.

[41] C.J. Copi, D.N. Schramm, and M.S. Turner. *Science*, 267:192–199, 1995.

[42] C. Alcock et al. *Astrophysical Journal*, 542:281–307, 2000.

[43] C. Afonso et al. *Astronomy & Astrophysics*, 400:951–956, 2003.

[44] C.G. Tinney. *Nature*, 397:37–40, 1999.

[45] N. Bellomo, J.L. Bernal, A. Raccanelli, and L. Verde. *JCAP*, 1801(004), 2018.

[46] G. Jungman, M. Kamionkowski, and K. Griest. *Physics Reports*, 267:195–373, 1996.

[47] J. Ellis, J.S. Hagelin, D.V. Nanopoulos, K. Olive, and M. Srednicki. *Nuclear Physics*, B238:453–476, 1984.

[48] V.S. Berezinsky. *Phys. Lett.*, B261:71–75, 1991.

[49] D.J.H. Chung, E.W. Kolb, and A. Riotto. *Phys. Rev.*, D59(023501), 1998.

[50] R. Dashen. *Phys. Rev.*, 183(1245), 1969.

[51] G.G. Raffelt. *J. Phys.*, A40:6607–6620.

[52] S. Weinberg. *Phys. Rev. Lett.*, 40(223), 1978.

[53] F. Wilczek. *Phys. Rev. Lett.*, 40(279), 1978.

[54] T.W. Donnelly, S.J. Freedman, R.S. Lytel, R.D. Peccei, and M. Schwartz. *Phys. Rev.*, D18(1607), 1978.

[55] M. Dine, W. Fischler, and M. Srednicki. *Phys. Lett.*, B104:199–202, 1981.

[56] A. Zhitnitsky. *Sov. J. Nucl. Phys.*, 31(260), 1980.

[57] J.E. Kim. *Phys. Rev. Lett.*, 43(103), 1979.

[58] M.A. Shifman, A.I. Vainshtein, and V.I. Zakharov. *Nucl. Phys.*, B166:493–506, 1980.

[59] G.G. Raffelt. *Lect. Notes Phys.*, 741:51–71.

[60] J. Redondo. *JCAP*, 12(008), 2013.

[61] E. Fischbach and D.E. Krause. *Phys. Rev. Lett.*, 83(18), 1999.

[62] E. Witten. *Comm. Math. Phys.*, 92:455–472, 1984.

[63] J.P. Conlon. *J. High Energy Phys.*, 05(078), 2006.

[64] A. Arvanitaki, S. Dimopoulos, S. Dubovsky, N. Kaloper, and J. March-Russell. *Phys. Rev.*, D81(123530), 2010.

[65] M. Cicoli, M.D. Goodsell, and A. Ringwald. *J. High Energy Phys.*, 1210(146), 2012.

[66] P. Arias, D. Cadamuro, Mark Goodsell, J. Jaeckel, J. Redondo, and A. Ringwald. *JCAP*, 06(013), 2012.

[67] P. Sikivie. *Lect. Notes Phys.*, 741:19–50, 2008.

[68] H. Primakoff. *Phys. Rev.*, 81(899), 1951.

[69] P. Gondolo and G.G. Raffelt. *Phys. Rev.*, D79(107301), 2009.

[70] CAST Collaboration. *Nature Physics*, 13:584–590, 2017.

[71] J. Isern, E. García-Berro, L.G. Althaus, and A.H. Córsico. *Astron. Astrophys.*, A86(512), 2010.

[72] G. Raffelt and A. Weiss. *Phys. Rev.*, D51(4), 1995.

[73] T.E.O. Ericson and J.-F. Mathiot. *Phys. Lett.*, B219:507–514, 1989.

[74] A. Sedrakian. *Phys. Rev.*, D93(065044), 2016.

[75] M. Giannotti, I. Irastorza, J. Redondo, and A. Ringwald. *JCAP*, 1605(057), 2016.

[76] E. Di Valentino, E. Giusarma, M. Lattanzi, O. Mena, A. Melchiorri, and J. Silk. *Phys. Lett.*., B752:182–185, 2016.

[77] M. Betz, F. Caspers, M. Gasior, and M. Thumm. *arXiv:1204.4370 [physics.ins-det]*, 2012.

[78] C. Abel et al. *Phys. Rev.*, X7(041034), 2017.

[79] ATLAS Collaboration. *Eur. Phys. J.*, C77(393), 2017.

[80] CMS Collaboration. *JHEP*, 07(014), 2017.

[81] E. Charles et al. *Phys. Rep.*, 636(1), 2016.

[82] MAGIC Collaboration. *JCAP*, 1402(008), 2014.

[83] MAGIC Collaboration Fermi-LAT. *JCAP*, 1602(039), 2016.

[84] G. Dobler, I. Cholis, and N. Weiner. *Astrophys. J.*, 741(25), 2011.

[85] PAMELA Collaboration. *Nature*, 458(607), 2009.

[86] AMS Collaboration. *Phys. Rev. Lett.*, 110(141102), 2013.

[87] S. Adrian-Martinez et al. *Phys. Lett.*, B759:69–74, 2016.

[88] IceCube Collaboration. *European Physical Journal*, C77(146), 2017.

[89] E. Bulbul et al. *Astrophys. J.*, 789(13), 2014.

[90] D. Iakubovskyi A. Boyarsky, O. Ruchayskiy and J. Franse. *Phys. Rev. Lett.*, 113(251301), 2014.

[91] Hitomi Collaboration. *Astrophys. J.*, 837(15), 2017.

[92] K. S. Jeong T. Higaki and F. Takahashi. *Phys. Lett.*, B733(25), 2014.

[93] C.E. Aalseth et al. (CoGeNT Collaboration). *Phys. Rev. Lett.*, 106(131301), 2011.

[94] J.B.R. Battat et al. *Physics of the Dark Universe*, 9-10:1–7, 2015.

[95] R. Bernabei et al. *Eur. Phys. J.*, C56(333), 2008.

[96] R. Bernabei et al. *Eur. Phys. J.*, C67(39), 2010.

[97] XMASS Collaboration. *Phys. Lett.*, B759:272–276, 2016.

[98] DEAP-3600 Collaboration. *arXiv:1707.08042 [astro-ph.CO]*, 2017.

[99] F. Orio on behalf of the CUORE Collaboration. *Journal of Physics: Conference Series*, 337(012067), 2012.

[100] R. Agnese et al. (SuperCDMS Collaboration). *Phys. Rev.*, D92(072003), 2015.

[101] R. Agnese et al. (SuperCDMS Collaboration). *Phys. Rev.*, D95(082002), 2017.

[102] G. Angloher et al. *Eur. Phys. J.*, C76(1), 2016.

[103] C. Amole et al. (PICO Collaboration). *Phys. Rev. Lett.*, 118(251301), 2017.

[104] A.I. Bolozdynya. *Physics Procedia*, 74:405–410, 2015.

[105] D.S. Akerib et al. (LUX Collaboration). *Nucl. Instrum. Methods*, A704(111), 2013.

[106] P. Agnes et al. *Phys. Lett.*, B743:456–466, 2015.

[107] A. Minamino et al. *Astropart. Phys.*, 35:609–614, 2012.

[108] ZEPLIN-II Collaboration. *Astroparticle Physics*, 28:287–302, 2007.

[109] E. Aprile et al. (XENON Collaboration). *Astropart. Phys.*, 35:573–590, 2012.

[110] E. Aprile et al. (XENON Collaboration). *Phys. Rev. Lett.*, 109(181301), 2012.

[111] E. Aprile et al. (XENON100 Collaboration). *Phys. Rev.*, D95(029904), 2017.

[112] E. Aprile et al. (XENON Collaboration). *Phys. Rev.*, C95:024605, 2017.

[113] E. Aprile et al. (XENON Collaboration). *JCAP*, 1604:027, 2016.

[114] E. Aprile et al. (XENON Collaboration). *arXiv:1705.06655 [astro-ph.CO]*.

[115] PandaX-II Collaboration. *Phys. Rev. Lett.*, 117(121303), 2016.

[116] PandaX-II Collaboration. *Phys. Rev. Lett.*, 118(071301), 2017.

[117] A. Hitachi. *Astro. Phys.*, 24:247–256, 2005.

[118] T. Doke, A. Hitachi, J. Kikuchi, K. Masuda, H. Okada, and E. Shibamura. *Jpn. J. Appl. Phys.*, 41:1538–1545, 2002.

[119] S. Kubota, M. Hishida, and J. Raun. *J. Phys.*, C11(2645), 1978.

[120] A. Barbet et al. *J. Phys. B: At. Mol. Phys.*, 8:1785, 1975.

[121] P. Sorensen. *JCAP*, 09(033), 2010.

[122] E. Aprile et al. *Phys. Rev. Lett.*, 97(081302), 2006.

[123] J. Lindhard and M. Scharff. *Phys. Rev.*, 124(128), 1961.

[124] A. Manzur, A. Curioni, L. Kastens, D. N. McKinsey, K. Ni, and T. Wongjirad. *Phys. Rev.*, C81(025808), 2010.

[125] D.S. Akerib et al. (LUX Collaboration). *Phys. Rev.*, D95(012008), 2017.

[126] J. Thomas and D.A. Imel. *Phys. Rev.*, A36(2), 1987.

[127] D.S. Akerib et al. (LUX Collaboration). *arXiv:1608.05381v2 [physics.ins-det]*, 2016.

[128] D.S. Akerib et al. (LUX Collaboration). *Nucl. Instr. Meth.*, A668(1), 2012.

[129] D. Mei and A. Hime. *Phys. Rev.*, D73(053004), 2006.

[130] D.S. Akerib et al. (LUX Collaboration). *Astropart. Phys.*, 62:33–46, 2015.

[131] D.S. Akerib et al. (LUX Collaboration). *Phys. Rev. Lett.*, 116(161301), 2016.

[132] L.W. Kastens, S.B. Cahn, A. Manzur, and D.N. McKinsey. *Phys. Rev.*, C80(045809), 2009.

[133] D.S. Akerib et al. (LUX Collaboration). *Phys. Rev.*, D93(072009), 2016.

[134] M. Szydagis et al. *JINST*, 6(P10002), 2011.

[135] M. Szydagis et al. *JINST*, 8(C10003), 2013.

[136] D.S. Akerib et al. (LUX Collaboration). *Nucl. Instrum. Methods*, A675(63), 2012.

[137] J.D. Lewin and P.F. Smith. *Astroparticle Physics*, 6:87–112, 1996.

[138] Til Piffl et al. *Astronomy & Astrophysics*, 562(A91), 2014.

[139] D.S. Akerib et al. (LUX Collaboration). *Phys. Rev. Lett.*, 112(091303), 2014.

[140] Chung-Lin Shan. *JCAP*, 07(005), 2011.

[141] R.H. Helm. *Phys. Rev.*, 104(1466), 1956.

[142] G. Cowan, K. Cranmer, E. Gross, and O. Vitells. *Eur. Phys. J.*, C71(1554), 2011.

[143] D.S. Akerib et al. (LUX Collaboration). *Phys. Rev. Lett.*, 118(021303), 2017.

[144] D.S. Akerib et al. (LUX Collaboration). *Phys. Rev. Lett.*, 116(161302), 2016.

[145] D.S. Akerib et al. (LUX Collaboration). *Phys. Rev. Lett.*, 118(251302), 2017.

[146] D.S. Akerib et al. (LUX Collaboration). *Phys. Rev. Lett.*, 118(261303), 2017.

[147] G.D. Starkman S. Dimopoulos and B.W. Lynn. *Phys. Lett.*, B168(145), 1986.

[148] M. Pospelov, A. Ritz, and M. Voloshin. *Phys. Rev.*, D78(115012), 2008.

[149] A. Derevianko, V.A. Dzuba, V.V. Flambaum, and M. Pospelov. *Phys. Rev.*, D82(065006), 2010.

[150] B. Lenardo et al. *IEEE Trans. Nucl. Sci.*, 62:3387–3396, 2015.

[151] A. Kolmogorov. *G. Ist. Ital. Attuari*, 4:83–91, 1933.

[152] N. Smirnov. *Annals of Mathematical Statistics*, 19:279–281, 1948.

[153] L. Moneta. *https://root.cern.ch/doc/v608/StandardHypoTestInvDemo_8C_source.html*.

[154] E. Armengaud et al. *JCAP*, 1311(067), 2013.

[155] K. Abe et al. *Phys. Lett.*, B724:46–50, 2013.

[156] N. Viaux et al. *Phys. Rev. Lett.*, 111(231301), 2013.

[157] E. Gross and O. Vitells. *Eur. Phys. J.*, C70:525–530, 2010.

[158] CMS Collaboration. *Phys. Lett.*, B716:30–61, 2012.

[159] N. Abgrall et al. (MAJORANA Collaboration). *Phys. Rev. Lett.*, 118(161801), 2017.

[160] CDMS Collaboration. *Phys. Rev. Lett.*, 103(141802), 2009.

[161] C.E. Aalseth et al. (CoGeNT Collaboration). *Phys. Rev. Lett.*, 101(251301), 2008.

[162] LZ Collaboration. *arXiv:1703.09144 [physics.ins-det]*, 2017.

[163] E. Armengaud et al. *JINST*, 9(T05002), 2014.

[164] R. Bähre et al. *JINST*, 8(T09001), 2013.

[165] CAST Collaboration. *JCAP*, 05(010), 2013.

[166] K. Zuber N. Barros, J. Thurn. *J. Phys.*, G41(115105), 2014.

[167] W.A.Rolke et al. *Nucl. Instrum. Methods*, A551:493–503, 2005.

[168] K. Abe et al. (XMASS Collaboration). *arXiv:1801.03251*.